STATE OF THE CLIMATE IN 2019

THE TROPICS

H. J. Diamond and C. J. Schreck, Eds.

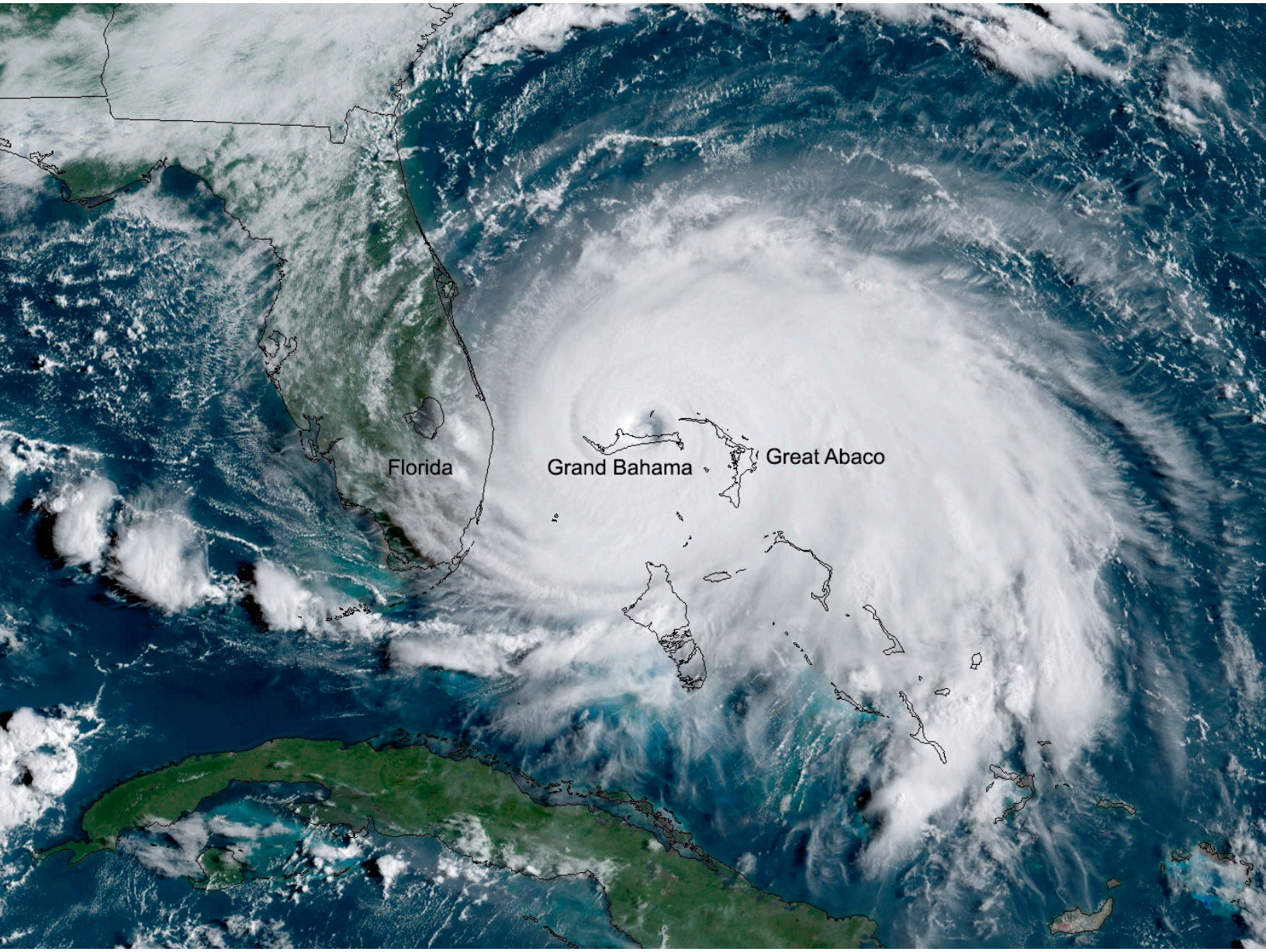

Special Online Supplement to the *Bulletin of the American Meteorological Society,* Vol.101, No. 8, August, 2020

https://doi.org/10.1175/BAMS-D-20-0077.1
Corresponding author: Howard J. Diamond / howard.diamond@noaa.gov
©2020 American Meteorological Society
For information regarding reuse of this content and general copyright information, consult the AMS Copyright Policy.

Unauthenticated | Downloaded 12/18/20 02:53 PM UTC

STATE OF THE CLIMATE IN 2019
The Tropics

Editors

Jessica Blunden
Derek S. Arndt

Chapter Editors

Peter Bissolli
Howard J. Diamond
Matthew L. Druckenmiller
Robert J. H. Dunn
Catherine Ganter
Nadine Gobron
Rick Lumpkin
Jacqueline A. Richter-Menge
Tim Li
Ademe Mekonnen
Ahira Sánchez-Lugo
Ted A. Scambos
Carl J. Schreck III
Sharon Stammerjohn
Diane M. Stanitski
Kate M. Willett

Technical Editor

Andrea Andersen

BAMS Special Editor for Climate

Richard Rosen

American Meteorological Society

Unauthenticated | Downloaded 12/18/20 02:55 PM UTC

Cover credit:
Catastrophic Hurricane Dorian slowed to a crawl over Grand Bahama Island overnight and into Labor Day. On Monday, September 2, 2019, GOES East captured a view of the Category 5 storm over Grand Bahama.

This GeoColor-enhanced imagery was created by NOAA's partners at the Cooperative Institute for Research in the Atmosphere. The GOES East geostationary satellite, also known as GOES-16, provides coverage of the Western Hemisphere, including the United States, the Atlantic Ocean and the eastern Pacific. The satellite's high-resolution imagery provides optimal viewing of severe weather events, including thunderstorms, tropical storms, and hurricanes.
© NOAA

The Tropics is one chapter from the *State of the Climate in 2019* annual report and is available from https://doi.org/10.1175/BAMS-D-20-0077.1. Compiled by NOAA's National Centers for Environmental Information, *State of the Climate in 2019* is based on contributions from scientists from around the world. It provides a detailed update on global climate indicators, notable weather events, and other data collected by environmental monitoring stations and instruments located on land, water, ice, and in space. The full report is available from https://doi.org/10.1175/2020BAMSStateoftheClimate.1.

How to cite this document:

Citing the complete report:
Blunden, J. and D. S. Arndt, Eds., 2020: State of the Climate in 2019. *Bull. Amer. Meteor. Soc.,* **101** (8), Si–S429, https://doi.org/10.1175/2020BAMSStateoftheClimate.1.

Citing this chapter:
Diamond, H.J. and C. J. Schreck, Eds., 2020: The Tropics [in "State of the Climate in 2019"]. *Bull. Amer. Meteor. Soc.,* **101** (8), S185–S238, https://doi.org/10.1175/BAMS-D-20-0077.1.

Citing a section (example):
Chen, L., J. -J Luo, and A. D. Magee, 2020: Indian Ocean dipole [in "State of the Climate in 2019"]. *Bull. Amer. Meteor. Soc.,* **101** (8), S229–S232, https://doi.org/10.1175/BAMS-D-20-0077.1.

Unauthenticated | Downloaded 12/18/20 02:55 PM UTC

Editor and Author Affiliations (alphabetical by name)

Baxter, Stephen, NOAA/NWS Climate Prediction Center, College Park, Maryland
Bell, Gerald D., NOAA/NWS Climate Prediction Center, College Park, Maryland
Blake, Eric S., NOAA/NWS National Hurricane Center, Miami, Florida
Bringas, Francis G., NOAA/OAR Atlantic Oceanographic and Meteorological Laboratory, Miami, Florida
Camargo, Suzana J., Lamont-Doherty Earth Observatory, Columbia University, Palisades, New York
Chen, Lin, Institute for Climate and Application Research (ICAR)/KLME/ILCEC/CIC-FEMD, Nanjing University of Information Science and Technology, Nanjing, China
Coelho, Caio A. S., CPTEC/INPE Center for Weather Forecasts and Climate Studies, Cachoeira Paulista, Brazil
Diamond, Howard J., NOAA/OAR Air Resources Laboratory, College Park, Maryland
Domingues, Ricardo, Cooperative Institute for Marine and Atmospheric Studies, University of Miami, Miami, Florida
Goldenberg, Stanley B., NOAA/OAR/AOML Hurricane Research Division, Miami, Florida
Goni, Gustavo, NOAA/OAR/AOML Hurricane Research Division, Miami, Florida
Fauchereau, Nicolas, National Institute of Water and Atmospheric Research, Ltd., Auckland, New Zealand
Halpert, Michael S., NOAA/NWS Climate Prediction Center, College Park, Maryland
He, Qiong, Earth System Modeling Center, Nanjing University of Information Science and Technology, Nanjing, China
Klotzbach, Philip J., Department of Atmospheric Science, Colorado State University, Fort Collins, Colorado
Knaff, John A., NOAA/NESDIS Center for Satellite Applications and Research, Fort Collins, Colorado
L'Heureux, Michelle, NOAA/NWS Climate Prediction Center, College Park, Maryland
Landsea, Chris W., NOAA/NWS National Hurricane Center, Miami, Florida
Lin, I.-I., National Taiwan University, Taipei, Taiwan
Lorrey, Andrew M., National Institute of Water and Atmospheric Research, Ltd., Auckland, New Zealand
Luo, Jing-Jia, Institute for Climate and Application Research (ICAR)/KLME/ILCEC/CIC-FEMD, Nanjing University of Information Science and Technology, Nanjing, China
Magee, Andrew D., Centre for Water, Climate and Land, School of Environmental and Life Sciences, University of Newcastle, Callaghan, NSW, Austrailia
Pasch, Richard J., NOAA/NWS National Hurricane Center, Miami, Florida
Pearce, Petra R., National Institute of Water and Atmospheric Research, Ltd., Auckland, New Zealand
Pezza, Alexandre B., Greater Wellington Regional Council, Wellington, New Zealand
Rosencrans, Matthew, NOAA/NWS Climate Prediction Center, College Park, Maryland
Schreck III, Carl J., North Carolina State University, Cooperative Institute for Climate and Satellites – North Carolina (CICS-NC), Asheville, North Carolina
Trewin, Blair C., Australian Bureau of Meteorology, Melbourne, Victoria, Australia
Truchelut, Ryan E., "WeatherTiger," Tallahassee, Florida
Wang, Bin, Department of Atmospheric Science and IPRC, University of Hawaii, Honolulu, Hawaii
Wang, H., NOAA/NWS Climate Prediction Center, College Park, Maryland
Wood, Kimberly M., Department of Geosciences, Mississippi State University, Starkville, Mississippi
Woolley, John-Mark, National Institute of Water and Atmospheric Research, Ltd., Auckland, New Zealand

Editoral and Production Team

Andersen, Andrea, Technical Editor, Innovative Consulting and Management Services, LLC, NOAA/NESDIS National Centers for Environmental Information, Asheville, North Carolina
Griffin, Jessicca, Graphics Support, Cooperative Institute for Satellite Earth System Studies, North Carolina State University, Asheville, North Carolina
Hammer, Gregory, Content Team Lead, Communications and Outreach, NOAA/NESDIS National Centers for Environmental Information, Asheville, North Carolina
Love-Brotak, S. Elizabeth, Lead Graphics Production, NOAA/NESDIS National Centers for Environmental Information, Asheville, North Carolina
Misch, Deborah J., Graphics Support, Innovative Consulting and Management Services, LLC, NOAA/NESDIS National Centers for Environmental Information, Asheville, North Carolina
Riddle, Deborah B., Graphics Support, NOAA/NESDIS National Centers for Environmental Information, Asheville, North Carolina
Veasey, Sara W., Visual Communications Team Lead, Communications and Outreach, NOAA/NESDIS National Centers for Environmental Information, Asheville, North Carolina

Unauthenticated | Downloaded 12/18/20 02:55 PM UTC

4. Table of Contents

List of authors and affiliations S188
a. Overview S190
b. ENSO and the tropical Pacific S191
1. Oceanic conditions S192
2. Atmospheric circulation, temperature, and precipitation anomalies during December–February 2018/19 ..... S193
3. Atmospheric circulation, temperature, and precipitation anomalies during March–May through September–November 2019 ..... S194
c. Tropical intraseasonal activity S195
d. Intertropical convergence zones S198
1. Pacific S198
2. Atlantic S199
e. Global monsoon summary S200
f. Tropical cyclones S203
1. Overview S203
2. Atlantic basin S204
Sidebar 4.1: Hurricane Dorian: A devastating hurricane for the northwest Bahamas S210
3. Eastern North Pacific and Central North Pacific basins S212
4. Western North Pacific basin S214
5. North Indian Ocean basin S219
6. South Indian Ocean basin S221
7. Australian basin S223
8. Southwest Pacific basin S225
g. Tropical cyclone heat potential S227
h. Indian Ocean dipole S229
Appendix: Acronym List S233
References S235

***Please refer to Chapter 8 (Relevant datasets and sources) for a list of all climate variables and datasets used in this chapter for analyses, along with their websites for more information and access to the data.**

Unauthenticated | Downloaded 12/18/20 02:55 PM UTC

4. THE TROPICS

H. J. Diamond and C. J. Schreck, Eds.

a. Overview—H. J. Diamond and C. J. Schreck

The tropics in 2019 featured a weak El Niño event that began in January and ended in July. Neutral ENSO conditions prevailed for the remainder of the year, although sea surface temperatures (SSTs) remained above normal in the central Pacific. The Oceanic Niño Index (ONI) met the +0.5°C threshold for El Niño during September–December 2018 and November–December 2019. However, the ocean–atmosphere coupling, normally an intrinsic aspect of El Niño, was missing during both periods.

For the global tropics, combined land and ocean surface temperatures (measured 20°N–20°S) registered +0.47°C above the 1981–2010 average. This makes 2019 the third-warmest year for the tropics since records began in 1880, and the warmest since 2016. Data from the Global Precipitation Climatology Project indicate a mean annual total precipitation value of 1317 mm across the 20°N–20°S latitude band over land. This is 11 mm above the 1981–2010 average and ranks in the middle tercile of the 1979–2019 period of record.

Globally, 96 named tropical cyclones (TCs; ≥34 kt; or 17 m s^{-1}) were observed during the 2019 Northern Hemisphere (NH) season (January–December 2019) and the 2018/19 Southern Hemisphere (SH) season (July–June 2018/19; Table 4.2), as documented in IBTrACSv4 (Knapp et al. 2010). Overall, this number was well above the 1981–2010 global average of 82 TCs and similar to the 95 TCs reported during 2018 (Diamond and Schreck 2019).

In terms of Accumulated Cyclone Energy (ACE; Bell et al. 2000), each NH basin was above its 1981–2010 average. The North and South Indian Ocean basins were in the top 10% of ACE recorded for those basins at 85×10^4 kt^2 and 154×10^4 kt^2, respectively; and in fact, the ACE value in the North Indian Ocean was the highest on record. In the western North Pacific, seven storms (six of Category 5 intensity) out of a total of 28 accounted for 71% of the above-average seasonal ACE of 341×10^4 kt^2. The North Atlantic basin had an ACE of nearly 145% of its 1981–2010 median value but was well below the 241% of median recorded in 2017 (Bell et al. 2018). Category 5 Hurricanes Dorian and Lorenzo alone accounted for >60% of the 2019 total. The Australian and southwest Pacific basins were fairly quiet; each had an ACE that was below normal but still within the middle tercile. The global total was near normal for 1981–2010 with 795×10^4 kt^2. Five TCs across the globe reached Saffir–Simpson Hurricane Wind Scale (SSHWS) Category 5 intensity level—two in the North Atlantic and three in the western North Pacific.

From a socio-economic standpoint, the five Category 5 storms were significant in their effects. Hurricane Dorian caused unprecedented and tremendous devastation, with over 70 fatalities and damages totaling $3.4 billion (U.S. dollars). Hurricane Lorenzo as a post-tropical/extratropical cyclone was the second-deadliest storm of the 2019 North Atlantic season, causing 19 deaths. However, major impacts are not relegated to Category 5 storms, and Super Typhoon Faxai demonstrated that with total damages estimated at $9.3 billion (U.S. dollars). Faxai was one of the strongest typhoons on record to affect Tokyo, Japan, killing three people and injuring 147, causing extensive blackouts, and damaging more than 40 000 homes

The Indian Ocean dipole (IOD), an inherent air–sea coupling mode in the tropical Indian Ocean, exhibited its greatest magnitude recorded since 1997, which was under extremely strong El Niño conditions. The unique feature of the 2019 IOD event was that it occurred during neutral ENSO conditions.

Unauthenticated | Downloaded 12/18/20 02:55 PM UTC

In addition, tropical intraseasonal variability was especially prominent, with three distinct periods of Madden-Julian Oscillation (MJO) activity spanning a total of approximately eight months.

The editors of this chapter would like to insert a personal note recognizing the passing of a past author of the Tropics Chapter. Our colleague and good friend A. Brett Mullan died of cancer on 22 April 2020. Brett was a mainstay of this chapter having stewarded the section on the Pacific Intertropical Convergence Zone from 2006 to 2018. Brett worked for New Zealand's National Institute of Water and Atmosphere and made significant contributions and authored seminal papers in meteorology. These included the analysis of SH climate and circulation variability over interannual (El Niño–Southern Oscillation [ENSO]) to interdecadal (interdecadal Pacific Oscillation) timescales. His work in documenting the relationships of climate variability to long-term global teleconnections has been a basis for seasonal climate prediction for New Zealand commencing in the 1990s. He carried out research into climate change and modeling, with particular emphasis on SH and New Zealand regional effects (Southern Oscillation, greenhouse warming, ocean–atmosphere coupled models and decadal variability, and integrated climate impact models). Over his 40-year career, Brett's contributions to meteorology and climate science and beyond were tremendous. His outstanding work and significant scientific contributions will be his legacy, and he will be greatly missed.

b. ENSO and the tropical Pacific—M. L'Heureux, G. D. Bell, and M. S. Halpert

The El Niño–Southern Oscillation (ENSO) is a coupled ocean–atmosphere climate phenomenon over the tropical Pacific Ocean, with opposite phases called El Niño and La Niña. For historical purposes, NOAA's Climate Prediction Center (CPC) classifies and assesses the strength and duration of El Niño and La Niña using the Oceanic Niño Index (ONI; shown for mid-2018 through 2019 in Fig. 4.1). The ONI is the 3-month (seasonal) running average of sea surface temperature (SST) anomalies in the Niño-3.4 region (5°N–5°S, 170°–120°W), currently calculated as the departure from the 1986–2015 base period mean. El Niño is classified when the ONI ≥ +0.5°C for at least five consecutive, overlapping seasons. La Niña is similarly defined but for ONI ≤ −0.5°C.

Using the ONI, the minimum threshold for El Niño was reached in September–November (SON) 2018, but the CPC did not declare the onset of El Niño until ocean–atmosphere coupling became evident in January 2019 (Bell et al. 2019). ONI values peaked and remained near +0.8°C for five overlapping seasons (October–December [OND] until March–May [MAM]), then decreased before El Niño ended in May–July (MJJ) 2019. This episode was categorized as weak because the ONI remained between +0.5°C and +0.9°C.

The ONI remained positive throughout 2019, and the central Pacific remained warmer than usual. However, the remainder of the year was classified as ENSO-neutral as ONI values decreased to a minimum of +0.1°C during July–September (JAS) and August–October (ASO). During the autumn and early winter, the ONI increased to +0.5°C in OND and +0.6°C in November–January (NDJ), but the ocean–atmosphere coupling, which is normally an intrinsic aspect of El Niño, was not present during this season.

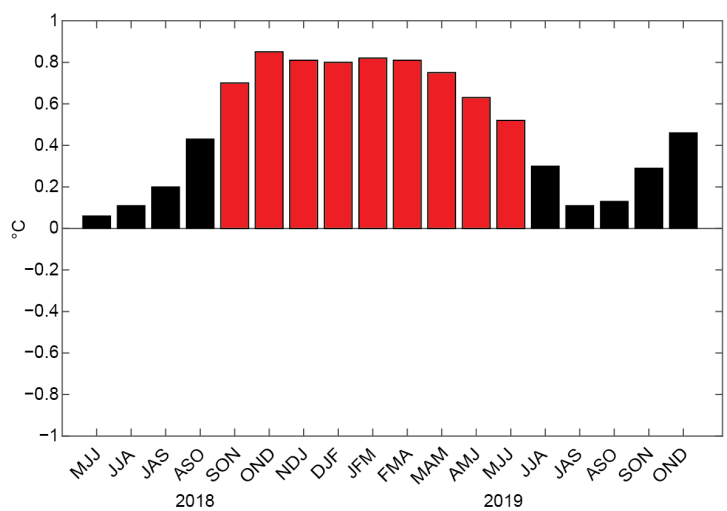

Fig. 4.1. Time series of the ONI (°C) from mid-2018 through 2019. Overlapping 3-month seasons are labeled on the x-axis, with initials indicating the first letter of each month in the season. Red bars indicate positive values in excess of +0.5°C. ONI values are derived from the ERSST-v5 dataset (Huang et al. 2017) and are based on departures from the 1986–2015 period monthly means.

Unauthenticated | Downloaded 12/18/20 02:55 PM UTC

1) Oceanic conditions

Seasonal sea surface temperatures (SSTs) and anomalies during December–February (DJF) 2018/19 through SON 2019 are shown in Fig. 4.2. The El Niño during DJF and MAM is indicated by positive SST anomalies across the central and eastern equatorial Pacific Ocean (Figs. 4.2a–d). Throughout the event, anomalies exceeding +1.0°C were seen in the central and east-central equatorial Pacific. These conditions reflected a weaker-than-average equatorial cold tongue in the eastern Pacific and an eastward expansion of the western Pacific warm pool (approximated by SSTs above 29°C) to well east of the date line (near 160°W; Fig. 4.2d).

Following the demise of El Niño, equatorial SST anomalies in the central Pacific Ocean remained quite high (near or above +1.0°C) throughout the year, while the anomalies decreased in the eastern equatorial Pacific, returning to near zero during June–August (JJA) and SON 2019 (Figs. 4.2f,h). A sizable region of 30°C temperatures covered the western equatorial Pacific Ocean, extending to the date line (Figs. 4.2e,g). Correspondingly, SST anomalies increased to +1.5°C in the western equatorial Pacific (~170°E) during SON (Fig. 4.2h).

Consistent with the SST evolution, subsurface temperatures during DJF 2018/19 and MAM 2019 were above average across most of the equatorial Pacific (Figs. 4.3a,b). This warming reflected deepening of the oceanic thermocline and reduced upwelling that accompanies El Niño. Although ENSO-neutral conditions returned by summer, temperature anomalies near the date line remained greater than +1.0°C between the surface and 150-m depth (Figs. 4.3c,d).

In contrast, in the far eastern equatorial Pacific, the thermocline was shallower than average, consistent with the below-average temperatures in this region during JJA (Fig. 4.3c). By SON, the thermocline and subsurface temperatures were near average across most of the equatorial Pacific Ocean.

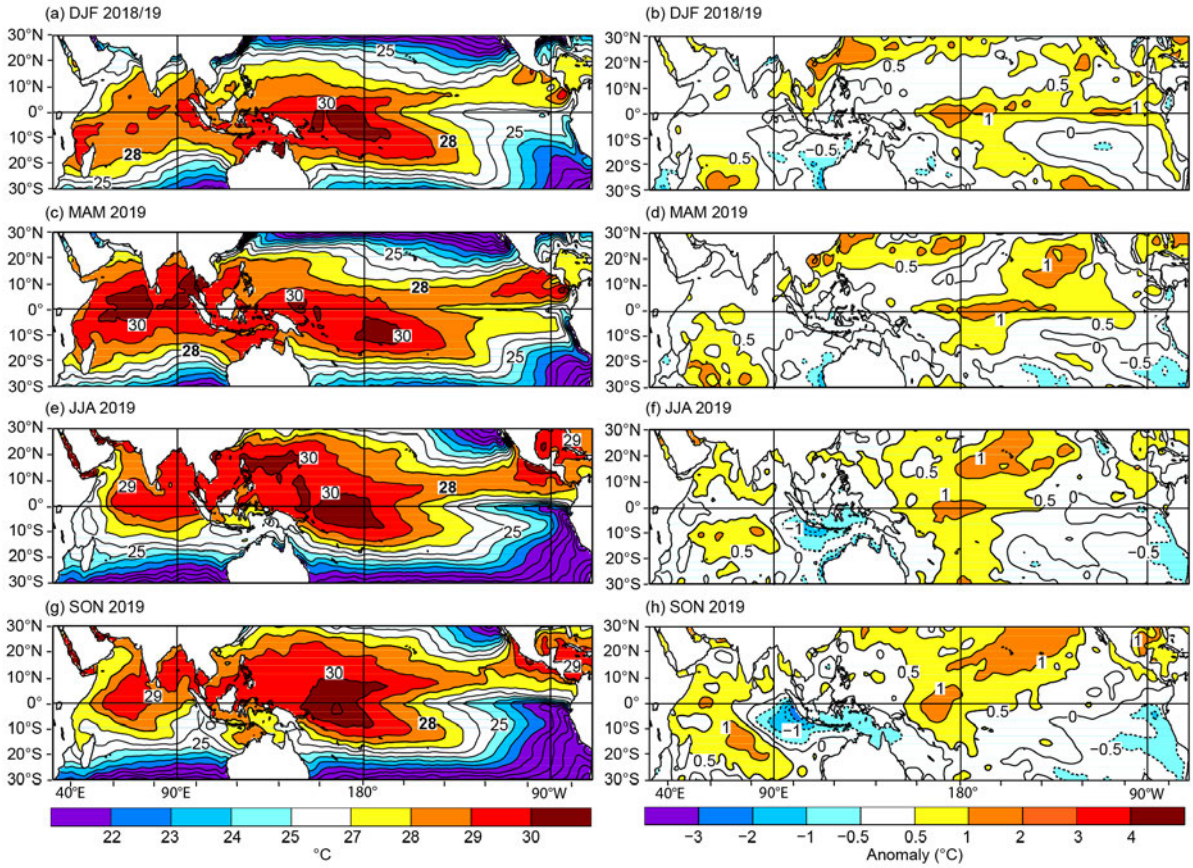

Fig. 4.2. Seasonal SST (left) and anomaly (right) for (a),(b) DJF 2018/19, (c),(d) MAM 2019, (e),(f) JJA 2019, and (g),(h) SON 2019. Contour interval for SST is 1°C. For SST anomaly, contour interval is 0.5°C for anomalies between ±1°C, and 1°C for anomalies > 1°C and < –1°C. Anomalies are departures from the 1981–2010 seasonal adjusted OI climatology (Reynolds et al. 2002).

Unauthenticated | Downloaded 12/18/20 02:55 PM UTC

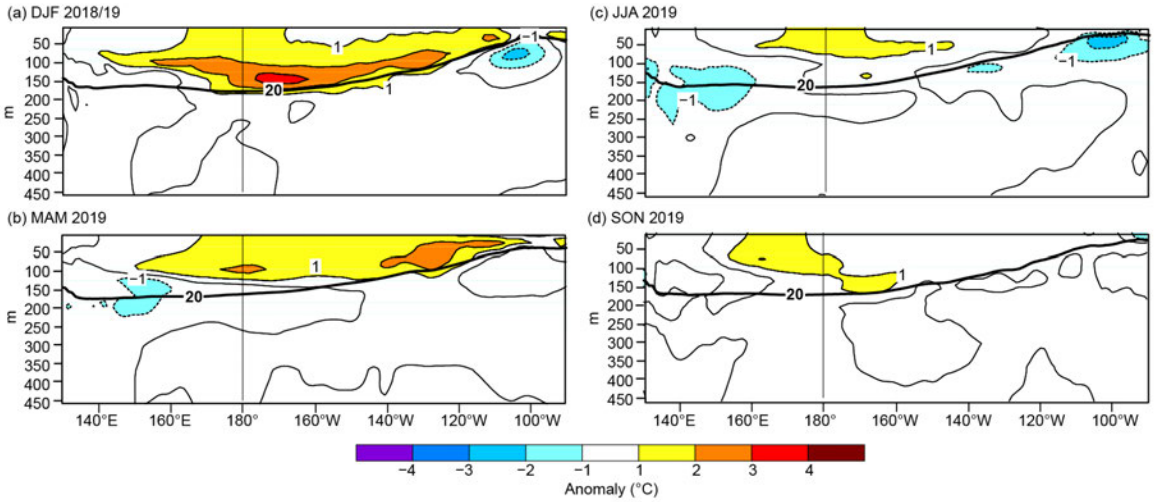

Fig. 4.3. Equatorial depth–longitude section of Pacific Ocean temperature anomalies (°C) from the 1981–2010 mean averaged between 5°N and 5°S during (a) DJF 2018/19, (b) MAM 2019, (c) JJA 2019, and (d) SON 2019. The 20°C isotherm (thick solid line) approximates the center of the thermocline. The data are derived from an analysis system that assimilates oceanic observations into an oceanic general circulation model (Behringer et al. 1998).

2) Atmospheric circulation, temperature, and precipitation anomalies during December–February 2018/19

The patterns of tropical convection and winds during DJF 2018/19 generally reflected El Niño (Figs. 4.4a, 4.5a). In particular, tropical convection (measured by Outgoing Longwave Radiation [OLR]) was enhanced near the date line (green shading) and suppressed over Indonesia (brown shading). Low-level (850 hPa) tropical wind anomalies were westerly over the western Pacific Ocean during DJF (Fig. 4.4a), reflecting a weakening of the trade winds, an indicator of a weaker Pacific Walker circulation (Bjerknes 1969).

In the upper atmosphere (200 hPa), tropical wind anomalies were mostly cross-equatorial during DJF 2018/19, with flow from the Northern Hemisphere (NH) subtropics to the Southern Hemisphere (SH) over the eastern Pacific (Fig. 4.5a). Upper-level wind anomalies reflected anomalous divergence in association with the enhanced convection near the date line. Adjacent to this region, two anomalous upper-level anticyclones flanked the equator, consistent with El Niño.

Over the Pacific–North American region, anomalies of 500-hPa heights and upper-level winds during DJF 2018/19 generally did not match those conventionally associated with El Niño. The strengthened and southern-shifted

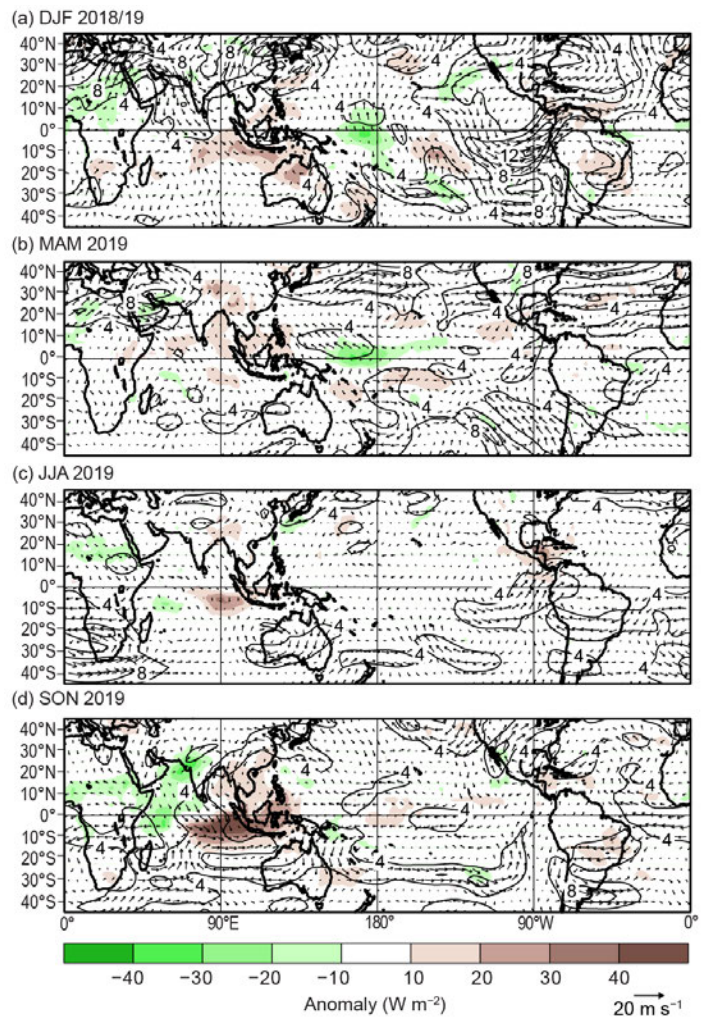

Fig. 4.4. Anomalous 850-hPa wind vectors and speed (contour interval is 2 m s^{-1}) and anomalous OLR (shaded, W m^{-2}) during (a) DJF 2018/19, (b) MAM 2019, (c) JJA 2019, and (d) SON 2019. Reference wind vector is below right of color bar. Anomalies are departures from the 1981–2010 period monthly means. (Source: NCEP–NCAR reanalysis [Kalnay et al. 1996].)

Unauthenticated | Downloaded 12/18/20 02:55 PM UTC

jet stream was only evident over the far eastern North Pacific Ocean instead of across the central North Pacific Ocean as expected with El Niño (Fig. 4.5a). Despite the lack of a clear El Niño footprint, the anomalous circulation was linked to increased precipitation over California, the southeastern United States, and Florida. However, enhanced precipitation was also widespread over the entire contiguous United States, with the exception of the Pacific Northwest and most of Texas, where near- to slightly-below-average precipitation occurred. As with the 500-hPa height anomalies, the temperature anomalies over North America were also not consistent with El Niño with below-average temperatures over western Canada and the north-central United States, and above-average temperatures over the southern tier of the United States (see sections 7b1 and 7b2).

In other parts of the world, El Niño during DJF is historically associated with positive temperature anomalies over the northern half of South America, Australia, Indonesia, southeast Asia, and southern Africa (Halpert and Ropelewski 1992). All of these were apparent during DJF 2018/19 (see relevant temperature sections in Chapter 7 for details), though undoubtedly with a partial contribution from the long-term climate change warming signal as well (see section 2b1). El Niño was also likely associated with above-average precipitation across most of the southern tier of the United States, Uruguay, and southeastern China during DJF 2018/19 (see relevant precipitation sections in Chapter 7 for details; Ropelewski and Halpert 1989). Likewise, El Niño likely played some role in below-average precipitation over parts of southern Chile, northern South America, South Africa, Indonesia, and Australia.

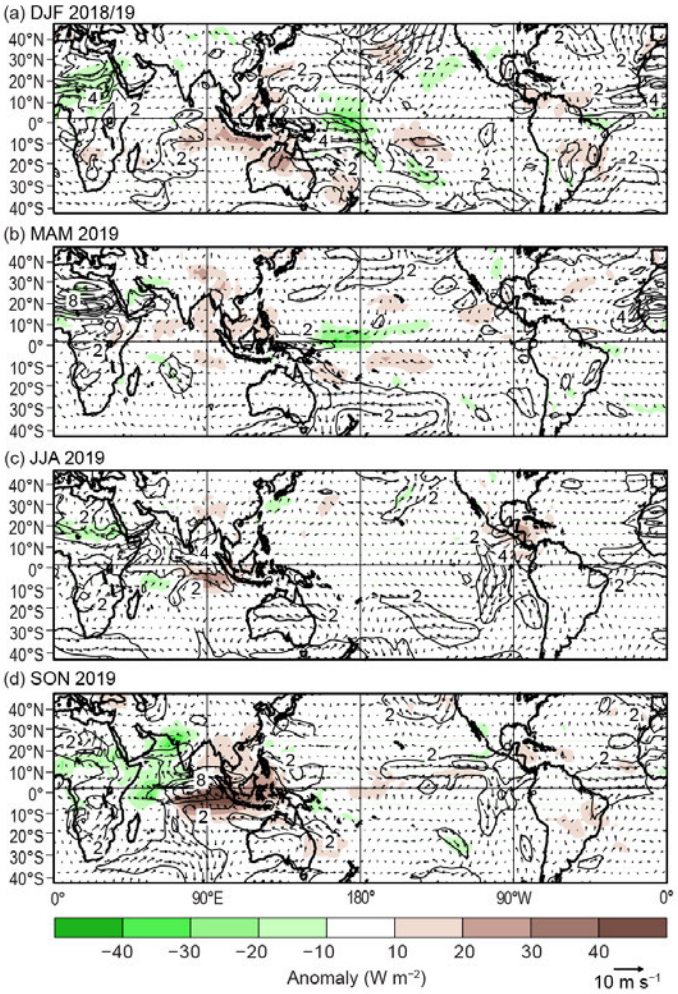

Fig. 4.5. Anomalous 200-hPa wind vectors and speed (contour interval is 4 m s^{-1}), and anomalous OLR (shaded, W m^{-2}), during (a) DJF 2018/19, (b) MAM 2019, (c) JJA 2019, and (d) SON 2019. Reference wind vector is below right of color bar. Anomalies are departures from the 1981–2010 period monthly means. (Source: NCEP–NCAR reanalysis [Kalnay et al. 1996].)

3) Atmospheric circulation, temperature, and precipitation anomalies during March–May through September–November 2019

The pattern of wind anomalies over the equatorial Pacific Ocean changed from DJF to MAM 2019, with mostly near-average low-level winds (Fig. 4.4b) and anomalous upper-level easterlies over the western Pacific Ocean during MAM (Fig. 4.5b). By this season, the El Niño was weakening from its boreal winter maximum. However, the East Asia–North Pacific jet stream was stronger than average across most of the extratropical oceans (Fig. 4.5b), which is typical of El Niño. Likewise, enhanced precipitation continued over California and much of the contiguous United States (see section 7b2). Temperatures over the United States, however, were largely a continuation of the DJF anomalies and not consistent with El Niño. Later in the year, the lower-level and upper-level winds were mostly near average over the equatorial Pacific (Figs. 4.4c,d and 4.5c,d). During SON, convection was suppressed over the Maritime Continent, mostly in

Unauthenticated | Downloaded 12/18/20 02:55 PM UTC

association with the strengthening of the Indian Ocean dipole (IOD; section 4h). While SST anomalies were positive over the western and central equatorial Pacific Ocean, there was no corresponding increase in convection. In fact, OLR was weakly suppressed near the date line (Figs. 4.4d, 4.5d).

c. Tropical intraseasonal activity—S. Baxter, C. Schreck, and G. D. Bell

Tropical intraseasonal variability was especially prominent during 2019. Two leading aspects of this variability were the Madden-Julian Oscillation (MJO; Madden and Julian 1971, 1972, 1994; Zhang 2005) and convectively coupled equatorial waves (Wheeler and Kiladis 1999; Kiladis et al. 2009), which include equatorial Rossby waves and atmospheric Kelvin waves. There were three distinct periods of MJO activity in 2019 spanning a total of approximately eight months (Fig. 4.6), which were interspersed with the convectively coupled waves (Fig. 4.7). Between the MJO periods, the tropical convective anomalies were dominated by lower frequency variability and convectively coupled waves.

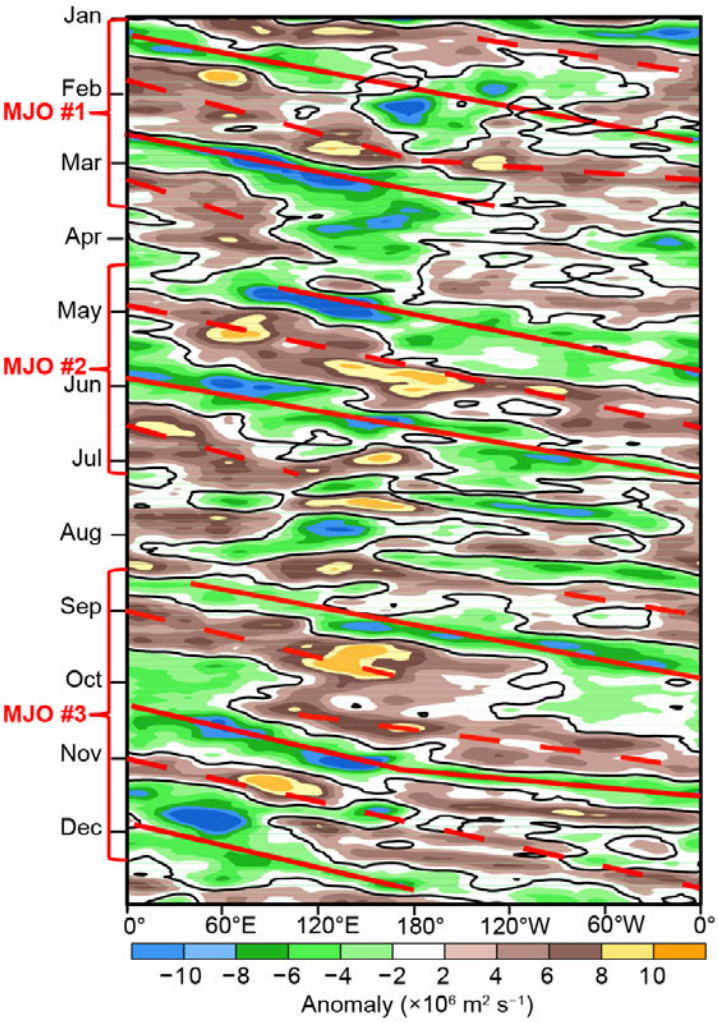

Fig. 4.6. Time–longitude section for 2019 of 5-day running anomalous 200-hPa velocity potential (× 10^6 $m^2 s^{-1}$) averaged between 5°N–5°S. For each day, the period mean is removed prior to plotting. Green (brown) shading highlights likely areas of anomalous divergence and rising motion (convergence and sinking motion). Red lines and labels highlight the main MJO episodes. Anomalies are departures from the 1981–2010 base period daily means. (Source: NCEP–NCAR reanalysis [Kalnay et al. 1996].)

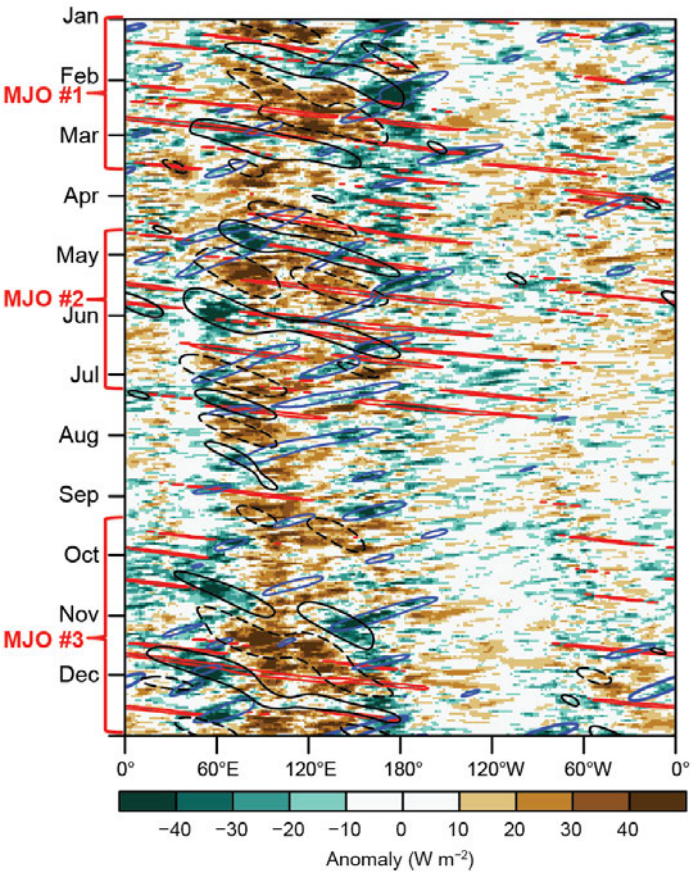

Fig. 4.7. Time–longitude section for 2019 of anomalous OLR ($W m^{-2}$) averaged between 10°N–10°S. Negative anomalies indicate enhanced convection, positive anomalies indicate suppressed convection. Contours identify anomalies filtered for the MJO (black) and atmospheric Kelvin waves (red), and equatorial Rossby waves (blue). Red labels highlight the main MJO episodes. Contours are drawn at ±10 $W m^{-2}$, with the enhanced (suppressed) convective phase of these phenomena indicated by solid (dashed) contours. Anomalies are departures from the 1981–2010 base period daily means.

Unauthenticated | Downloaded 12/18/20 02:55 PM UTC

The MJO is a leading intraseasonal climate mode of tropical convective variability. Its convective anomalies often have a similar spatial scale to El Niño–Southern Oscillation (ENSO) but differ in that they exhibit a distinct eastward propagation and generally traverse the globe in 30–60 days. The MJO affects weather patterns around the globe (Zhang 2013), including monsoons (Krishnamurti and Subrahmanyam 1982; Lau and Waliser 2012), tropical cyclones (TCs; Mo 2000; Frank and Roundy 2006; Camargo et al. 2007; Schreck et al. 2012; Diamond and Renwick 2015), and extratropical circulations (Knutson and Weickmann 1987; Kiladis and Weickmann 1992; Mo and Kousky 1993; Kousky and Kayano 1994; Kayano and Kousky 1999; Cassou 2008; Lin et al. 2009; Riddle et al. 2012; Schreck et al. 2013; Baxter et al. 2014). The MJO is often episodic, with periods of moderate-to-strong activity followed by little or no activity. The MJO tends to be most active during ENSO-neutral and weak ENSO periods and is often absent during strong El Niño events (Hendon et al. 1999; Zhang and Gottschalck 2002; Zhang 2005). Common metrics for identifying the MJO include time–longitude plots of anomalous 200-hPa velocity potential (Fig. 4.6) and Outgoing Longwave Radiation (OLR; Fig. 4.7), as well as the Wheeler–Hendon (2004) Real-time Multivariate MJO (RMM) index (Fig. 4.8). In the time–longitude plots, the MJO exhibits eastward propagation from upper-left to lower-right. In the RMM, the MJO propagation and intensity are seen as large, counter-clockwise circles around the origin. When considered together, these diagnostics point to three prolonged MJO episodes during 2019. MJO #1 was a strong and long-lasting episode that continued from late 2018 (Baxter et al. 2019) through mid-March 2019. MJO #2 began in mid-April and persisted into early July, while MJO #3 began in mid-August and lasted through late December. All three MJO periods were associated with either westerly wind bursts (WWBs) or trade wind surges (TWS) over the central Pacific (Fig. 4.9a).

MJO #1 featured a zonal wave-1 pattern of strong convective anomalies. Its periodicity was approximately 30 days during January, slowing to about 45 days during February and March (Figs. 4.6, 4.8a). The plot of anomalous velocity potential (Fig. 4.6) shows that MJO #1 circumnavigated the globe nearly two times during January–March. The RMM index indicates the event was strongest in late February and early March (Fig. 4.8a). During late March, coherent eastward propagation gave way to a more stationary convective pattern with upper-level divergence (convergence) centered over the west-central Pacific Ocean (eastern Indian Ocean).

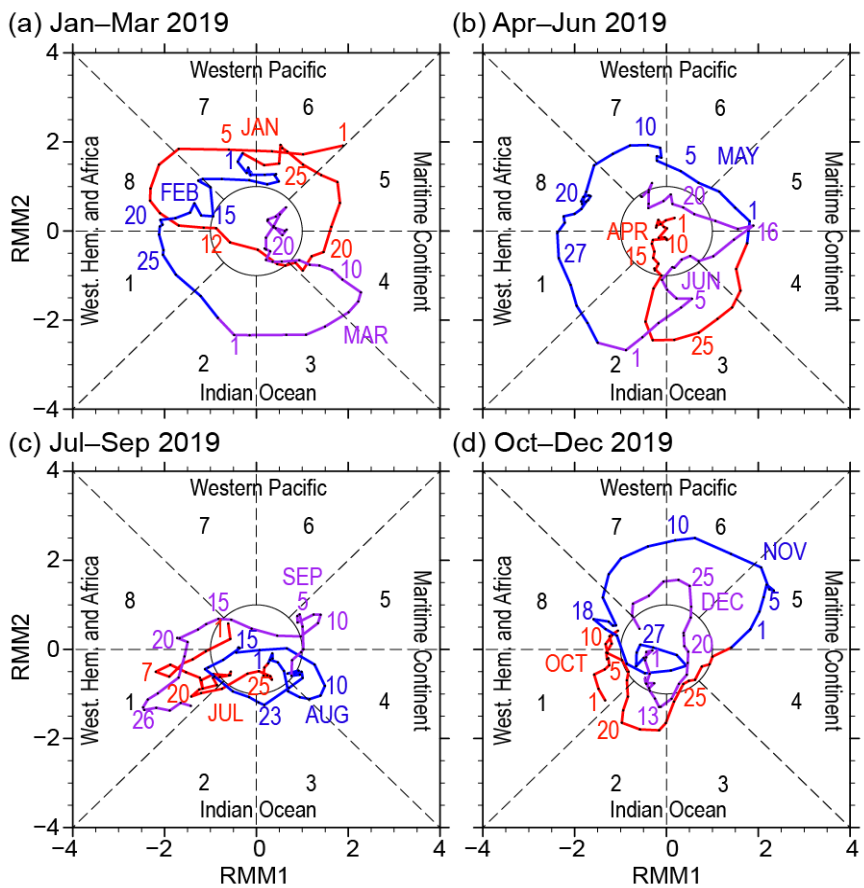

Fig. 4.8. Wheeler–Hendon (2004) Real-time Multivariate MJO (RMM) index for (a) Jan–Mar, (b) Apr–Jun, (c) Jul–Sep, and (d) Oct–Dec 2019. Each point represents the MJO amplitude and location on a given day, and the connecting lines illustrate its propagation. Amplitude is indicated by distance from the origin, with points inside the circle representing weak or no MJO. The eight phases around the origin identify the region experiencing enhanced convection, and counter-clockwise movement is consistent with eastward propagation.

Unauthenticated | Downloaded 12/18/20 02:55 PM UTC

Impacts from MJO #1 included notable WWB activity over the equatorial Pacific during January and February (Fig. 4.9a). These WWBs initiated and reinforced the strongest downwelling oceanic Kelvin wave observed in 2019 (dashed line, Fig. 4.9b), which resulted in positive heat content anomalies exceeding 2°C in early March. This downwelling wave reached the west coast of South America during April. Prominent TWS were notably absent during early 2019.

MJO #2 occurred from mid-April to early July. Its periodicity was about 45 days, with nearly canonical eastward propagation throughout its duration. The RMM index showed peak amplitude during mid- to late May (Fig. 4.8b). Eastward propagation broke down during July, giving way to less coherent convective anomalies punctuated by westward-moving equatorial Rossby waves.

MJO #2 resulted in alternating low-level zonal wind anomalies over the western and central Pacific (Fig. 4.9a) that gave rise to both upwelling and downwelling oceanic Kelvin waves. TWS events in April and June, respectively, resulted in upwelling oceanic Kelvin waves seen as local minima in heat content anomalies (dotted lines, Fig. 4.9b). A WWB in May resulted in a downwelling oceanic Kelvin wave observed between the aforementioned upwelling periods.

The third and final MJO period of 2019 was associated with the emergence of a wave-1 convective pattern in late August. Both the RMM index and velocity potential anomalies reveal relatively slow propagation during mid-September through mid-October, when a westward-moving equatorial Rossby wave (Figs. 4.7, 4.9a) interfered with the overall MJO signal. This interference is seen as a distinct split in the MJO-suppressed phase during late September and early October (Fig. 4.6). A similar split is visible but less prominent in the enhanced MJO phase at the same time. Eastward propagation with a periodicity of nearly 40 days resumed in mid- to late October. MJO #3 reached peak amplitude in November (Fig. 4.8) as a very strong suppressed phase propagated across the Indian Ocean (Fig. 4.7). Canonical eastward propagation gave way to a fast-moving atmospheric Kelvin wave in late December.

MJO #3 resulted in two prominent WWB events and associated downwelling oceanic Kelvin waves in September and November, respectively. The first downwelling wave reached the South American coast in early December. A modest TWS in late October and the resulting upwelling separated the two downwelling waves. MJO #3 also appears to have played a role in modulating Atlantic hurricane activity. During 4–14 September, no new named storm formations occurred when the MJO was producing enhanced upper-level divergence over the central and eastern Pacific

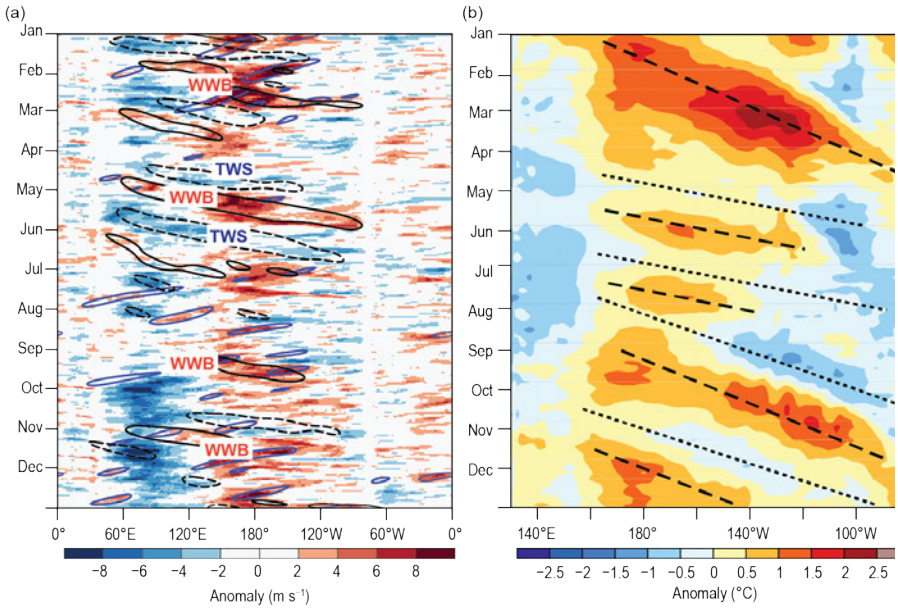

Fig. 4.9. (a) Time–longitude section for 2019 of anomalous 850-hPa zonal wind (m s^{-1}) averaged between 10°N–10°S. Contours identify anomalies filtered for the MJO (black), atmospheric Kelvin waves (red), and equatorial Rossby waves (blue). Significant WWB and TWS over the equatorial Pacific that resulted in notable downwelling and upwelling oceanic Kelvin waves are labeled. (b) Time–longitude section for 2019 of the anomalous equatorial Pacific Ocean heat content, calculated as the mean temperature anomaly between 0–300 m depth. Yellow/red (blue) shading indicates above- (below-) average heat content. Relative warming (dashed lines) and cooling (dotted lines) due to downwelling and upwelling equatorial oceanic Kelvin waves are indicated. Anomalies are departures from the 1981–2010 base period pentad means. Data in (b) are derived from an analysis system that assimilates oceanic observations into an oceanic general circulation model (Behringer et al. 1998).

Unauthenticated | Downloaded 12/18/20 02:55 PM UTC

(Fig. 4.6), a pattern known to increase vertical wind shear over the tropical Atlantic and be unfavorable for tropical cyclogenesis (Klotzbach 2010). In contrast, the MJO likely contributed to enhanced Atlantic TC activity during 14 September–2 October (five Atlantic named storms) and 18–30 October (four Atlantic named storms). In both periods, the suppressed phase of the MJO produced anomalous upper-level convergence over the central equatorial Pacific, a pattern that acts to decrease the vertical wind shear and increase activity over the tropical Atlantic.

d. Intertropical convergence zones

1) Pacific—N. Fauchereau

Tropical Pacific rainfall patterns are dominated by two convergence zones, the Intertropical Convergence Zone (ITCZ; Schneider et al. 2014) north of the equator and the South Pacific Convergence Zone (SPCZ; Vincent 1994). Figure 4.10 summarizes their combined behavior during 2019 using rainfall estimated from satellite microwave and infrared data in a product known as CMORPH (Joyce et al. 2004). Rainfall transects over 20°N–30°S are presented for each quarter of the year, averaged across successive 30°-longitude bands, starting in the western Pacific at 150°E–180°. The 2019 seasonal variation is compared against the 1998–2018 climatology.

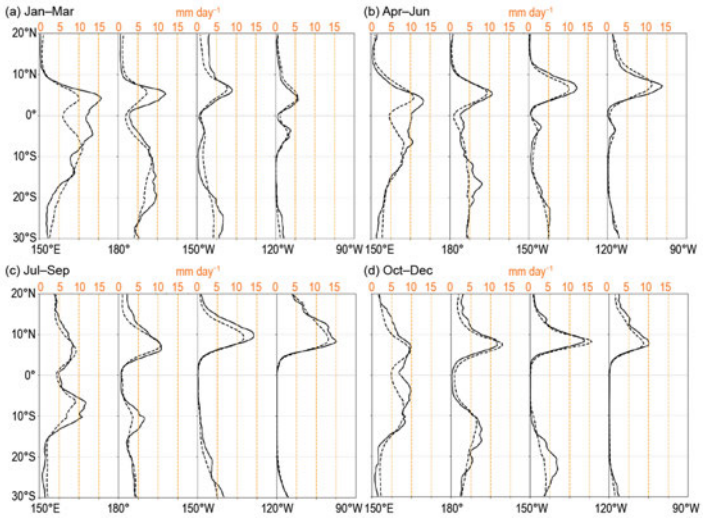

Fig. 4.10. Rainfall rate (mm day^{-1}) from CMORPH analysis for the cross-section between 20°N and 30°S, for (a) Jan–Mar, (b) Apr–Jun, (c) Jul–Sep, and (d) Oct–Dec 2019. Each quarter's panels show the 2019 rainfall (solid line), and the 1998–2018 climatology (dotted line), for four 30° sectors from 150°E–180° to 120°–90°W. (Source: CMORPH [Joyce et al. 2004].)

From January through March, the positive sea surface temperature (SST) anomalies in the central Pacific were associated with considerable increases in precipitation around the date line. During this time, large departures from normal rainfall were recorded in February just south of the equator (Figs. 4.10a, 4.11a) within the SPCZ. A strongly intensified ITCZ developed in March (Fig. 4.11b). Conversely, well-below-normal rainfall was recorded in the western Pacific and the Maritime Continent in February. Persistent dryness affected many islands within Micronesia during the first quarter of 2019 (PEAC 2019, Pacific ENSO update).

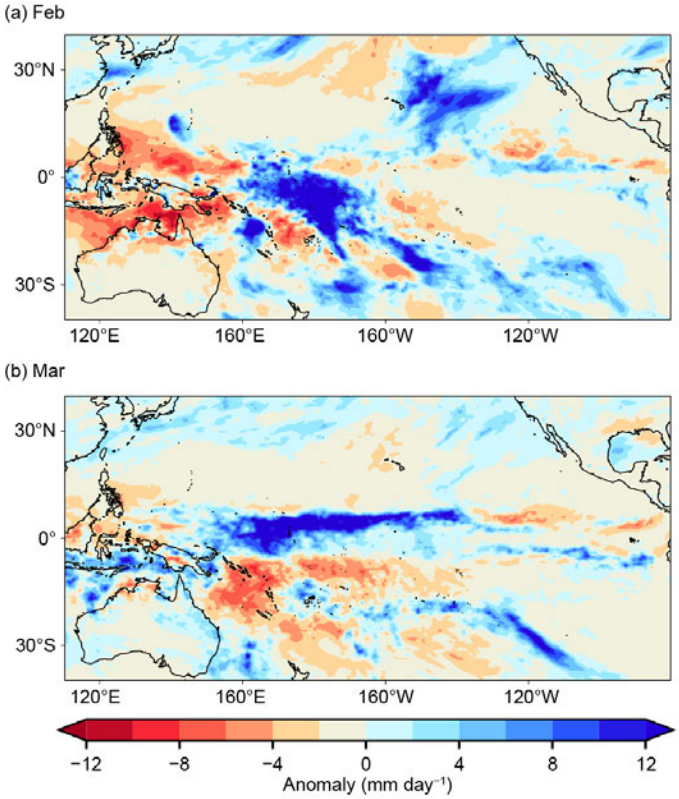

Fig. 4.11. Rainfall anomalies (mm day^{-1}) for (a) Feb and (b) Mar 2019. The anomalies are calculated with respect to the 1998–2018 climatology. (Source: CMORPH [Joyce et al. 2004].)

Figure 4.12 shows a more detailed comparison of the western Pacific CMORPH rainfall transect during January–March (JFM) 2019 relative to all other years in the satellite dataset. During JFM, the ITCZ was quite strong, with the most exceptional rainfall anomalies—approaching and exceeding the largest values in the CMORPH dataset—recorded within the ITCZ in the northern Pacific between 150°E

Unauthenticated | Downloaded 12/18/20 02:55 PM UTC

and 180°. This pattern is atypical of the composite anomalies associated with more canonical El Niño conditions. However, it is consistent with an atmospheric response to positive SST anomalies centered around and west of the date line, noting the amplitude of the rainfall anomalies observed are still somewhat unprecedented.

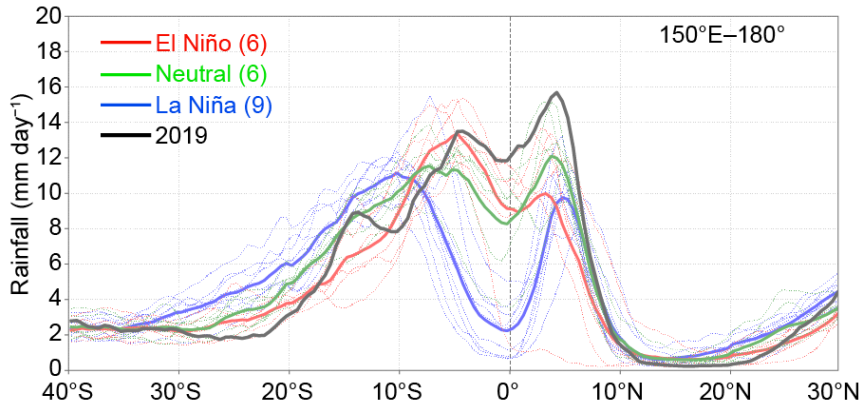

Fig. 4.12. Rainfall rate (mm day^{-1}) for Jan–Mar, for each year 1998 to 2018, averaged over the longitude sector 150°E–180°. The cross-sections are color-coded according to NOAA's ONI, except 2019, which is shown in black. Dotted lines are individual years, and solid lines are the average over all years in each ENSO phase. Inset legend indicates how many years went into each composite. (Source: CMORPH [Joyce et al. 2004].)

Rainfall anomalies broadly consistent with weak El Niño conditions persisted until about July, after which most El Niño–Southern Oscillation (ENSO) indicators dipped below El Niño thresholds and ENSO-neutral conditions took hold. However, the continued development of a positive Indian Ocean dipole (IOD; one of the strongest on record) influenced rainfall patterns from September through the end of the year, especially in the western Pacific (section 4h). During this period, dry conditions developed and impacted some areas of the western Pacific and Maritime Continent again. At the same time, the ITCZ shifted north of its climatological position in the central and eastern equatorial Pacific east of the date line.

In November 2019, SST anomalies increased in the central and western Pacific. The continuation of positive IOD conditions well into December led to dry conditions forming across parts of the western Pacific and the Maritime Continent. The SPCZ was clearly shifted northeast of its climatological position in the southwest Pacific during December, leading to dry conditions across Papua New Guinea, the Solomon Islands, Vanuatu, and New Caledonia.

2) Atlantic—A. B. Pezza and C. A. S. Coelho

The Atlantic ITCZ is a well-organized convective band that oscillates between approximately 5°–12°N during July–November and 5°N–5°S during January–May (Waliser and Gautier 1993; Nobre and Shukla 1996). Equatorial atmospheric Kelvin waves can modulate ITCZ intraseasonal variability (Guo et al. 2014). ENSO and the Southern Annular Mode (SAM) can also influence the ITCZ on interannual time scales (Münnich and Neelin 2005). The SAM, also known as the Antarctic Oscillation, describes the north–south movement of the westerly wind belt that circles Antarctica, dominating the middle to higher latitudes of the Southern Hemisphere (SH). The changing position of the westerly wind belt influences the strength and position of cold fronts and midlatitude storm systems. During a positive SAM event, the belt of strong westerly winds contracts toward Antarctica. Conversely, a negative SAM event reflects an expansion of the belt of strong westerly winds towards the equator. The SAM, which was mostly positive in recent years, started to oscillate between predominantly neutral and negative phases in 2019, with negative values developing late in the year (see section 6b). This was consistent with an El Niño-like state in the Pacific, with weak coupling between equatorial Pacific oceanic and atmospheric conditions.

This transition state was associated with an Atlantic ITCZ oscillating around its climatological position. Occasional southern excursions during March and April contributed to positive rainfall anomalies offshore and in some small areas of northeastern Brazil during the first half of the year (Fig. 4.13). These bursts were associated with an anomalously warm Atlantic Ocean south of the equator and a cool North Atlantic during the first half of the year. This SST pattern reverted to a

Unauthenticated | Downloaded 12/18/20 02:55 PM UTC

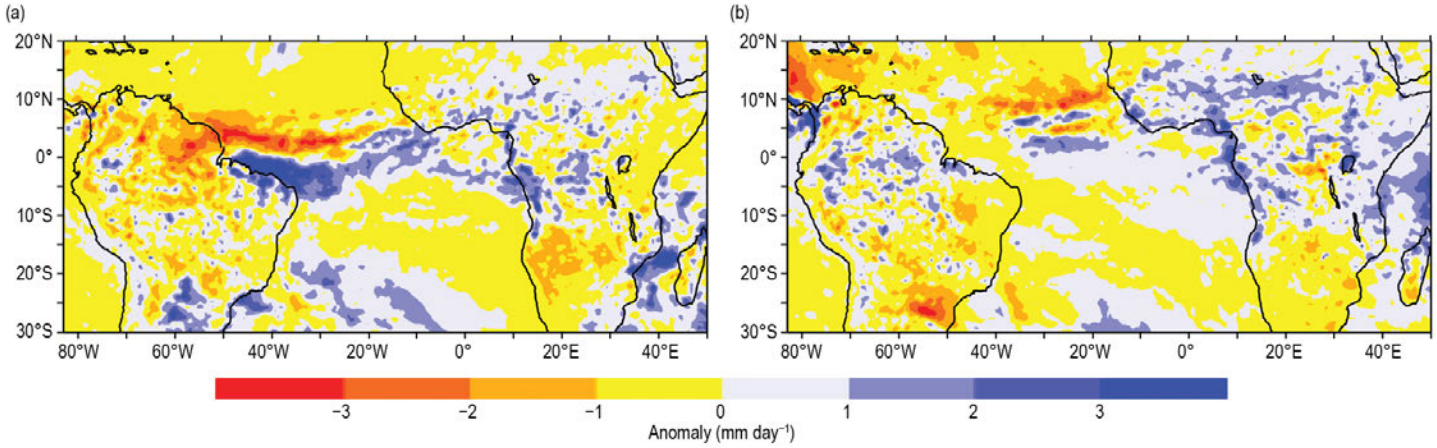

Fig. 4.13. Observed precipitation anomaly for tropical and subtropical South America (mm day^{-1}) during (a) Jan–Jun and (b) Jul–Dec 2019. Anomalies are calculated based on a 1998–2018 climatology. (Source: CMORPH [Joyce et al. 2004].)

more neutral set up from June to October, and then re-intensified toward the end of the year.

The Atlantic Index (Pezza and Coelho 2019), as defined by the SST south of the equator minus the SST north of the equator over key areas of influence for the ITCZ, reflects well the role of the north–south gradient mechanism highlighted above for 2019, with the ITCZ tending to shift toward the warmer side of this gradient (Fig. 4.14). A weaker subtropical South Atlantic anticyclone associated with a negative SAM also contributed to re-establish a positive SST anomaly pattern south of the equator toward the end of the year. This pattern resulted in an abrupt increase in the Atlantic Index (Fig. 4.14). This increase is also consistent with possible atmospheric Kelvin wave propagation, although the ITCZ was too far north to be impacted.

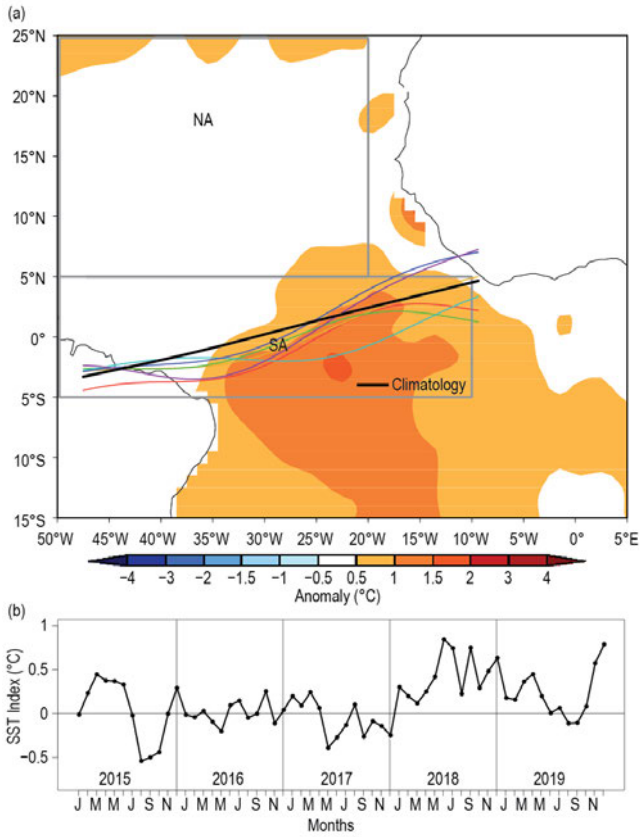

Fig. 4.14. (a) Atlantic ITCZ position inferred from OLR (Liebmann and Smith 1996) during Mar 2019. The colored thin lines indicate the approximate position for the six pentads of the month. The black thick line indicates the climatological position for Mar. SST anomalies for Mar 2019 based on the 1982–2018 climatology are shaded (°C). Boxes indicate areas used to calculate the Atlantic index. (b) Atlantic index for 2015–19, based on monthly OISST (Smith et al. 2008) anomaly time series averaged over the South Atlantic sector (SA box, 10°–50°W, 5°N–5°S) minus the same averaged over the North Atlantic sector (NA box, 20°–50°W, 5°–25°N). A positive index indicates favorable conditions for enhanced Atlantic ITCZ activity south of the equator.

e. Global monsoon summary—B. Wang and Q. He

The global monsoon is the dominant mode of annual tropical–subtropical precipitation and circulation variability and thus a critical part of Earth's climate system (Wang and Ding 2008). Figure 4.15 shows global precipitation anomalies, focusing on monsoon rainfall anomalies, especially over the land monsoon region, for the monsoon seasons in the (a) Southern Hemisphere (SH; November 2018–April 2019) and (b) Northern Hemisphere (NH; May–October 2019), which constitute the global monsoon year of 2018/19. Figure 4.16 shows the time series of monsoon precipitation and low-level circulation indices (Yim et al. 2014) for each of the eight regional monsoons. Note that these precipitation

Unauthenticated | Downloaded 12/18/20 02:55 PM UTC

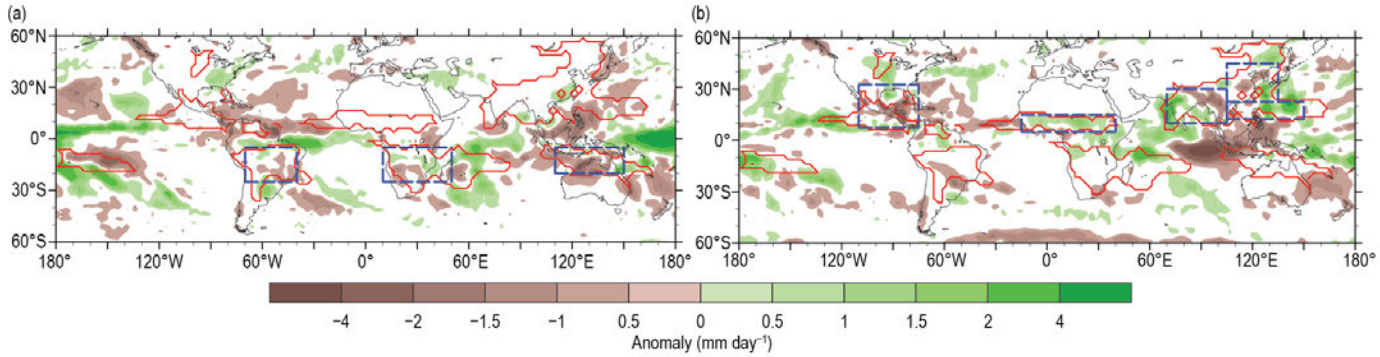

Fig. 4.15. Precipitation anomalies (mm day^{-1}) averaged for (a) the SH monsoon season: Nov 2018–Apr 2019 and (b) the NH monsoon season: May–Oct 2019. Red lines outline the global monsoon precipitation domain defined by two climatological conditions: first, the local monsoon season precipitation minus that of the cool season exceeds 300 mm and second, the monsoon season precipitation constitutes at least 55% of the total annual amount (Wang and Ding 2008). Precipitation indices for each regional monsoon are defined by the areal mean precipitation in the corresponding rectangular regions (dashed blue), which are highly correlated with that of the corresponding real regional monsoon domains (Table 4.1). (Source: GPCP [Huffman et al. 2009].)

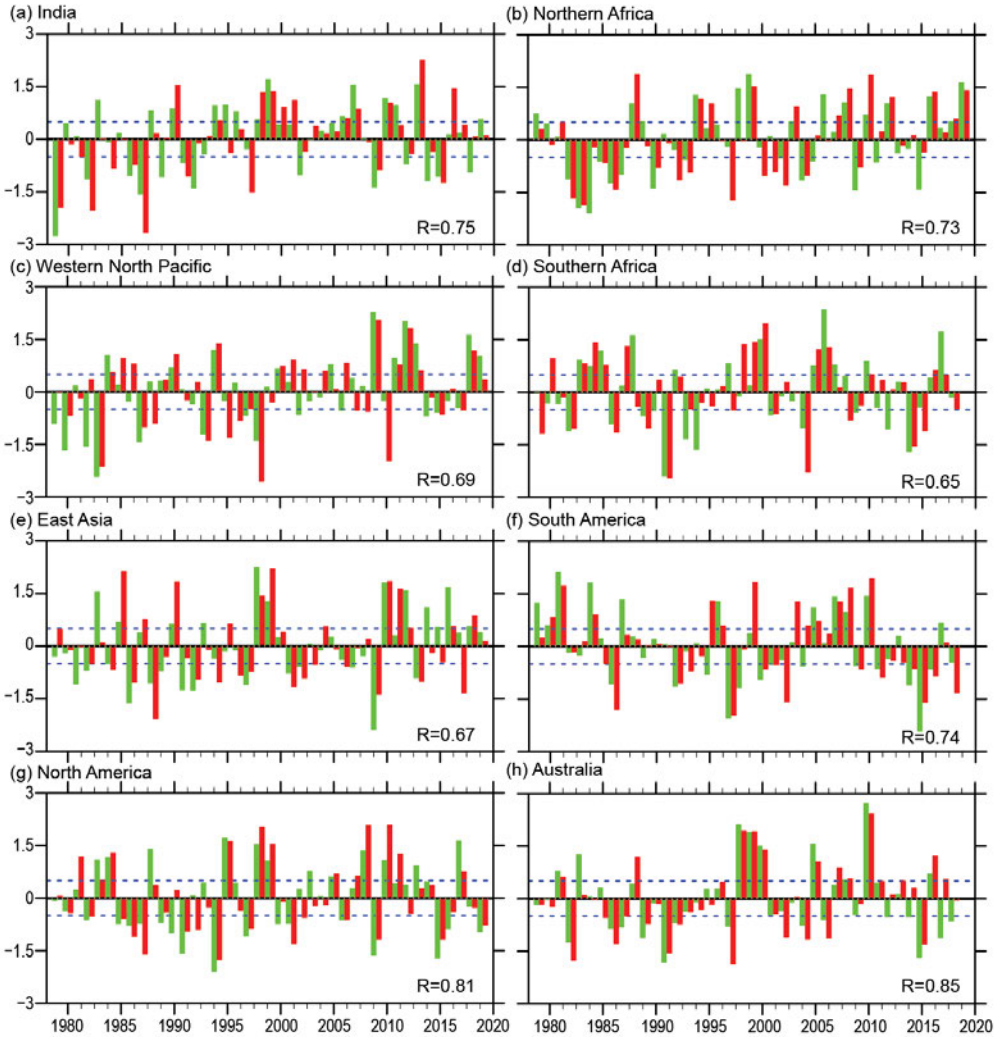

Fig. 4.16. Summer mean precipitation (green) and circulation (red) indices for each of eight regional monsoons defined in Table 4.1, normalized by their corresponding std. dev. In each panel, R denotes the correlation coefficient between the seasonal mean precipitation and circulation indices (sample size: 40). Dashed lines indicate ±0.5 std. dev. The monsoon seasons are May–Oct for the NH and Nov–Apr for the SH. The normalization method is discussed in Yim et al. (2014). (Source: GPCP for precipitation; ERA-5 for circulation.)

Unauthenticated | Downloaded 12/18/20 02:55 PM UTC

indices represent the average precipitation amount over both land and ocean areas in the boxed regions shown in Fig. 4.16. The definitions of the circulation indices for each monsoon region are provided in Table 4.1. In most regions, the precipitation and circulation indices are well correlated, with correlation coefficients ranging from 0.68 to 0.86, except for the southern African monsoon. The correlation coefficients in Table 4.1 were computed using monthly mean data from 1979 to 2018 (sample size is 160). The precipitation and circulation indices together provide consistent measurements of the strength of each regional monsoon system.

Global land monsoon precipitation is strongly influenced by tropical sea surface temperature (SST) anomalies, especially those associated with the El Niño–Southern Oscillation (ENSO; Wang et al. 2012). As shown in Fig. 4.15a, during the SH monsoon season, precipitation increased over the central-western Pacific and was suppressed over the Maritime Continent–Australian monsoon region (Fig. 4.15a). This pattern was consistent with the SST anomalies associated with the weak El Niño that occurred from January to July 2019. The South American monsoon was characterized by below-normal precipitation and circulation intensity, especially a significant weakening of the South American monsoon circulation (Fig. 4.16g). The Australian summer monsoon region also received markedly less precipitation than normal, but the strength of the corresponding circulation was near normal (Fig. 4.16h). The southern African summer monsoon precipitation was near normal, but the circulation intensity was below normal (Fig. 4.16f). Overall, the SH summer monsoon was generally below normal with reduced precipitation and monsoon circulation, although the degree of weakening varied in the three SH regional monsoons.

During the NH monsoon season, precipitation over the Maritime Continent was significantly below normal with a prominent reduction of precipitation to the west of Sumatra over the tropical eastern Indian Ocean (Fig. 4.15b). On a regional scale, the northern African monsoon was characterized by above-normal precipitation and circulation intensity, both of which reached ~1.5 std. dev. (Fig. 4.16e) above normal, indicating a strong monsoon year over northern Africa.

Table 4.1. (Modified from Yim et al. 2014). Definition of the regional summer monsoon circulation indices and their correlation coefficients (CCs) with the corresponding regional summer monsoon precipitation indices for the period 1979–2018. All circulation indices are defined by the meridional shear of the zonal wind at 850 hPa, which measures the intensity (relative vorticity) of the monsoon troughs at 850 hPa except for northern African (NAF) and East Asian (EA). The NAF monsoon circulation index is defined by the westerly monsoon strength: U850 (0°–15°N, 60°–10°W), and the EASM circulation index is defined by the meridional wind strength: V850 (20°–40°N, 120°–140°E), which reflects the east–west thermal contrast between the Asian continent and the western North Pacific. The precipitation indices are defined by the areal mean precipitation over the blue box regions shown in Fig. 4.15. The correlation coefficients were computed using monthly time series (160 summer months) (Jun–Sep [JJAS] in NH [1979–2018] and Dec–Mar [DJFM] in SH [1979/80–2018/19]). Bolded numbers represent significance at the 99% confidence level.

Region	Definition of the circulation index	CC
Indian (ISM)	U850 (5° –15°N, 40°–80°E) minus U850 (25°–35°N, 70°–90°E)	**0.69**
Western North Pacific (WNPSM)	U850 (5°–15°N, 100°–130°E) minus U850 (20°–35°N, 110°–140°E)	**0.80**
East Asian (EASM)	V850 (20°–40°N, 120°–140°E)	**0.70**
North American (NASM)	U850 (5°–15°N, 130°–100°W) minus U850 (20°–30°N, 110°–80°W)	**0.83**
Northern African (NAFSM)	U850 (0°–15°N, 60°–10°W)	**0.68**
South American (SASM)	U850 (20°–5°S, 70°–40°W) minus U850 (35°–20°S, 70°–40°W)	**0.82**
Southern African (SAFSM)	U850 (15°S-0°, 10°–40°E) minus U850 (25°–10°S, 40°–70°E)	**0.53**
Australian (AUSSM)	U850 (15°S–0°, 90°–130°E) minus U850 (30°–20°S, 100°–140°E)	**0.86**

Unauthenticated | Downloaded 12/18/20 02:55 PM UTC

Boreal summer precipitation over India was significantly above normal, but precipitation over Bangladesh and the Indo-China peninsula was below normal. The western North Pacific monsoon precipitation was ~1 std. dev. above normal (Fig. 4.16b). Both the East Asian summer monsoon rainfall and its circulation were near normal (Fig. 4.16c) with a dipolar pattern: above-normal precipitation over the East China Sea to western Japan and below-normal precipitation along the subtropical frontal zone extending from the middle Yangtze River Valley to the Korean peninsula (Fig. 4.15b). The North American monsoon was characterized by both below-normal precipitation and circulation intensity (Fig. 4.16d). Overall, total monsoon precipitation was above normal in the NH and below normal in the SH. There was a notable contrast between the Eastern and Western Hemispheres, with increased rainfall over the Eastern Hemisphere tropical monsoon regions and reduced rainfall over those of the Western Hemisphere (e.g., the American monsoon regions).

f. Tropical cyclones

1) Overview—H. J. Diamond and C. J. Schreck

The IBTrACS dataset comprises historical tropical cyclone (TC) best-track data from numerous sources around the globe, including all of the World Meteorological Organization (WMO) Regional Specialized Meteorological Centers (RSMCs; Knapp et al. 2010). This dataset represents the most complete compilation of global TC data. From these data, Schreck et al. (2014) compiled 1981–2010 climatological values of TC activity for each basin using statistics from both the WMO RSMCs and the Joint Typhoon Warning Center (JTWC). These values are referenced in each subsection.

Tallying the global TC numbers is challenging and involves more than simply adding up basin totals, because some storms cross TC basin boundaries, some TC basins overlap, and multiple agencies track and categorize TCs. Compiling the activity using preliminary IBTrACS data over all seven TC basins from NOAA's National Hurricane Center and the JTWC (Fig. 4.17), the 2019 season (2018/19 in the Southern Hemisphere [SH]) had 96 named storms (sustained wind speeds ≥ 34 kt or 17 m s^{-1}), which is one more than last season (Diamond and Schreck 2019) and above the 1981–2010 average of 82 (Schreck et al. 2014). The 2019 season also featured 53 hurricanes/typhoons/cyclones (HTC; sustained wind speeds ≥ 64 kt or 33 m s^{-1}), which is above the climatological average of 46 (Schreck et al. 2014). During the 2019 season, 31 storms reached major HTC status (sustained wind speeds ≥ 96 kt or 49 m s^{-1}), which is also above the long-term average of 21 and five more than the 2018 season (Diamond and Schreck 2019). All of these metrics were in the top 10% relative to 1981–2010 (Table 4.2).

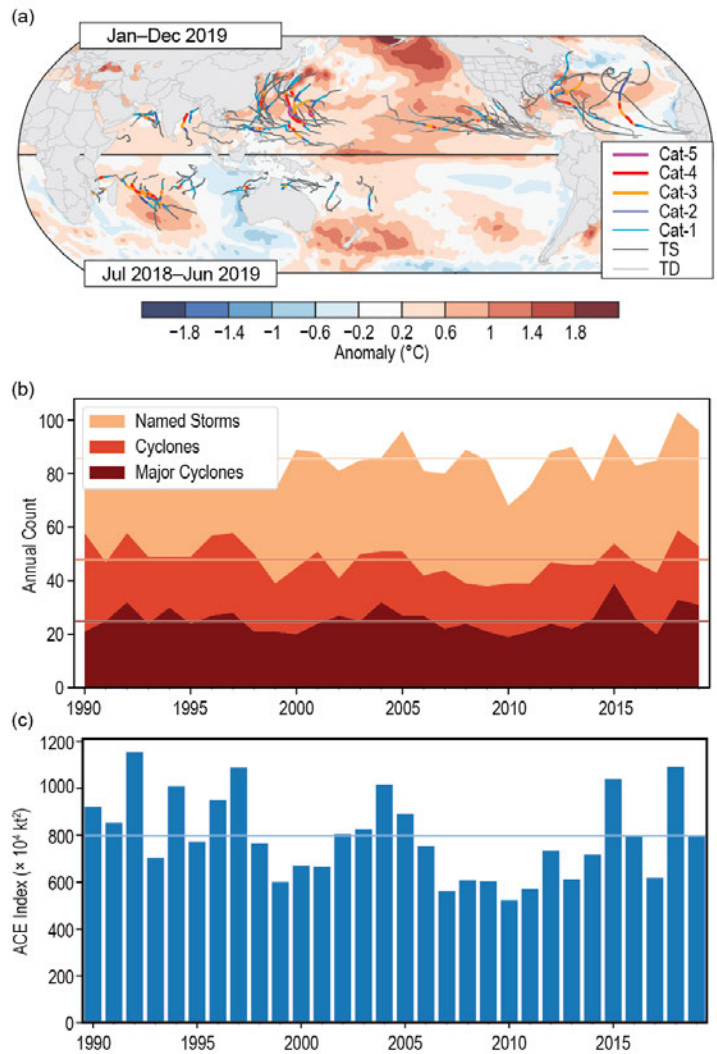

Fig. 4.17. (a) Global summary of TC tracks overlaid on associated OISST anomalies (°C; Reynolds et al. 2002) for the 2019 season relative to 1982–2010; (b) global TC counts; and (c) global ACE values. Horizontal lines on (b) and (c) are 1981–2010 normals.

Unauthenticated | Downloaded 12/18/20 02:55 PM UTC

In sections 4f2–4f8, 2018/19 and 2019 seasonal TC activity is described and compared to the historical record for each of the seven WMO-defined hurricane basins. For simplicity, all counts are broken down by the U.S. Saffir–Simpson Hurricane Wind Scale (SSHWS). The overall picture of global TCs during 2019 is shown in Fig. 4.17; actual counts by category are documented in Table 4.2.

Table 4.2. Global counts of TC activity by basin for 2019. "+" means top tercile; "++" is top 10%; "–" is bottom tercile; "––" is bottom 10% (all relative to 1981–2010). "+++" denotes record values for the entire IBTrACS period of record. Please note that some inconsistencies between Table 4.2 and the text of the various basin write-ups in section f exist and are unavoidable, as tallying global TC numbers is challenging and involves more than simply adding up basin totals, because some storms cross TC basin boundaries, some TC basins overlap, and multiple agencies are involved in tracking and categorizing TCs.

Basin	TCs	HTCs	Major HTCs	SS Cat 5	ACE ($\times 10^4$ kt^2)
North Atlantic	18 +	6	3 +	2 ++	130
Eastern North Pacific	19	7	4	0	97
Western North Pacific	27	16	10	3 +	263
North Indian	8 ++	6 +++	3 +++	0	85 +++
South Indian	11 +	10 ++	8 +++	0	154 ++
Australian Region	7 –	4	3 +	0	68
Southwest Pacific	6	4 +	0 –	0	25
Global Totals	**96 ++**	**53 +**	**31 ++**	**5 +**	**795**

Globally, five storms during the year reached SSHWS Category 5 strength (sustained wind speeds ≥ 137 kt or 70.5 m s^{-1}). This was one fewer than recorded in 2016 (Diamond and Schreck 2017), equal to the number recorded in 2017 (Diamond and Schreck 2018), and six fewer than the total of 11 recorded in 2018 (Diamond and Schreck 2019). The all-time record of 12 Category 5 global TCs was set in 1997 (Schreck et al. 2014).[1]

The five Category 5 storms were: Super Typhoons Wutip, Hagibis, and Halong in the western North Pacific and Hurricanes Dorian and Lorenzo in the North Atlantic. Dorian caused unprecedented and tremendous devastation, with approximately 70 fatalities reported in the northwest Bahamas and over $3.4 billion (U.S. dollars) in damages generated there. Dorian was responsible for six fatalities in Florida and three in North Carolina and caused over $1 billion (U.S. dollars) in damages in the United States. As a post-tropical cyclone, Dorian also caused considerable damages in Nova Scotia, Canada, with over $100 million (U.S. dollars) in damages reported. While Lorenzo was a Category 5 storm for a short period of time, it was more deadly as a post-tropical/extratropical cyclone. Lorenzo produced tropical storm force winds across portions of Ireland, and was the second deadliest storm of the 2019 North Atlantic season, causing 19 deaths both at sea and along the U.S. coast as a result of high-surf conditions. Sidebar 4.1 details the record-setting and devastating local impacts of Hurricane Dorian.

2) Atlantic basin—G. D. Bell, E. S. Blake, C. W. Landsea, M. Rosencrans, H. Wang, S. B. Goldenberg, and R. J. Pasch

(I) 2019 SEASONAL ACTIVITY

The 2019 Atlantic hurricane season produced 18 named storms, of which six became hurricanes and three achieved major hurricane status (Fig. 4.18a). The HURDAT2 1981–2010 seasonal averages (included in IBTrACS) are 11.8 named storms, 6.4 hurricanes, and 2.7 major hurricanes (Landsea and Franklin 2013). The 2019 seasonal Accumulated Cyclone Energy (ACE) value (Bell et al. 2000) was 134% of the 1981–2010 median (which is 92.4 × 10^4 kt^2; Fig. 4.18b), above NOAA's threshold

[1] SSHWS is based on 1-minute averaged winds, and the categories are defined at: https://www.weather.gov/mfl/saffirsimpson; the Australian category scale is based on 10-minute averaged winds, and those categories are defined at: https://australiasevereweather.com/cyclones/tropical_cyclone_intensity_scale.htm

Unauthenticated | Downloaded 12/18/20 02:55 PM UTC

(120%) for an above-normal season. The numbers of named storms and major hurricanes were also both above average. Therefore, the 2019 season was designated as above normal by NOAA. This makes 2019 the fourth consecutive above-normal season, tying the record set in 1998–2001. This also marks the 17th above-normal season of the 25 since the current Atlantic high-activity era began in 1995 (Goldenberg et al. 2001; Bell et al. 2019).

The previous high-activity era for which fairly reliable data on TC counts and overall hurricane strengths exist is 1950–70. That period also featured numerous above-normal seasons (10 out of 21), while the intervening low-activity era of 1971–94 had only 2 out of 24 (Bell et al. 2018). Note that the hurricane record is considered far less reliable before 1950, with exact season-to-season comparisons for ACE considered less reliable before the mid-1970s and the start of the geostationary satellite era (Landsea et al. 2006). Given these caveats, the best estimates suggest that the previous high-activity era actually spanned the period from 1926–70 (Goldenberg et al. 2001).

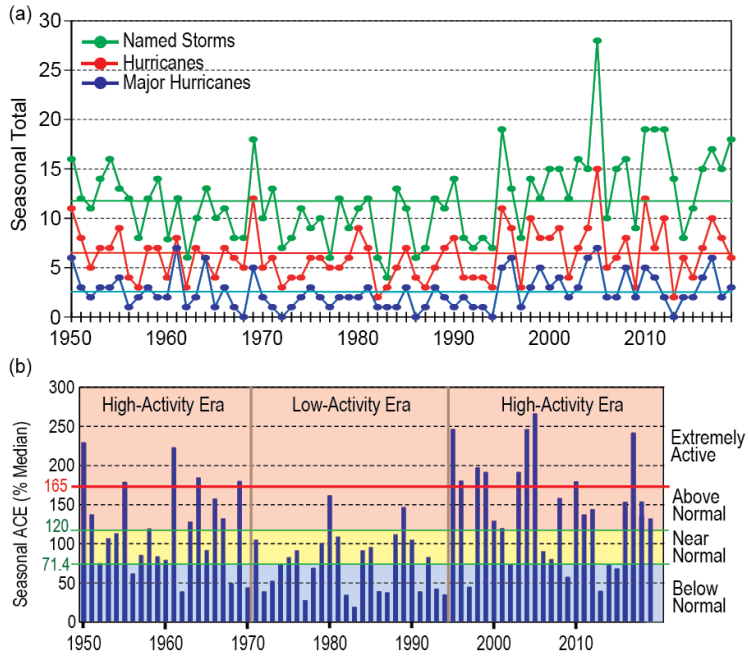

Fig. 4.18. Seasonal Atlantic hurricane activity during 1950–2019. (a) Numbers of named storms (green), hurricanes (red), and major hurricanes (blue); 1981–2010 seasonal means shown by solid colored lines. (b) ACE (Bell et al. 2000) index expressed as percent of the 1981–2010 median value. Red, yellow, and blue shadings correspond to NOAA classifications for above-, near-, and below-normal seasons, respectively (http://www.cpc.ncep.noaa.gov/products/outlooks/background_information.shtml). Thick red horizontal line at 165% ACE value denotes the threshold for an extremely active season. Vertical brown lines separate high- and low-activity eras. Note: There is a low bias in activity during the 1950s to the early 1970s due to the lack of satellite imagery and technique (Dvorak) to interpret TC intensity for systems over the open ocean. (Source: HURDAT2 [Landsea and Franklin 2013] for TC counts.)

The 18 named storms during 2019 are the sixth highest on record since 1950, while the 2019 ACE value is only the 24th highest in that 69-year record. This disparity is in part because two storms (Category 5 Hurricanes Dorian and Lorenzo) produced about 60% of the season's ACE. Meanwhile, eight of the named storms were very short-lived (<2 days). There has been a large artificial increase in these "shorties" since 2000, with seasons averaging about five per year since that time (Landsea et al. 2010). The increased ability to record these storms primarily reflects new observational capabilities such as scatterometers, Advanced Microwave Sounding Units, and the Advanced Dvorak Technique. Villarini et al. (2011) confirmed the lack of association of the shorties' time series with any known climate variability.

(II) STORM FORMATION REGIONS AND LANDFALLS

The vast majority of Atlantic TCs typically form during the peak months (August–October, ASO) of the hurricane season. During 2019, 15 of the 18 named storms, five of the six hurricanes, and all three major hurricanes formed during ASO.

Historically, the primary cause for an above-normal season is a sharp increase in activity associated with storms that form within the Main Development Region (MDR), which spans the tropical Atlantic Ocean and Caribbean Sea between 9.5°N and 21.5°N (Goldenberg and Shapiro 1996; Goldenberg et al. 2001; Bell and Chelliah 2006; Bell et al. 2017, 2018, 2019). For above-normal seasons during 1981–2010, the ACE value associated with storms first named in the MDR averaged 155% of the median (Fig. 4.19a), compared to only 15.8% during below-normal seasons. During 2019, the MDR-related ACE value was 101% of the median.

Unauthenticated | Downloaded 12/18/20 02:55 PM UTC

The nearly tenfold increase in ACE that occurs on average during above-normal seasons reflects the fact that far more MDR-initiated storms eventually become hurricanes (6.4 compared to 1.0) and major hurricanes (4.4 compared to 0.4). These differences not only reflect a nearly four-fold increase in the number of named storms that form within the MDR during above-normal seasons (9.3 compared to 2.5), but also a significantly higher percentage of those storms that become hurricanes (72% compared to 39%) and major hurricanes (44% compared to 17%; Fig. 4.19b). These results are consistent with those of Goldenberg et al. (2001), who noted a five-fold increase in the number of Caribbean hurricanes for high- versus low-activity eras. During 2019, six named storms formed within the MDR, with three (50%) eventually becoming hurricanes and two (33%) eventually becoming major hurricanes. Thus, the MDR-related activity during 2019 was relatively modest for an above-normal season in the entire basin, and no Caribbean hurricanes were recorded.

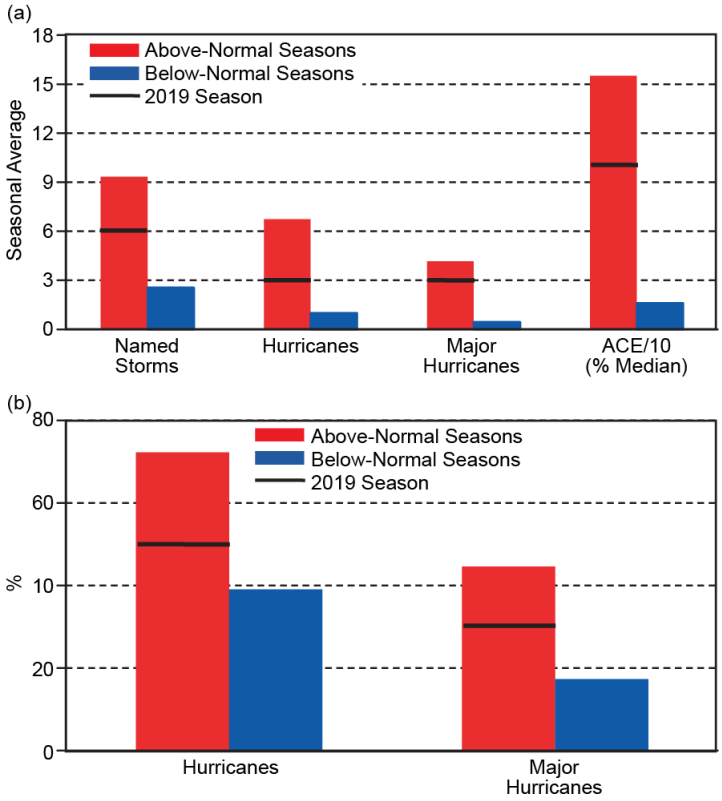

Fig. 4.19. (a) Seasonal averages of specified storm metrics during 1981–2010 associated with named storms initiated within the MDR. (b) Percentage of MDR-initiated named storms during 1981–2010 that eventually became hurricanes (left) and major hurricanes (right). Red (blue) bars show results for above-normal (below-normal) seasons. (Source: HURDAT2 [Landsea and Franklin 2013].)

Two-thirds (67%) of the named storms during 2019 formed outside of the MDR, which is a far higher percentage than the 1981–2010 average of 42% for above-normal seasons. Five of those storms during 2019 formed over the Gulf of Mexico, tying a record with 2003 and 1957 for the most storms to form in that region. The other seven named storms (including one hurricane) during 2019 formed over the North Atlantic north of the MDR, with all but one tropical storm forming over the western North Atlantic (west of 55°W and north of 21.5°N). A relatively high level of TC formation (six named storms including two hurricanes) also occurred over the western North Atlantic in 2018 (Bell et al. 2019).

Regarding landfalls, the most significant landfalling storm of the 2019 Atlantic hurricane season was Major Hurricane Dorian, which stalled over Abaco Island and Grand Bahama Island in the northwest Bahamas during 1–2 September. Dorian spent much of this period at Category 5 intensity, resulting in widespread destruction and death. Dorian tied the Labor Day 1935 hurricane for the strongest on record to make landfall (based on maximum wind speed) anywhere in the Atlantic basin. While the intensity of Dorian was continually observed via satellite and extensively measured by numerous NOAA and Air Force Reserve aircraft reconnaissance flights, the intensity of the 1935 Labor Day storm was only approximated based on a reading from a single land-based barometer, and the estimated maximum surface wind speed was derived using pressure-wind relationships from that one observation.

By 6 September, Dorian weakened to a Category 1 hurricane and made landfall in North Carolina. Two other storms also made landfall in the United States during 2019. These storms were Barry, which made landfall as a Category 1 hurricane in Louisiana on 13 July, and Tropical Storm Imelda, which made landfall in Texas on 17 September.

Unauthenticated | Downloaded 12/18/20 02:55 PM UTC

(III) SEA SURFACE TEMPERATURES

The MDR sea surface temperatures (SSTs) were above average with an area-averaged SST anomaly of +0.40°C (Fig. 4.20b). Most locations had departures between +0.25°C and +0.50°C. However, this anomaly was only slightly higher (by 0.1°C) than the remainder of the global tropics (Fig. 4.20c).

On multi-decadal time scales, the presence of higher SST anomalies in the MDR compared to the global tropics typifies the warm phase of the Atlantic Multidecadal Oscillation (AMO; Enfield and Mestas-Nuñez 1999; Bell and Chelliah 2006) and is characteristic of Atlantic high-activity eras such as 1950–70 and 1995–present (Goldenberg et al. 2001; Vecchi and Soden 2007; Bell et al. 2018). On interannual time scales, large fluctuations in the relative anomalous warmth of the MDR can also be seen. This variability can have nothing to do with the AMO itself and instead reflect factors such as fluctuations in the wind patterns across the MDR, El Niño–Southern Oscillation (ENSO), the Pacific-Decadal Oscillation, and Indian Ocean SST variability. During ASO 2019, area-averaged SSTs in both the tropical Indian and tropical Pacific Oceans were the second highest (anomalies were +0.73°C and +0.50°C, respectively) in the 1950–2019 record. The reduction in the relative anomalous MDR warmth, especially when compared to most years since 1995, reflected these conditions and should not be interpreted as an indicator that the warm AMO phase has ended.

Another important SST signal during ASO reflected above-average SSTs in the western North Atlantic (red box, Fig. 4.20a), where six TCs formed. The area-averaged SST anomaly in this region (+0.60°C) indicates a continuation of exceptional warmth in that area that began in 2014 (Fig. 4.20d).

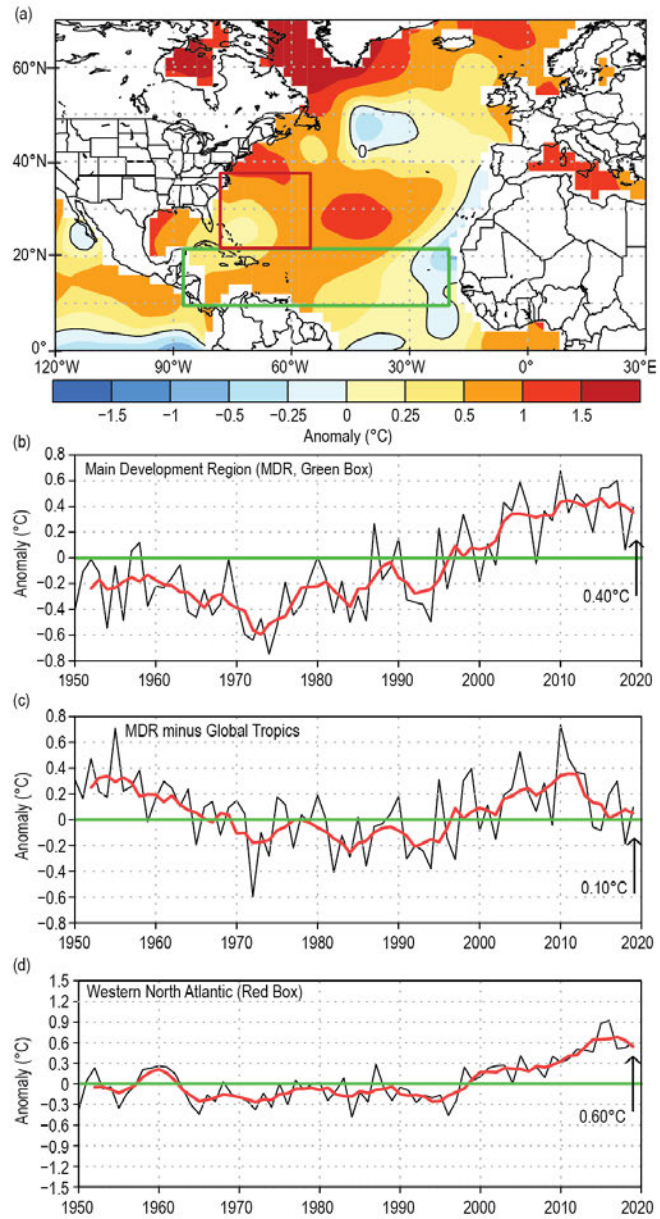

Fig. 4.20. (a) Aug–Oct (ASO) 2019 SST anomalies (°C). (b)–(d) Time series of ASO area-averaged SST anomalies (black) and 5-point running mean of the time series (red): (b) in the MDR (green box in (a), spanning 20°–87.5°W and 9.5°–21.5°N), (c) difference between the MDR and the global Tropics (20°N–20°S), and (d) in the western North Atlantic (red box in (a), spanning 55°–77.5°W and 21.5°–37.5°N). Anomalies are departures from the 1981–2010 period means. (Source: ERSST-v5 [Huang et al. 2017].)

(IV) ATMOSPHERIC CONDITIONS

Consistent with the ongoing high-activity era for Atlantic hurricanes, an interrelated set of conditions during ASO 2019 favored increased TC activity in the MDR even if that region was relatively quiet in 2019. These included upper tropospheric anticyclonic streamfunction anomalies across the subtropical North Atlantic, in association with an enhanced subtropical ridge (Fig. 4.21a). A similar anomaly pattern was present across the subtropical South Atlantic Ocean. This pronounced inter-hemispheric symmetry of the anticyclonic anomalies is typical of an enhanced West African monsoon system (Bell and Chelliah 2006), which is the June–September portion of the North African monsoon.

During 2019, these conditions were associated with upper-level easterly wind anomalies across the MDR and lower-level westerly wind anomalies over the eastern half of the MDR (Fig. 4.21b). This

Unauthenticated | Downloaded 12/18/20 02:55 PM UTC

overall pattern resulted in anomalously weak vertical wind shear across the MDR (Figs. 4.22a,b). The area-averaged magnitude of the vertical wind shear within the MDR was 7.0 m s^{-1} (Fig. 4.22c), which is below the 8 m s^{-1} threshold considered conducive to hurricane formation on a monthly time scale (Bell et al. 2017).

Over the eastern half of the MDR, the lower-level westerly wind anomalies reflected weaker easterly trade winds (Fig. 4.21b). These anomalies extended upward to at least the 700-hPa level (Fig. 4.21c), the approximate level of the African Easterly Jet (AEJ). This contributed to a deep layer of anomalous cyclonic relative vorticity (i.e., increased horizontal cyclonic shear) along the equatorward flank of the AEJ. These conditions are known to favor increased TC activity within the MDR by helping African easterly waves to be better maintained and by providing an inherent cyclonic rotation to their embedded convective cells (Bell et al. 2004, 2006, 2017, 2018).

All of the above conditions are typical of an enhanced West African monsoon system (Gray 1990; Hastenrath 1990; Landsea et al. 1992; Bell and Chelliah 2006; Bell et al. 2018). The strength of that monsoon is a major factor contributing to observed multidecadal fluctuations in Atlantic hurricane activity because it directly impacts atmospheric conditions and TC formation and intensification within the MDR. During August–September, one indicator of the enhanced monsoon was an extensive area of anomalous 200-hPa divergence across western Africa, with an associated core of negative velocity potential anomalies (Fig. 4.23a). Another indicator was enhanced convection (shown by negative Outgoing Longwave Radiation [OLR] anomalies) in the African Sahel region (red box, Fig. 4.23b). During August–September, OLR values in this region averaged 237 W m^{-2} (Fig. 4.23c). Values below 240 W m^{-2} indicate deep tropical convection. These values are typical of the current high-activity era, whereas OLR values generally above 240 W m^{-2} (indicating a weaker monsoon) were typical of the low-activity period of the 1980s and early 1990s. These multidecadal fluctuations in monsoon strength coincide with opposing phases (warm and cold, respectively) of the AMO.

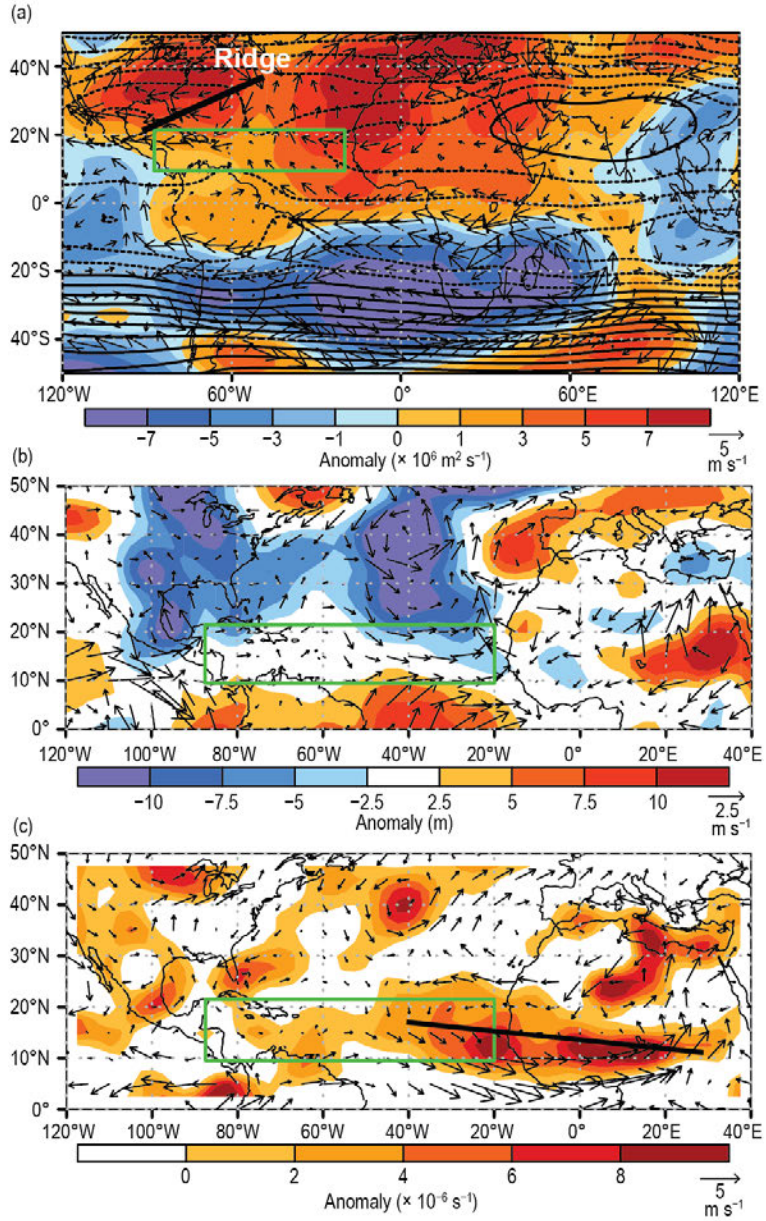

Fig. 4.21. Aug–Oct 2019: (a) 200-hPa streamfunction (contours, interval is 5 × 10^6 m^2 s^{-1}) and anomalies (shaded), and anomalous vector winds (m s^{-1}); (b) anomalous 1000-hPa heights (shaded, m) and vector winds; and (c) anomalous 700-hPa cyclonic relative vorticity (shaded, × 10^{-6} s^{-1}) and vector winds. In (a), the upper-level ridge discussed in the text is labeled and denoted by the thick black line. In (c), the thick solid line indicates the axis of the mean African Easterly Jet, hand-drawn based on total seasonal wind speeds (not shown). Vector scales differ for each panel, and are below right of the color bar. The green box denotes the MDR. Anomalies are departures from the 1981–2010 means. (Source: NCEP–NCAR reanalysis [Kalnay et al. 1996].)

Unauthenticated | Downloaded 12/18/20 02:55 PM UTC

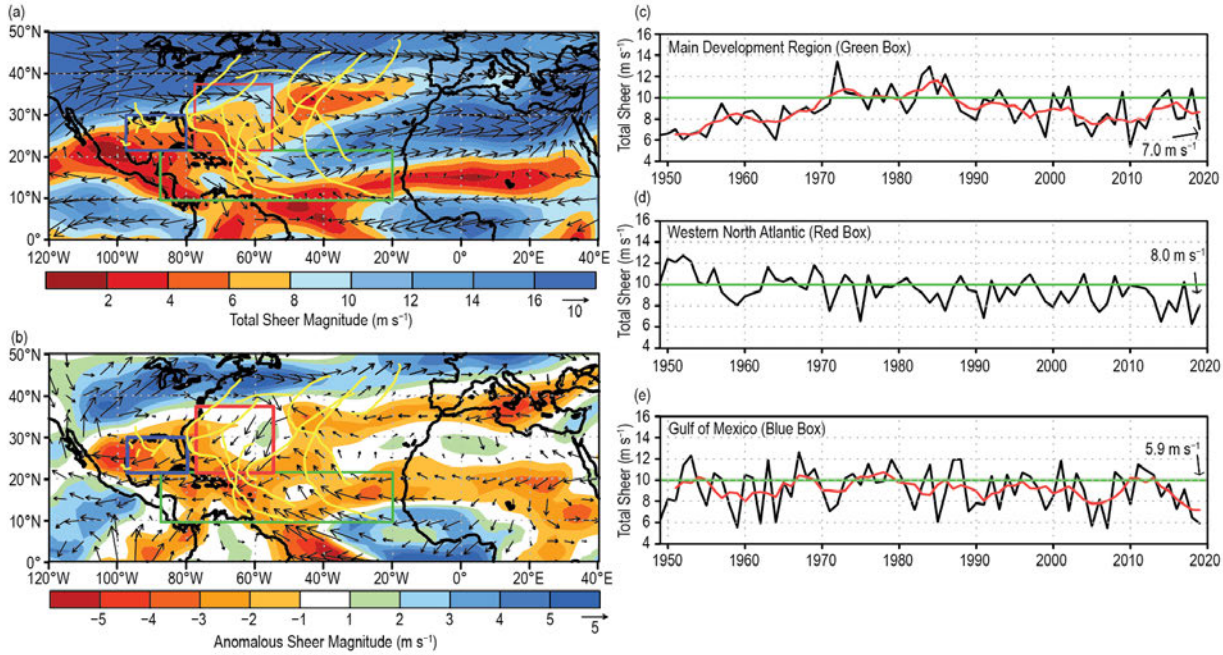

Fig. 4.22. Aug–Oct (ASO) magnitude of the 200–850-hPa vertical wind shear (m s^{-1}): (a) 2019 total magnitude and vector and (b) 2019 anomalous magnitude and vector versus 1981–2010 means. (c)–(e) Time series of ASO vertical shear magnitude (black) and 5-point running mean of the time series (red) averaged over (c) the MDR (green box in (a), (b) spanning 87.5°–20°W and 9.5°–21.5°N); (d) the western North Atlantic (red box in (a), (b) spanning 77.5°–55°W and 21.5°–37.5°N); and (e) the Gulf of Mexico (blue box in (a), (b) spanning 97.5°–80°W and 21.5°–30°N). In (a) and (b), 2019 TC tracks (yellow lines) are shown and vector scale (m s^{-1}) is below right of color bar. (Source: NCEP–NCAR reanalysis [Kalnay et al. 1996].)

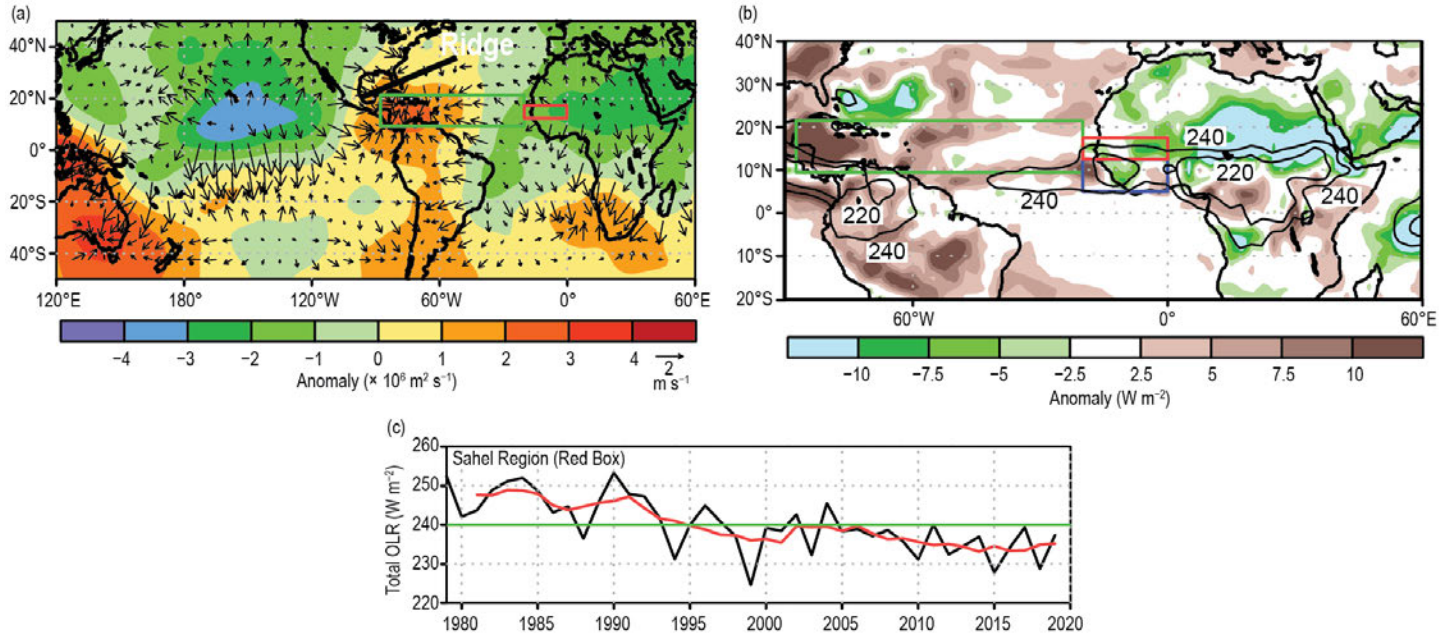

Fig. 4.23. (a) Aug–Sep 2019 anomalous 200-hPa velocity potential (× 10^6 m^{2}s^{-1}) and divergent wind vectors (m s^{-1}). (b) Aug–Sep 2019 anomalous OLR (W m^{-2}), with negative (positive) values indicating enhanced (suppressed) convection. (c) Time series of Aug–Sep total OLR (black) and 5-point running mean of the time series (red) averaged over the African Sahel region (red box in (a) and (b) spanning 20°W–0° and 12.5°–17.5°N). In (a) the upper-level ridge discussed in the text is labeled and denoted by the thick black line. In (b), contours show total OLR values of 220 W m^{-2} and 240 W m^{-2}. In (a) and (b), the green box denotes the MDR. Anomalies are departures from the 1981–2010 means. (Source: NCEP–NCAR reanalysis [Kalnay et al. 1996] for velocity potential and wind.)

Unauthenticated | Downloaded 12/18/20 02:55 PM UTC

SIDEBAR 4.1: **Hurricane Dorian: A devastating hurricane for the northwest Bahamas—** P. J. KLOTZBACH AND R. E. TRUCHELUT

The 2019 Atlantic hurricane season ended up slightly above normal for most tropical cyclone (TC) parameters, with a total of 18 named storms, six hurricanes, and three major hurricanes occurring. By far, the most significant and devastating hurricane of the 2019 season was Hurricane Dorian. Dorian will be most remembered for the devastation that it caused in the northwest Bahamas, especially on the Abaco Islands and on Grand Bahama Island. It was also the longest-lived (14 days as a named storm and 10 days as a hurricane) and most intense (1-minute maximum sustained winds of 160 kt (82 ms^{-1}) hurricane of the 2019 season (Avila et al. 2020). Dorian also generated the most Accumulated Cyclone Energy (ACE) of any Atlantic hurricane, accounting for ~40% of basinwide ACE accrued in 2019. This sidebar summarizes the meteorological history of Dorian along with the notable records that the hurricane achieved during its track across the Atlantic. Historical landfall records from 1851–present are taken from the National Hurricane Center/Atlantic Oceanographic and Meteorological Laboratory archive located at: http://www.aoml.noaa.gov/hrd/hurdat/All_U.S._Hurricanes.html, and Dorian's observed values are taken from Avila et al (2020).

Dorian became a tropical depression (TD) on 24 August in the central tropical Atlantic and was upgraded to a tropical storm (TS) shortly thereafter (Fig. SB4.1). Despite moving through an environment of relatively low wind shear and a warm sea surface (~28°–29°C), considerable mid-level dry air inhibited Dorian's intensification early in its lifetime. Dorian passed through the Windward Islands on 27 August as a TS. Dorian's center reformed farther north after interacting with Saint Lucia, and its center also reformed downshear (i.e., to the east) due to moderate westerly shear. This northeastward shift in track from where the models were originally forecasting the storm allowed it to avoid the elevated terrain of Hispaniola and Puerto Rico, which would have likely weakened the storm. It then turned northwestward and intensified as it moved into a more moisture-rich environment. Dorian became a hurricane as it tracked over Saint Croix on 28 August and reached major hurricane intensity on 30 August as it approached the Bahamas. From 0600 UTC on 30 August to 1800 UTC on 31 August, Dorian underwent rapid intensification from 90 kt (46 $m\,s^{-1}$) to 130 kt (67 $m\,s^{-1}$) with 24-hour intensification rates ranging between 30 kt (15 $m\,s^{-1}$) and 35 kt (18 $m\,s^{-1}$). Dorian slowed as it approached the northwest Bahamas, then underwent another burst of rapid intensification, becoming a Category 5 hurricane as it approached Great Abaco Island.

Soon thereafter, Dorian reached its maximum intensity of 160 kt (82 $m\,s^{-1}$) as it made landfall on Great Abaco Island on 1 September. In doing so, Dorian became the strongest hurricane on record to make landfall in the Bahamas and tied with the Labor Day Hurricane of 1935 for the strongest landfalling hurricane on record anywhere in the Atlantic basin. The 160 kt (82 $m\,s^{-1}$) intensity achieved by Dorian was also the strongest on record by any Atlantic hurricane outside of the tropics (>23.5°N) in the satellite era (since 1966). Dorian tracked slowly over Great Abaco as the steering currents collapsed, and the system effectively stalled after making landfall on Grand Bahama Island with maximum sustained winds of 155 kt (80 $m\,s^{-1}$) (Fig. SB4.2). Dorian was the first Category 5 hurricane on record to make landfall on Grand Bahama Island. Its extremely slow forward movement caused devastating wind, rain, and storm surge impacts over these islands. During its first 24 hours over Grand Bahama Island, Dorian

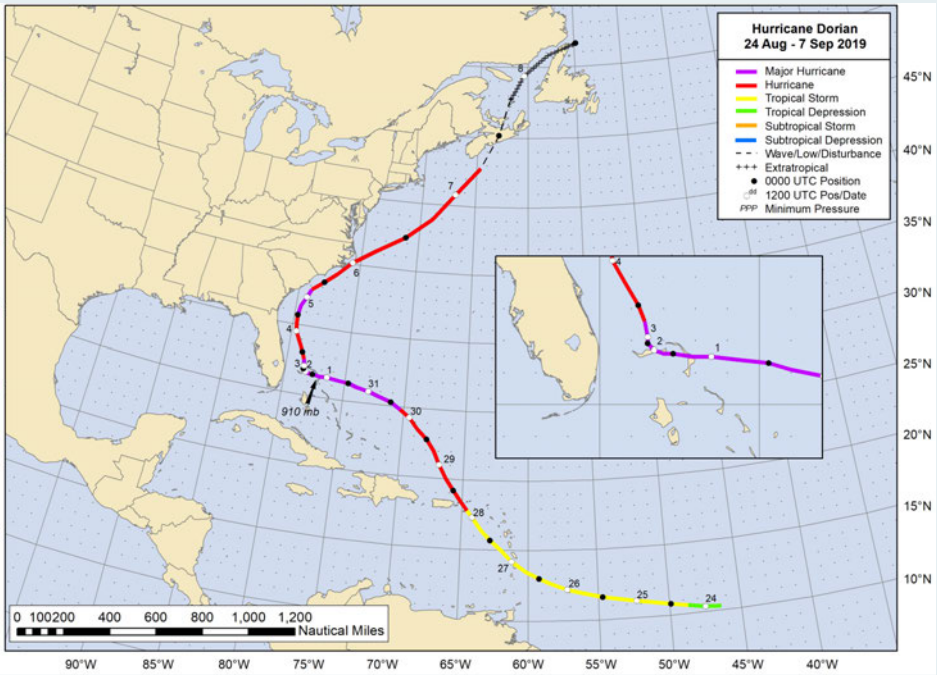

Fig. SB4.1. NOAA's National Hurricane Center Best Track Plot for Hurricane Dorian (Avila et al. 2020).

Unauthenticated | Downloaded 12/18/20 02:55 PM UTC

weakened extremely slowly—from a 155 kt (80 m s^{-1}) Category 5 hurricane to a 115 kt (59 m s^{-1}) Category 4 hurricane. Because of this stalling motion and maintenance of strong hurricane intensity, Dorian generated the most ACE in a 1° × 1° grid box in the Atlantic basin in the satellite era (i.e., since 1966; Wood et al. 2020).

Land interaction, an increase in vertical wind shear, and cold water upwelling continued to slowly reduce Dorian's wind strength, and it weakened below major hurricane strength late on 3 September. Dorian tracked northward offshore of the southeast United States and briefly regained major hurricane strength on 5 September before weakening as it encountered lower sea surface temperatures (SSTs) and stronger vertical wind shear. It brushed the South Carolina and North Carolina coasts, and Dorian made landfall on Cape Hatteras at 1230 UTC on 6 September as a Category 2 hurricane, with winds estimated at 85 kt (44 m s^{-1}), although most of the strongest winds remained over water to the east of the center (Avila et al. 2020). At the time of its North Carolina landfall, Dorian's central pressure was 956 hPa, tying it with Floyd (1999) and Florence (2018) for the sixth lowest central pressure for a landfalling North Carolina hurricane since 1950. Dorian became extratropical as it accelerated northeastward, but it also strengthened slightly during this time. It made a final landfall as a post-tropical cyclone in Nova Scotia on 7 September, bringing hurricane-force winds to portions of Atlantic Canada. Dorian made a final landfall as a post-tropical storm in Newfoundland on 8 September.

Dorian was an extremely long-lived storm and set several records due to both its intensity and longevity. Its 160 kt (82 m s^{-1}) winds were tied with Gilbert (1988) and Wilma (2005) for the second strongest on record for an Atlantic hurricane in the satellite era (since 1966), trailing only the 165 kt (85 m s^{-1}) winds recorded by Allen (1980). Its lifetime minimum central pressure of 910 hPa was tied with Ivan for the ninth-lowest lifetime minimum central pressure since 1980. Dorian generated 49 × 10^4 kt^2 ACE during its lifetime—the fifth most for an August TC in the satellite era. It also generated 14 named storm days, tying it with Felix (1995) for third place for most named storm days by a storm forming in August in the satellite era.

Given its extreme intensity and slow forward speed over both Great Abaco Island and Grand Bahama Island, Dorian caused tremendous devastation, with over 70 fatalities reported by the Bahamian Health Minister and $3.4 billion (U.S. dollars) in damage generated (Avila et al. 2020). Dorian was responsible for four indirect fatalities in the United States and caused $1.6 billion (U.S. dollars) in damage. Dorian as a post-tropical cyclone also caused considerable damage in Nova Scotia, with over $100 million (U.S. dollars) in damage being reported.

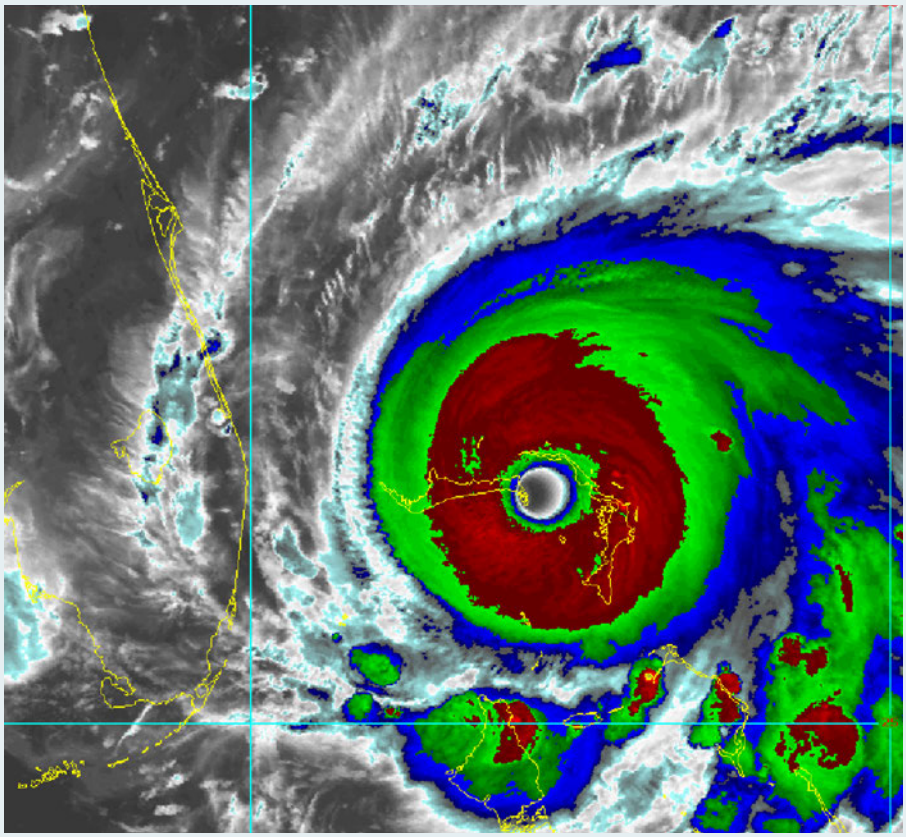

Fig. SB4.2. NOAA-18 infrared satellite image of Hurricane Dorian making landfall on Grand Bahama Island at 154 UTC on 2 Sep 2019.

Despite the above conditions, the 2019 TC activity for the MDR as a whole was relatively modest. This signal partly reflected the limited activity (two tropical storms) over the Caribbean Sea due in part to anomalously strong upper-level convergence (Fig. 4.23a) and sinking motion there. The modest activity was also associated with the synoptic scale sinking motion typically found downstream of the mean ridge axis, which in this case extended across the Gulf of Mexico and western subtropical North Atlantic (indicated by thick black line in Figs. 4.21a, 4.23a).

Two other aspects of the interannual variability during ASO 2019 include the relatively high number of six TC formations over the western subtropical North Atlantic and five over the Gulf of Mexico (yellow lines, Fig. 4.22). These

Unauthenticated | Downloaded 12/18/20 02:55 PM UTC

are roughly double the 1981–2010 averages seen during above-normal seasons. In addition to anomalously warm SSTs during ASO (Fig. 4.20a), both regions experienced below-average vertical wind shear (Fig. 4.22b) with area-averaged shear values at or below 8 m s^{-1} (Figs. 4.22d,e). For the Gulf of Mexico, the area-averaged shear was less than 6 m s^{-1} (Fig. 4.22e), which is comparable to some of the lowest values in the record. These conditions were linked to the persistent, anomalous upper-level ridge that extended across both regions (Fig. 4.21a).

3) Eastern North Pacific and Central North Pacific basins—K. M. Wood and C. J. Schreck

(I) SEASONAL ACTIVITY

Two agencies are responsible for issuing advisories and warnings in the eastern North Pacific (ENP) basin: NOAA's National Hurricane Center in Miami, Florida, covers the region from the Pacific coast of North America to 140°W, and NOAA's Central Pacific Hurricane Center in Honolulu, Hawaii, covers the central North Pacific (CNP) region between 140°W and the date line. This section combines statistics from both regions.

A total of 19 named storms formed in the combined ENP/CNP basin, seven of which became hurricanes and four became major hurricanes. The 1981–2010 IBTrACS seasonal averages for the basin are 16.5 named storms, 8.5 hurricanes, and 4.0 major hurricanes (Schreck et al. 2014). Thus, 2019 storm counts were near normal (Fig. 4.24a). These storms occurred between the official start date of the ENP season of 15 May and end date of 30 November. Hurricane Alvin first reached tropical storm strength on 29 June—the latest first storm formation since 2016's Tropical Storm Agatha was named on 2 July. The final named storm, Raymond, dissipated on 17 November. Four

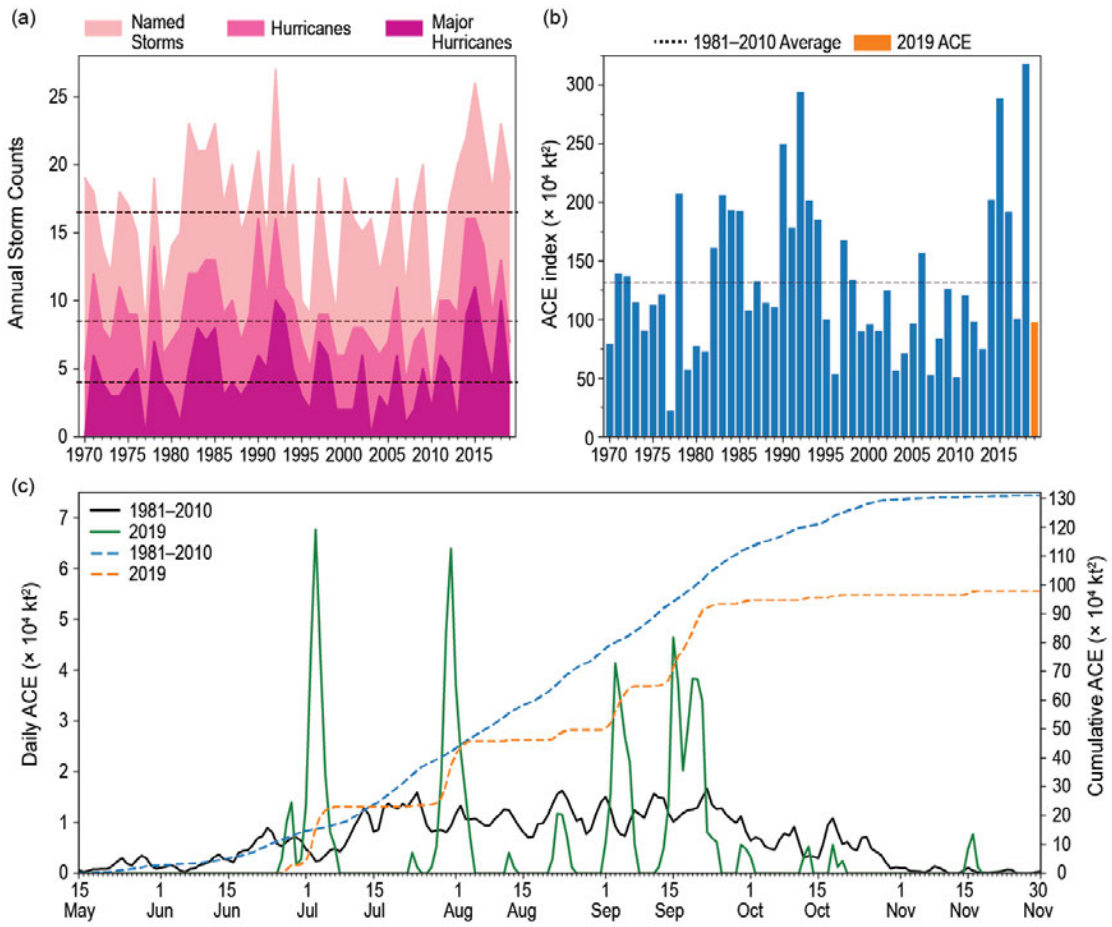

Fig. 4.24. (a) Annual storm counts for the eastern North Pacific by category during 1970–2019, with 1981–2010 average denoted as dashed lines. (b) Annual ACE during 1970–2019, with 2019 in orange and the 1981–2010 average denoted by the dashed line. (c) Daily ACE during 1981–2010 (solid black) and 2019 (solid green); accumulated daily ACE during 1981–2010 (dashed blue) and 2019 (dashed orange).

Unauthenticated | Downloaded 12/18/20 02:55 PM UTC

of the 19 storms either formed within or entered the CNP basin from the east, placing 2019 slightly below the 1981–2010 IBTrACS seasonal average of 4.7 named storms for the CNP.

Unlike 2018, which set a new record for basin-wide ACE (318×10^4 kt^2; Wood et al. 2019), the 2019 seasonal ACE index was 98×10^4 kt^2, or 74% of the 1981–2010 mean of 132×10^4 kt^2 (Fig. 4.24b; Bell et al. 2000; Schreck et al. 2014). The bulk of TC activity was confined to late June through late September (Fig. 4.24c); no hurricanes developed in October or November.

Three TCs contributed more than half of 2019's total ACE and reached Category 4 intensity on the SSHWS. Each underwent rapid intensification (≥ 30 kt or 15.4 m s^{-1} in 24 hours) prior to reaching peak intensity and then rapidly weakened (≤ –30 kt or –15.4 m s^{-1} in 24 hours; Wood and Ritchie 2015). The strongest storm of the season, Hurricane Barbara (30 June–6 July) peaked at 135 kt (69 m s^{-1}), just shy of Category 5 strength. Hurricane Erick (27 July–3 August) intensified by 50 kt (26 m s^{-1}) in 24 hours, and Hurricane Kiko (12–24 September) reached Category 4 intensity (115 kt; 59 m s^{-1}) after similarly explosive intensification from 60 kt to 115 kt in 24 hours. All three TCs maintained peak intensity for only 12 hours before weakening rapidly.

(II) ENVIRONMENTAL INFLUENCES ON THE 2019 SEASON

The El Niño of 2018/19 transitioned to a neutral state in mid-2019, and seasonal SSTs were about average near most TC formation locations (Fig. 4.25a). Anomalous warmth dominated the western part of the basin, particularly north of 10°N, but few storms crossed this region. Below-average OLR was largely colocated with TC tracks (Fig. 4.25b), and vertical wind shear was slightly weaker than normal where most TCs formed (Fig. 4.25c). As in 2018, the strongest easterly wind shear anomalies occurred in the central Pacific, but few 2019 TCs reached that region. Again, enhanced low-level westerlies dominated west of 140°W, and the enhanced 850-hPa easterly flow west of Central America (Fig. 4.25d) resembles the pattern in 2018 that was attributed to anomalously strong gap winds influenced by the Sierra Madre mountain range (Kruk and Schreck 2019).

Both the Madden Julian Oscillation (MJO) and convectively-coupled Kelvin waves are known to affect ENP TC activity, particularly cyclogenesis (e.g., Maloney and Hartmann 2001; Aiyyer and Molinari 2008; Schreck and Molinari 2011; Ventrice et al. 2012a,b; Schreck 2015, 2016). To examine convective variability during the 2019 ENP hurricane season, Fig. 4.26 shows unfiltered, MJO-filtered, and Kelvin wave-filtered OLR anomalies computed using the methodology of Kiladis et al. (2005, 2009). In general, the MJO remained weak in the ENP for much of the hurricane season. However, a strong convectively suppressed MJO phase in June likely contributed to the late start to the season. The subsequent weaker convective envelope

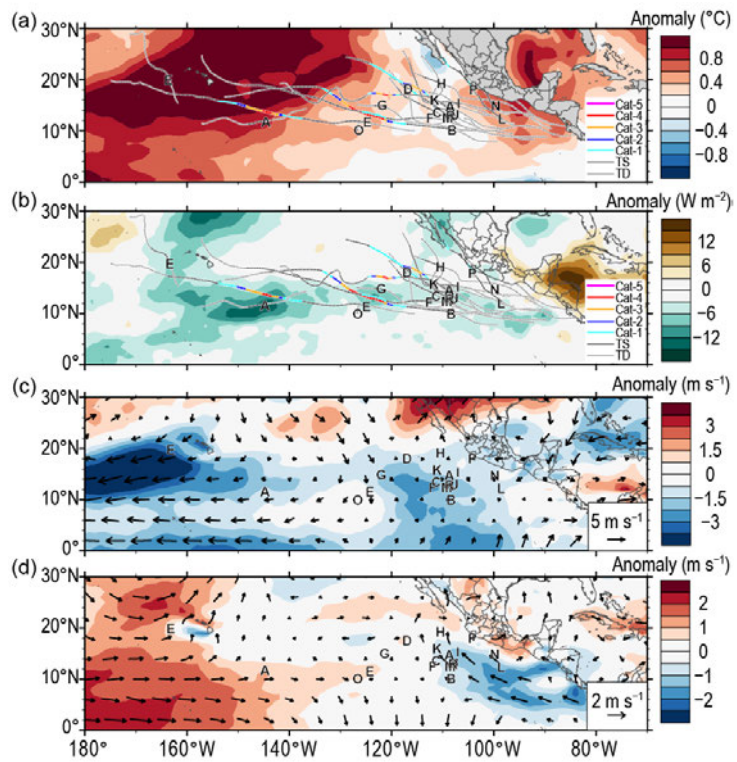

Fig. 4.25. 15 May–30 Nov 2019 anomaly maps of (a) SST (°C; Banzon and Reynolds 2013); (b) OLR (W m^{-2}; Schreck et al. 2018); (c) 200–850-hPa vertical wind shear (m s^{-1}) vector (arrows) and scalar (shading) anomalies; and (d) 850-hPa wind (m s^{-1}; arrows) and zonal wind (shading) anomalies. Anomalies are relative to the annual cycle from 1981–2010, except for SST, which is relative to 1982–2010. Letters denote where each ENP TC attained tropical storm intensity. Wind data are obtained from CFSR (Saha et al. 2014). The more westward A represents "Akoni" and the more westward E "Ema."

Unauthenticated | Downloaded 12/18/20 02:55 PM UTC

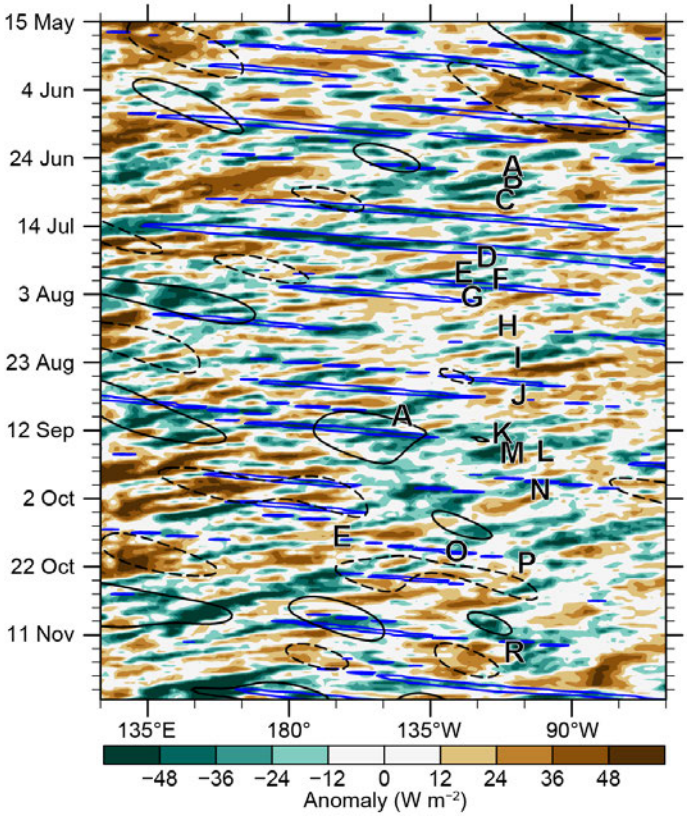

Fig. 4.26. Longitude–time Hovmöller diagram of 5°–15°N average OLR (W m^{-2}; Schreck et al. 2018). Unfiltered anomalies from a daily climatology are shaded. Negative anomalies (green) indicate enhanced convection. Anomalies filtered for Kelvin waves are contoured in blue at –10 W m^{-2} and MJO-filtered anomalies in black at ±10 W m^{-2}. Letters denote the longitude and time when each ENP TC attained tropical storm intensity. The second A represents "Akoni" and the second E "Ema."

may have contributed to the formations of Alvin, Barbara, and Cosme. Multiple Kelvin waves crossed the ENP, potentially influencing the development of Dalila, Gil, Juliette, Narda, Octave, Priscilla, and Raymond. Beyond these influences, easterly waves—shown in Fig. 4.26 as westward-moving negative anomalies—likely supported the genesis of multiple storms including Ivo, Priscilla, and Raymond.

(III) TROPICAL CYCLONE IMPACTS

Three TCs directly impacted land in 2019. Hurricane Lorena (17–22 September) made two landfalls in Mexico as a Category 1 hurricane, once in Jalisco and once in Baja California Sur, with one reported death (Avila 2019). In addition, Lorena's remnant moisture reached the southwestern United States where it likely contributed to thunderstorms and heavy rain. Tropical Storm Narda (29 September–1 October) also made landfall twice in Mexico, both times as a tropical storm, causing six fatalities largely attributed to freshwater flooding (Blake 2019). Short-lived Tropical Storm Priscilla (20 October) made landfall hours after being named and dumped more than 150 mm of rain in Nayarit. Its remnant moisture may have contributed to severe weather in the south-central United States (Stewart 2019). Though none produced significant damage, three landfalling storms in Mexico is well above the long-term average of 1.8 each year (Raga et al. 2013). Beyond landfalls, remnants of Tropical Storm Raymond (15–17 November) may have influenced the development of a low-pressure system that subsequently produced wind, rain, and flooding in the southwestern United States (NOAA 2019).

4) Western North Pacific basin—S. J. Camargo

(I) OVERVIEW

The 2019 TC season in the western North Pacific (WNP) was slightly above normal by most measures of TC activity. The data used here are primarily from JTWC best-track data for 1945–2018 and preliminary operational data for 2019. All statistics are based on the 1981–2010 climatological period with the exception that landfall statistics use 1951–2010.

Unauthenticated | Downloaded 12/18/20 02:55 PM UTC

A total of 28 TCs (climatological median = 26) reached tropical storm (TS) intensity in the WNP during 2019, including Pabuk, which formed in December 2018. Of these, 17 reached typhoon intensity (median = 16), with 4 reaching super typhoon status (≥ 130 kt, median = 3.5). There were also three tropical depressions (TDs; median 3.5). While 61% of the tropical storms became typhoons (median 64%), 23% of the typhoons intensified to super typhoons (median 24%). In Fig. 4.27a, the number of storms in each category is shown for the period 1945–2019.

The Japan Meteorological Agency (JMA) total for 2019 was 29 storms (top tercile ≥ 29), also including 2018 Tropical Storm Pabuk. While the JMA and JTWC totals are very close, there were some differences between the two agencies.[2] Kajiki was considered a TS by JMA but a depression by JTWC. Matmo was considered a severe TS by JMA and a typhoon by JTWC. Tapah was classified as a TS for JTWC and a typhoon for JMA. Tropical Storm Sepat was not included as a TC by JTWC, and Tropical Storm Four was not classified as a TC by JMA. Of the 29 TCs recorded by JMA, nine were tropical storms (top quartile ≥ 7); three were severe tropical storms (bottom quartile ≤ 4); and 17 were typhoons (top quartile ≥ 17). Fifty-nine percent of the storms reached typhoon intensity (median 58%). The number of all TCs (1951–76) and TSs, severe TSs, and typhoons (1977–2019) according to the JMA are shown in Fig. 4.27b. The Philippine Atmospheric, Geophysical and Astronomical Services Administration (PAGASA) named all 20 TCs that entered its area of responsibility, including Tropical Depressions Amang, Chedeng, Goring, and Marilyn, which were not named by JMA.

(II) SEASONAL ACTIVITY

The season started with Tropical Storm Pabuk, which formed on 30 December 2018 and lasted until 7 January 2019, reaching TS status on 1 January. Super Typhoon Wutip was the season's next named storm and the second TC to reach super typhoon intensity in February in the historical record, following Super Typhoon Higos (2005). Typhoon Mitag (2002) also formed in February, but reached super typhoon intensity in March. No named storms formed during March–May (bottom quartile = 0 for each month). Only Tropical Storm Four was active in the month of June according to the JTWC (bottom quartile ≤ 1), while JMA named Tropical Storm Sepat that month. Three TSs were active during July: Mun, Danas, and Nari (bottom quartile ≤ 2). Tropical Storm Wipha formed at the end of July, but was mostly active in August and therefore was considered as an August storm. Besides Wipha, five other TCs occurred in August: Tropical Storms Bailu and Podul, Typhoons Francisco and Krosa, and Super Typhoon Lekima. August had a total of six named storms (top quartile ≥ 6), three typhoons (median = 3), and one super typhoon (top quartile ≥ 1). Five more named storms formed in September (median = 5): Tropical Storms Peipah and Tapah and typhoons Faxai, Lingling, and Mitag (median = 3). October was an active month with four typhoons: Hagibis, Neoguri, Bualoi, and Matmo (top quartile ≥ 4), with Hagibis reaching super typhoon intensity. The basin continued to be very active in November with six named storms (top quartile ≥ 3): Tropical Storm Fung-Wong and Typhoons Halong (super typhoon), Nakri, Fengshen, Kalmaegi, and Kammuri (top quartile ≥ 2). The six named storms and five typhoons matched the historical record for November, set in 1964 and 1968, respectively. The season ended with Typhoon Phanphone in December (median = 1).

As shown in Figs. 4.27c–f, the early season (January–June) was relatively quiet, with only three tropical storms (bottom quartile ≤ 2.5) and one typhoon (bottom quartile ≤ 1) which reached super typhoon intensity. The peak season (July–October) had near-normal activity with 18 named storms (median = 17), 10 typhoons (bottom quartile ≤ 9), and two super typhoons (median = 2). In contrast, the late season (November–December) was quite active, with seven named storms (top quartile ≥ 4.5, maximum = 7) and six typhoons (top quartile ≥ 3) including one super typhoon (top quartile = 1). The occurrence of six typhoons during November and December is a historical record. This

[2] It is well known that there are systematic differences between the JMA and the JTWC datasets, which have been extensively documented in the literature (e.g. Wu et al. 2006; Nakazawa and Hoshino 2009; Song et al. 2010; Ying et al. 2011; Yu et al. 2012; Knapp et al. 2013; Schreck et al. 2014).

Unauthenticated | Downloaded 12/18/20 02:55 PM UTC

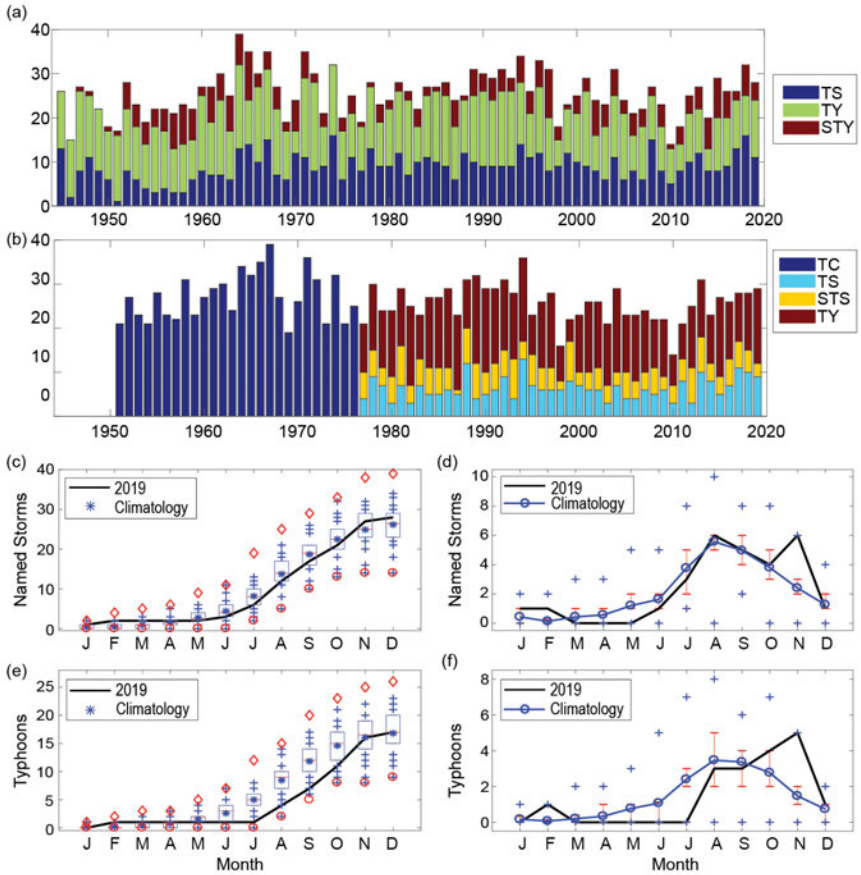

Fig. 4.27. (a) Number of tropical storms (TS) typhoons (TY) and super typhoons (STY) per year in the WNP for 1945–2019 based on JTWC. (b) Number of tropical cyclones (TC, all storms which reach TS intensity or higher) for 1951–1976; number of TSs, severe tropical storms (STS) and TY for 1977–2019 based on JMA. Panel (c) shows the cumulative number of TCs per month in the WNP in 2019 (black line) and climatology (1981–2010) as box plots (interquartile range: box, median: red line, mean: blue asterisk, values in the top or bottom quartile: blue crosses, high [low] records in the 1945–2018 period: red diamonds [circles]). Panel (e) is similar to panel (c) but for the number of TYs. Panels (d) and (f) show the number of TCs and TYs per month in 2019 (black line) and the climatological mean (blue line); blue "+"signs denote the maximum and minimum monthly historical records and the red error bars show the climatological interquartile range for each month. In the case of no error bars, the upper and/or lower percentiles coincide with the median. (Sources: 1945–2018 JTWC best-track dataset, 2019 JTWC preliminary operational track data, except for panel [b], which is 1951–2019 JMA best-track dataset.)

active late season compensated for the quiet early season, leading to a slightly above-average typhoon season in terms of the JTWC numbers of named storms (28, median = 26), typhoons (17, median = 16) and super typhoons (4, median = 3.5).

The total ACE in 2019 (Fig. 4.28a) was slightly below normal. As seen in Fig. 4.28b, the value for February, however, was the highest in the historical record. From March until July, the monthly ACE was in the bottom quartile of the monthly climatologies, with zero ACE values for March, April, and May. The August ACE was in the below-average quartile (25%–50%), and the September ACE was also in the bottom quartile of the monthly climatological distribution. The October and December ACE values were in the above-average quartile (50%–75%) of the climatological distributions, while November ACE was in the top quartile. The five months of October, November, August, September, and February contributed 26%, 22%, 16%, 14%, and 15% of the ACE respectively, summing to 93% of the seasonal ACE. In descending order of storm ACE, Super Typhoons Hagibis (top 5%), Wutip (top decile), and Halong, Typhoons Bualoi and Kammuri, and Super Typhoon Lekima placed in the top quartile of historical ACE per storm. Together, these six storms contributed 57% of the seasonal ACE, with Hagibis and Wutip contributing 14% and 12%, respectively.

Unauthenticated | Downloaded 12/18/20 02:55 PM UTC

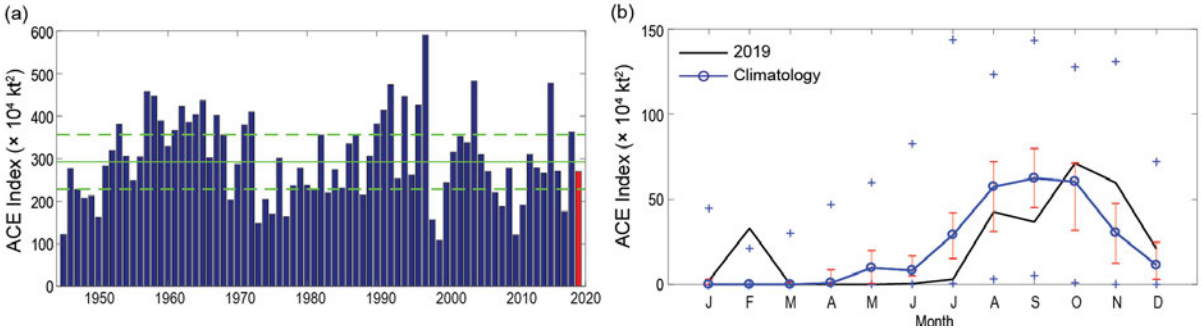

Fig. 4.28. (a) ACE per year in the WNP for 1945–2019. The solid green line indicates the median for 1981–2010; dashed lines show the climatological 25th and 75th percentiles. (b) ACE per month in 2019 (black line) and the 1981–2010 median (blue line); red error bars indicate the 25th and 75th percentiles. In case of no error bars, the upper and/or lower percentiles coincide with the median. The blue "+" signs denote the maximum and minimum values during the 1945–2018. (Source: 1945–2018 JTWC best-track dataset; 2019 JTWC preliminary operational track data.)

The mean genesis location in 2019 was 14.4°N, 138.4°E, slightly northwest of the climatological mean of 13.2°N, 142.8°E (std. dev. of 1.9° latitude and 5.6° longitude). The mean track position in 2019 was 19.0°N, 133.9°E, similarly northwest of the climatology mean of 17.3°N, 136.6°E (std. dev. of 1.4° latitude and 4.7° longitude). There is a well-known connection between genesis and track shifts in the WNP basin and ENSO phase (Chia and Ropelewski 2002; Camargo et al. 2007). However, the 2019 northwest shift in TC genesis and track cannot be attributed to El Niño, as there were neutral ENSO conditions during the peak typhoon season.

There were 110.25 named storm days in the WNP in 2019 (median = 113 days). The WNP had 50.25 typhoon days (bottom quartile ≤ 49.5 days) and 21.5 major typhoon days (SSHWS Categories 3–5; median = 21). The percentage of days with typhoons and major typhoons was 32% (bottom quartile ≤ 33%) and 14% (median = 13.9%) respectively. The median lifetime for TCs reaching TS intensity was 6.25 days (bottom percentile ≤ 6.25 days) and for those reaching typhoon intensity was eight days (bottom quartile ≤ 7.75 days). The longest-lived named storm in 2019 was Typhoon Matmo (12.25 days), followed by Major Typhoons Krosa (11.25 days), Wutip (11 days), and Kammuri (10.5 days)—all of which were in the top quartile (≥ 10.5 days). Tropical depression One was very long-lived as well (18 days). Of the 28 tropical storms and typhoons, 17 had a lifetime at or below the median (7.75 days), with 12 in the bottom quartile (≤ 5.25 days). The maximum number of TCs (and typhoons) active simultaneously in 2019 was three and occurred 7–9 November (Super Typhoon Halong and Typhoons Matmo and Nakri). The historical record is six (14–15 August 1996).

Including TDs, 23 storms made landfall in 2019, above the 90th percentile compared with the 1951–2010 climatology. Landfall here is defined when the storm track is over land, and the previous location was over the ocean. In order to include landfall over small islands, tracks were interpolated from 6-hourly to 15-minute intervals, using a high-resolution land mask. Seven storms made landfall as TDs (above the 95th percentile ≥ 7) and eight as tropical storms (top quartile ≥ 8). Six TCs made landfall as Category 1–2 typhoons on the SSHWS scale (median = 5): Francisco, Lekima, Faxai, Hagibis, Matmo, and Phanphone. Super Typhoons Lingling and Kammuri made landfall as major typhoons (Category ≥ 3; median = 2). Lingling affected both South and North Korea—the latter of which is not hit frequently by typhoons. Kammuri made landfall in the Bicol region of the Philippines on 2 December, followed by Typhoon Phanphone's landfall in the country's eastern Samar region on 24 December. Five storms made landfall in Japan in 2019 (top quartile ≥ 5), with the strongest being Typhoons Faxai and Hagibis.

(III) ENVIRONMENTAL CONDITIONS

Figures 4.29a–e show the July–October (JASO) environmental conditions associated with typhoon activity in 2019. The 2018/19 El Niño transitioned to near- to below-normal SSTs in the eastern Pacific during the beginning of the peak typhoon season (July to mid-September). From mid-September

Unauthenticated | Downloaded 12/18/20 02:55 PM UTC

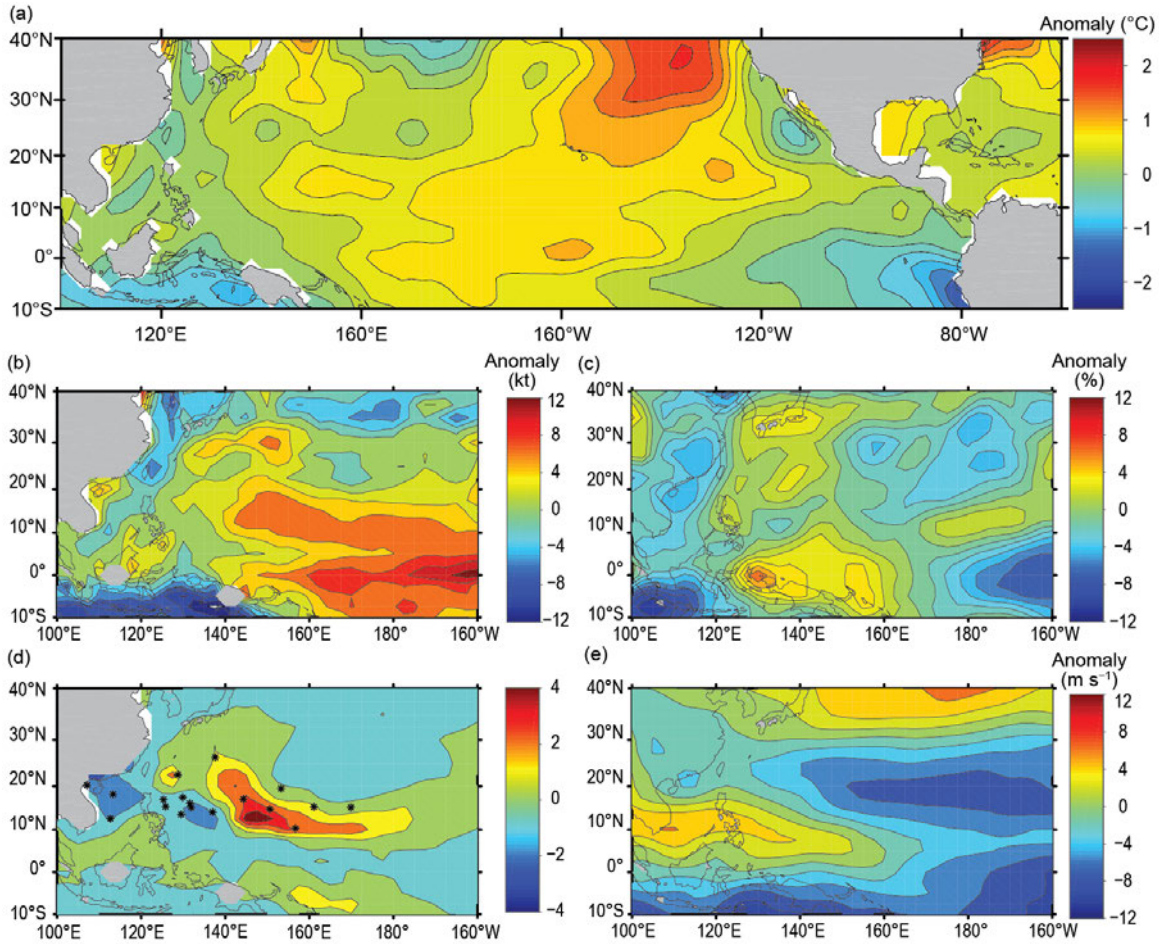

Fig. 4.29. (a) SST anomalies (°C) for Jul–Oct (JASO) 2019. (b) Potential intensity anomalies in JASO 2019 (kt). (c) Relative humidity (%) 600-hPa anomalies in JASO 2019. (d) Genesis potential index (unitless) anomalies in JASO 2019. First position of storms in JASO 2019 are marked with an asterisk. (e) 850-hPa zonal winds (m s^{-1}) in JASO 2019. (Source: atmospheric variables: NCEP–NCAR reanalysis data [Kalnay et al. 1996]; SST [Smith et al. 2008].)

until the end of the calendar year, above-normal SSTs expanded from the date line into the eastern Pacific. Below-normal eastern Pacific SSTs are clearly seen in the JASO SST anomalies (Fig. 4.29a), with above-average SST anomalies extending northeastward from the equatorial central Pacific around these cold anomalies. The above-average SST anomalies in the central Pacific are reflected in other environmental variables, such as positive potential intensity anomalies (Fig. 4.29b) in the eastern part of the basin near the date line. There was also a positive band of 600-hPa relative humidity anomalies between 130°–160°E extending from the equatorial region to ~40°N (Fig. 4.29c). For the genesis potential index (GPI; Fig. 4.29d; Emanuel and Nolan 2004; Camargo et al. 2007), anomalies are observed in a recurving narrow band between 10°–20°N. Many TC genesis locations occurred close to or just southwest of this region. The extent of the monsoon trough, defined by 850-hPa zonal winds (Fig. 4.29e), extended to 150°E, despite below-normal SSTs in the eastern Pacific. Several cases of TC genesis occurred just north of these westerly anomalies.

(IV) TROPICAL CYCLONE IMPACTS

Many storms had social and economic impacts in Asia in 2019, particularly Typhoons Lekima, Faxai, and Hagibis. Typhoon Lekima made landfall in China as the fifth-strongest landfalling typhoon to affect the country since 1949, according to the China Meteorological Administration. Lekima's heavy rainfall and long duration over China led to many historical daily precipitation records across the country, particularly in Zhejiang Province, where the typhoon made its first landfall. Lekima then passed over Shanghai and Jiangsu Province, before making a second landfall in Shangdong Province. Lekima left 48 dead and 21 missing, and displaced 1.7 million

Unauthenticated | Downloaded 12/18/20 02:55 PM UTC

people. Damages were estimated to be $9.3 billion (U.S. dollars). Typhoon Faxai impacted Japan as one of the strongest typhoons on record to affect Tokyo, killing three people and injuring 147, causing extensive blackouts, and damaging more than 40 000 homes. Japan's economic losses across several sectors due to Faxai are estimated at $7 billion (U.S. dollars). In October, Super Typhoon Hagibis affected the Tokyo region. The storm's record-breaking rainfall led to extensive flooding of rivers and dams and multiple landslides. At least 95 people were killed, 460 injured, and economic losses exceeded $10 billion (U.S. dollars).

5) North Indian Ocean basin—A. D. Magee and C. J. Schreck

(I) SEASONAL ACTIVITY

The North Indian Ocean (NIO) TC season typically occurs between April and December, with two peaks of activity: May–June and October–December, due to the presence of the monsoon trough over tropical waters of the NIO during these periods. Tropical cyclone genesis typically occurs in the Arabian Sea and Bay of Bengal between 8°–15°N. The Bay of Bengal, on average, experiences four times more TCs than the Arabian Sea (Dube et al. 1997).

The 2019 NIO TC season was a particularly active and record-breaking TC season with eight named storms, six cyclones, and three major cyclones (tied 1999), compared to the IBTrACS–JTWC 1981–2010 climatology of 4.9, 1.5, and 0.7, respectively (Fig 4.30a). One event, Cyclone Kyarr, was the second-most intense cyclone ever observed in the Arabian Sea. The 2019 NIO TC season was also the second-costliest on record with losses exceeding $11 billion (U.S. dollars).

Record-breaking ACE index values and a strongly positive Indian Ocean dipole (IOD) event characterized the 2019 NIO TC season (refer to the legend of Fig. 4.38 for the definition of IOD and its polarity). The 2019 seasonal ACE index was 85×10^4 kt^2. It nearly doubled the previous record holders (2007 and 2013 each had about 45×10^4 kt^2) and was over four times the 1981–2010 ACE climatology (19×10^4 kt^2; Fig 4.30b). The strong positive IOD event that marked the latter half of the 2019 season is clearly seen in Fig 4.31a, where anomalously warm SSTs occurred in the western tropical Indian Ocean (10°N–10°S, 50°–70°E). In addition, enhanced convection (Fig 4.31b) and negative vertical wind shear anomalies (Fig 4.31c) provided favorable conditions in the Arabian Sea, contributing to the high number of events there. Although positive IOD events historically result in fewer TCs in the NIO (Yuan and Cao 2012), this was not the case for the 2019 TC season.

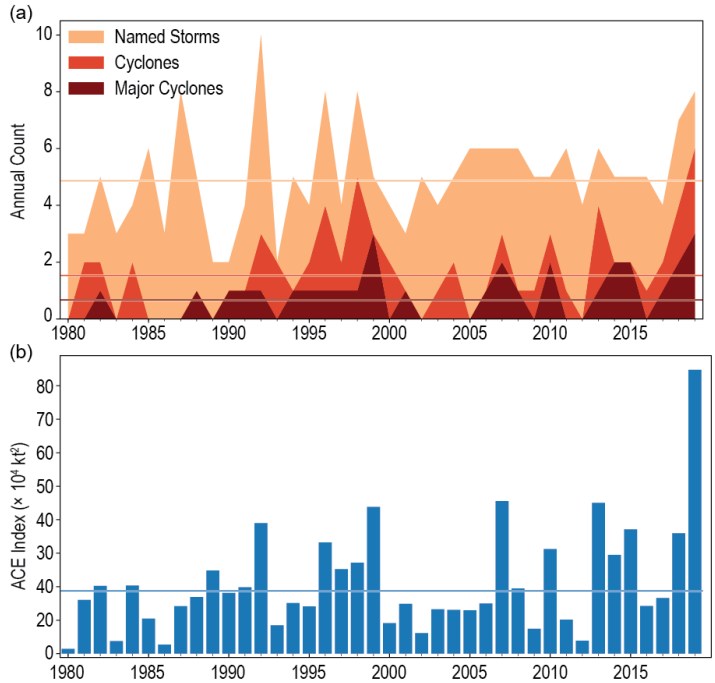

Fig. 4.30. Annual TC statistics for the NIO for 1980–2019: (a) number of named storms, cyclones, and major cyclones and (b) estimated annual ACE index ($\times 10^4$ kt^2) for all TCs during which they were at least tropical storm strength or greater intensity (Bell et al. 2000). Horizontal lines represent 1981–2010 climatology.

(II) NOTEWORTHY TROPICAL CYLONES AND IMPACTS

The first severe cyclonic storm of the 2019 NIO cyclone season, Cyclone Fani (27 April–3 May), developed unusually close to the equator, at 2.7°N, just west of Sumatra. Strong vertical wind shear impeded further development until 29 April when Fani intensified into a severe cyclonic storm. On 30 April, favorable conditions aided further intensification before Fani recurved north-northeastward toward India. It then underwent additional intensification, reaching its peak intensity of 135 kt (69 m s^{-1}) and a minimum central

Unauthenticated | Downloaded 12/18/20 02:55 PM UTC

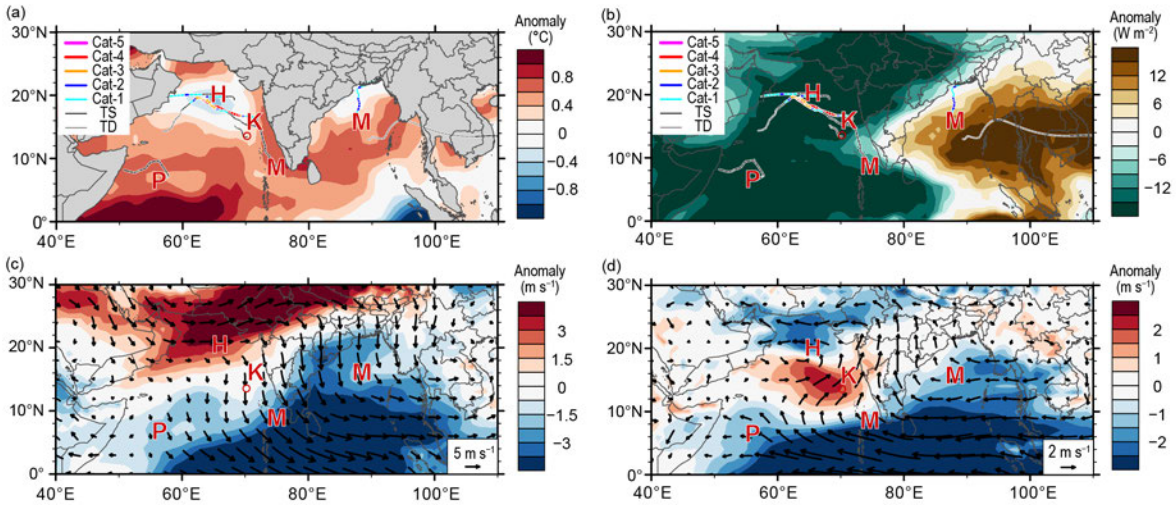

Fig. 4.31. 15 Sep 2019–15 Dec 2019 NIO anomaly maps of (a) SST (°C; Banzon and Reynolds 2013), (b) OLR (W m^{-2}; Schreck et al. 2018), (c) 200–850-hPa vertical wind shear (m s^{-1}) vector (arrows) and scalar (shading) anomalies, and (d) 850-hPa winds (m s^{-1}, arrows) and zonal wind (shading) anomalies. Anomalies are relative to the annual cycle from 1981–2010, except for SST, which is relative to 1982–2010 due to data availability. Letter symbols denote where each NIO TC attained its initial tropical storm intensity. Wind data are obtained from CFSR (Saha et al. 2014).

pressure of 917 hPa, equivalent to a strong Category 4 system on the SSHWS. Fani made landfall near Odisha, India, on 3 May with 1-minute maximum sustained wind speeds of 120 kt (62 m s^{-1}). Fani eventually weakened and moved into Bangladesh on 4 May before dissipating the following day. In total, 89 people were killed with estimated damages of approximately $8.1 billion (U.S. dollars). A storm surge of approximately 1.5 m and heavy rainfall resulted in extensive damage, including to agricultural land, where more than 30% of crops were damaged. In Bangladesh, 17 people were killed, many by lightning. Around 160 000 acres of farmland was destroyed, with agricultural losses in Bangladesh totaling $4.6 million (U.S. dollars).

Cyclone Vayu (10–17 June) formed in the southeastern Arabian Sea, aided by a strong convective pulse of the MJO. Vayu reached peak intensity on 13 June, with 1-minute maximum sustained winds of 95 kt (48 m s^{-1}), and a minimum central pressure of 950 hPa, a Category 2 SSHWS equivalent system. During its lifetime, Vayu's track recurved several times before weakening to a tropical low off the coast of Gujarat, India, and passed over the coast on 18 June. Vayu's proximity to Gujarat and surrounding regions resulted in eight deaths and an estimated $140 000 (U.S. dollars) in damages. Cyclone-generated waves and swells resulted in flooding of low-lying areas in Oman and Pakistan. Vayu contributed to an approximate one-week delay in the northward migration of the Indian monsoon, which was already delayed by weakening El Niño conditions that persisted during the early part of the 2019 monsoon season.

The fourth cyclone of the season, Hikaa (22–25 September), developed in the Arabian Sea and intensified into a severe cyclonic storm, reaching peak intensity of 85 kt (43 m s^{-1}) and a minimum central pressure of 972 hPa, a Category 2 SSHWS equivalent system. Hikaa tracked toward the west before making landfall near Duqm, Oman, on 24 September. As a result of Hikaa, a boat carrying 11 Indian fishermen reportedly sank, while another boat sank off the coast of Duqm.

Super Cyclone Kyarr (24 October–1 November) was the second-most intense cyclone ever observed in the Arabian Sea with a peak intensity of 135 kt (69 m s^{-1}) and a minimum central pressure of 923 hPa. After forming in the southeastern Arabian Sea, high SSTs and low vertical wind shear favored rapid intensification. Kyarr reached Super Cyclonic Storm strength (India Meteorological Department 2020) on 27 October—the first in the Arabian Sea since Cyclone Gonu in 2007. Unfavorable conditions resulted in a weakening of Kyarr, and it later dissipated on 1 November. No fatalities were recorded as a result of Kyarr; however, strong winds and intense rainfall caused flash flooding in Goa, India. High tide and extreme sea levels associated with

Unauthenticated | Downloaded 12/18/20 02:55 PM UTC

Kyarr caused coastal flooding in Oman, with extensive damage to the Muttrah Corniche as well as a portion of the coastline of the United Arab Emirates.

Cyclone Maha (30 October–6 November), the season's fourth cyclonic storm to originate in the Arabian Sea (compared to an average of one), intensified in a similar fashion to, and occurred concurrently with, Cyclone Kyarr. Maha underwent rapid intensification from depression to cyclonic storm within a 12-hour period. The peak intensity of Maha on 4 November was 105 kt (54 m s^{-1}) and a minimum central pressure of 959 hPa, a Category 3 SSHWS equivalent system. Maha generally tracked toward the northwest throughout its lifetime, parallel to the west coast of India, and generated storm surge up to 0.5 m (at Asarsa and Tankaria) on 2 November. Upwelling of cooler SSTs weakened Maha, and it made landfall as a depression near Gujarat and dissipated shortly thereafter.

Cyclone Bulbul (7–10 November) originated in the Bay of Bengal from a previous disturbance, Severe Tropical Storm Matmo, and emerged into the north Andaman Sea. After tracking west-northwestward toward the central Bay of Bengal, Bulbul moved to the north, intensifying to a very severe cyclonic storm on 8 November, with 1-minute maximum wind speeds of 85 kt (43 m s^{-1}) and a minimum central pressure of 971 hPa, a Category 2 SSHWS equivalent system. Bulbul made landfall near the Sagar Islands of West Bengal on 9 November. It brought significant rainfall, with reports of 24-hour accumulations of up to 202 mm in Canning, West Bengal. In total, 41 people died, with estimated damage totaling $3.38 billion (U.S. dollars). In the state of Odisha, rainfall caused agricultural damage, including an estimated 200 000 ha of damaged crops. In Bangladesh, more than two million people fled to shelters, 25 people died, and approximately 14% of Bangladesh's total farmland was damaged, equating to agricultural losses of approximately $31 million (U.S. dollars).

6) South Indian Ocean basin—A. D. Magee and C. J. Schreck

(I) SEASONAL ACTIVITY

The South Indian Ocean (SIO) TC basin extends south of the equator and from the African coastline to 90°E. In the SIO, TC genesis typically occurs south of 10°S. While the SIO TC season extends year-round, from July to June, the majority of activity occurs between November and April when the ITCZ is located in the SH. The 2018/19 TC season includes TCs that occurred from July 2018–June 2019. Landfalling TCs typically impact Madagascar, Mozambique, and the Mascarene Islands, including Mauritius and Réunion Island. The Regional Specialized Meteorological Centre (RSMC) on La Réunion is the official monitoring agency for TC activity within the SIO basin.

The 2018/19 SIO season had 11 named storms, 10 cyclones, and eight major cyclones (Fig 4.32a), compared to the IBTrACS–JTWC 1981–2010 mean of 9.1, 5.5, and 2.9, respectively (Schreck et al., 2014). The eight major cyclones broke the previous record of seven in 1993/94. The 2018/19 SIO season also had a record-breaking number of cyclone days, 39 days in total, overtaking the previous records of 1993/94 (36 days) and 2001/02 (35 days). Unfortunately, the season also set records for deaths and economic losses with over 1300 fatalities and total damage exceeding $2.3 billion (U.S. dollars). Cyclone Idai caused the majority of deaths and damage and was one of the worst natural disasters on record to impact southern Africa.

The 2018/19 seasonal ACE index was 154×10^4 kt^2, above the 1981–2010 SIO average of 92×10^4 kt^2 (Fig. 4.32b). Cyclone-favorable environmental conditions, including anomalously warm SSTs (Fig. 4.33a), enhanced convection (Fig. 4.33b), and anomalously weak shear (Fig. 4.33c) were present where the majority of TCs developed. The presence of low-level westerly anomalies along 10°S enhanced cyclonic vorticity for many systems, excluding TCs east of 70°E, where easterly anomalies predominated.

(II) NOTEWORTHY TROPICAL CYCLONES AND IMPACTS

The first named cyclone of the season intensified to a Category 3 SSHWS equivalent system, with maximum 1-minute sustained winds of 100 kt (51 m s^{-1}) and a minimum central pressure of

Unauthenticated | Downloaded 12/18/20 02:55 PM UTC

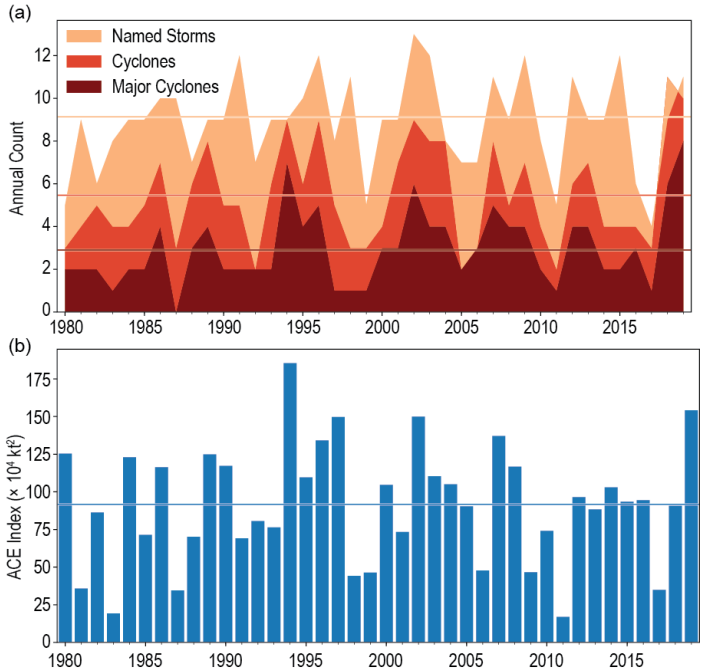

Fig. 4.32. Annual TC statistics for the SIO for 1980–2019: (a) number of named storms, cyclones, and major cyclones and (b) estimated annual ACE index (× 10^4 kt^2) for all TCs during which they were at least tropical storm strength or greater intensity (Bell et al. 2000). Horizontal lines represent 1981–2010 climatology.

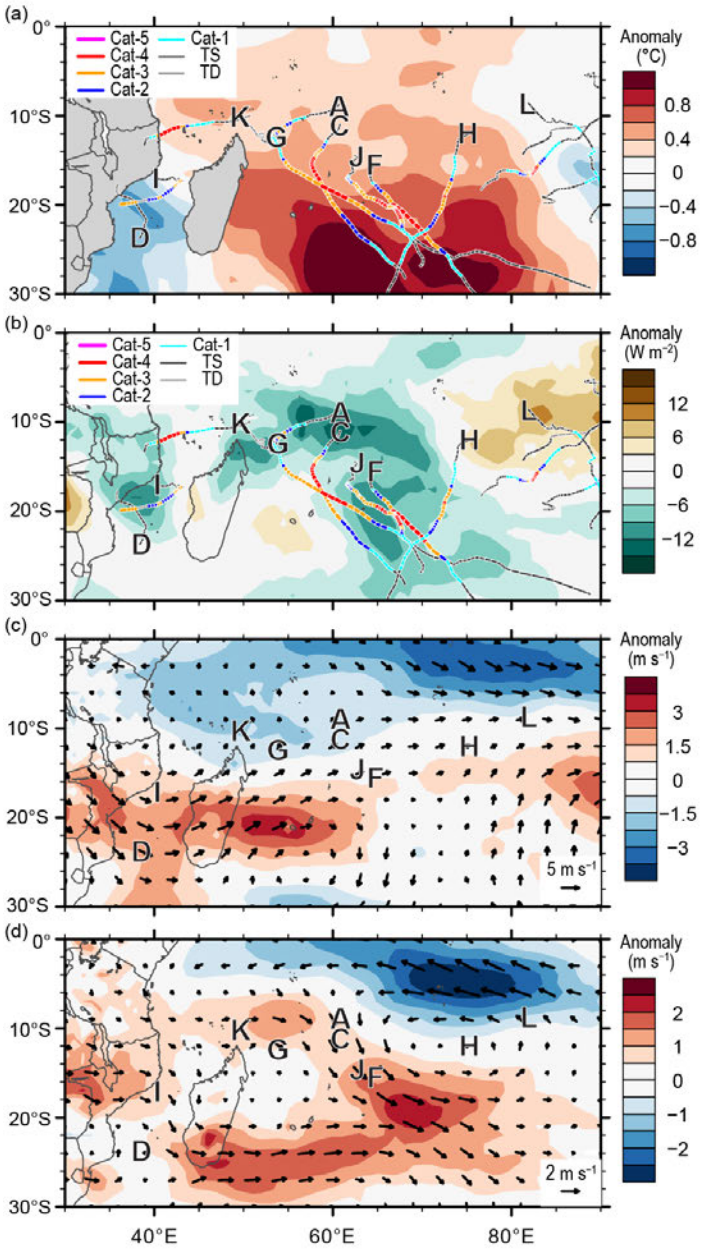

Fig. 4.33. Nov 2018–Apr 2019 SIO anomaly maps of (a) SST (°C; Banzon and Reynolds 2013); (b) OLR ($W m^{-2}$; Schreck et al. 2018); (c) 200–850-hPa vertical wind shear ($m s^{-1}$) vector (arrows) and scalar anomalies (shading), and (d) 850-hPa winds ($m s^{-1}$ arrows) and zonal wind anomalies (shading). Anomalies are relative to the annual cycle from 1981–2010, except for SST, which is relative to 1982–2010. Letter symbols denote where each SIO TC attained its initial tropical storm intensity. (Source: Wind data from CFSR [Saha et al. 2014].)

965 hPa. After tracking in a west-southwesterly direction toward Madagascar, Cyclone Alcide (6–13 November 2018) quickly weakened due to less favorable conditions and did not make landfall, although it did cause minor damage on the Mauritian island of Agaléga.

Cyclone Desmond (20–22 January 2019) formed as a TD off the east coast of Mozambique and recurved several times before tracking toward the northeast. Desmond intensified into a moderate TS with a peak intensity of 45 kt (23 $m s^{-1}$) and minimum central pressure of 993 hPa. Desmond made landfall in Mozambique approximately 200 km north of Beira, bringing 277 mm of rainfall over a 24-hour period. Significant flooding resulted in deaths of over 1000 livestock and affected approximately 60 000 ha of crops.

Cyclone Galena (6–15 February) intensified northeast of Mauritius and reached a peak intensity of 120 kt (61 $m s^{-1}$) with a minimum central pressure of 933 hPa, a Category 4 SSHWS equivalent system. It passed within 35 km of Rodrigues where wind gusts of 90 kt (46 $m s^{-1}$) were recorded. Winds associated with Galena devastated the agricultural sector on Rodrigues and damaged approximately 90% of the island's electricity grid.

Cyclone Idai (4–16 March), a Category 3 SSHWS equivalent system, was the deadliest TC ever recorded in the SIO basin. Over 1300 people lost their lives, and 3 million people were affected or displaced across Mozambique, Zimbabwe, Malawi, and Madagascar. Idai made two landfalls over

Unauthenticated | Downloaded 12/18/20 02:55 PM UTC

Mozambique. It remained over Mozambique for five days after its first landfall (4 March) before moving offshore. Just before Idai's second landfall, the system intensified, reaching peak intensity with maximum 1-minute sustained winds of 105 kt (54 m s^{-1}) and minimum central pressure of 944 mb. Its second landfall was near Beira, Mozambique, on 15 March, and it remained over Mozambique for three days. Multiple landfalls amplified the impacts associated with Idai, which are described in Sidebar 7.3.

Cyclone Joaninha (22–31 March), a Category 4 SSHWS equivalent system, formed to the east of Madagascar. On 24 March, Joaninha achieved peak intensity, with maximum 1-minute sustained winds of 115 kt (59 m s^{-1}) and a minimum central pressure of 937 hPa. Cyclone Joaninha was a slow-moving storm and passed within ~80 km of Rodrigues, Mauritius, with cyclonic conditions persisting there for more than 34 hours. Wind gusts up to 100 kt (51 m s^{-1}) and rainfall accumulations of 200 mm were recorded, resulting in widespread power cuts and flooding.

Cyclone Kenneth (23–26 April) was the most intense landfalling TC in Mozambique's observational record and also resulted in significant damage to the Comoro Islands, Tanzania, and Mozambique. At its peak, Kenneth reached a maximum intensity of 125 kt (64 m s^{-1}), a category 4 SSHWS equivalent system. It passed ~60 km north of Grande Comore Island and resulted in significant impacts there, which are described in Sidebar 7.3. Kenneth made landfall on 25 April, north of Pemba, Mozambique, with 1-minute sustained winds of 120 kt (61 m s^{-1}). Kenneth's widespread destruction in Mozambique came as the nation was still coming to terms with the substantial impacts of TC Idai, just six weeks before.

7) Australian basin—B.C. Trewin

(I) SEASONAL ACTIVITY

The 2018/19 TC season was near normal in the broader Australian basin (areas south of the equator and between 90°E and 160°E,[3] which includes Australian, Papua New Guinea, and Indonesian areas of responsibility). The season produced 11 TCs, which is near the 1983/84–2010/11 average[4] of 10.8, and is consistent with neutral ENSO conditions. The 1981–2010 IBTrACS seasonal averages for the basin are 9.9 named storms, 7.5 TCs, and 4.0 major TCs, which compares with the 2018/19 counts of 10, six, and two, respectively (Fig 4.34).

There were six TCs in the western sector[5] of the broader Australian region during 2018/19, four in the northern sector, and five in the eastern sector.[6] Three systems made landfall in Australia as TCs (two on multiple occasions), affecting Queensland and the Northern Territory, while a fourth approached the coast closely enough to have major impacts on land on the Pilbara coast in Western Australia. All cyclone categories referred to in this section are based on the Australian cyclone categorization scale.

(II) LANDFALLING AND OTHER SIGNIFICANT TROPICAL CYCLONES

The strongest cyclone of the season was Veronica, which approached the Pilbara coast in late March. Veronica was named at 1800 UTC on 19 March near 15°S, 120°E. It intensified rapidly over the following 24 hours while moving generally west-southwest, and it reached Australian Category 5 intensity at 0000 UTC on 21 March, near 17°S, 118°E, with maximum sustained 10-minute wind speeds of 115 kt (59 m s^{-1}) and a central pressure of 928 hPa. It weakened slightly as it moved toward

[3] The Australian Bureau of Meteorology's warning area overlaps both the southern Indian Ocean and southwest Pacific.

[4] Averages are taken from 1983/84 onward as that is the start of consistent satellite coverage of the region.

[5] The western sector covers areas between 90°E and 125°E. The eastern sector covers areas east of the eastern Australian coast to 160°E, as well as the eastern half of the Gulf of Carpentaria. The northern sector covers areas from 125°E east to the western half of the Gulf of Carpentaria. The western sector incorporates the Indonesian area of responsibility, while the Papua New Guinea area of responsibility is incorporated in the eastern sector.

[6] Trevor and Owen passed through both the northern and eastern sectors, Wallace through both the northern and western sectors, and Lili through both the northern sector and the Indonesian warning area of responsibility, which is included with the western sector.

Unauthenticated | Downloaded 12/18/20 02:55 PM UTC

the coast but was still at Category 4 intensity near the coast, about 100 km northeast of Karratha, at 0000 UTC on 24 March. Veronica then remained near-stationary, moving less than 50 km in 24 hours, while slowly weakening, before resuming its movement west, parallel to the Pilbara coast. It weakened below TC intensity by 0000 UTC on 26 March. The remnant low crossed North West Cape later that day before dissipating to the west.

While Veronica did not make landfall as a TC, its prolonged presence caused extended shutdowns of mining, oil, and gas industries in the region, with economic losses from lost production estimated at over $1.4 billion (U.S. dollars). There was also heavy rain in the Pilbara region, with 72-hour totals for 24–26 March of 634 mm at Indee, 572 mm at Sherlock, 539 mm at Mallina, 470 mm at Upper North Pole (near Marble Bar), and 356 mm at Port Hedland. Local and river flooding caused traffic disruptions and some livestock losses.

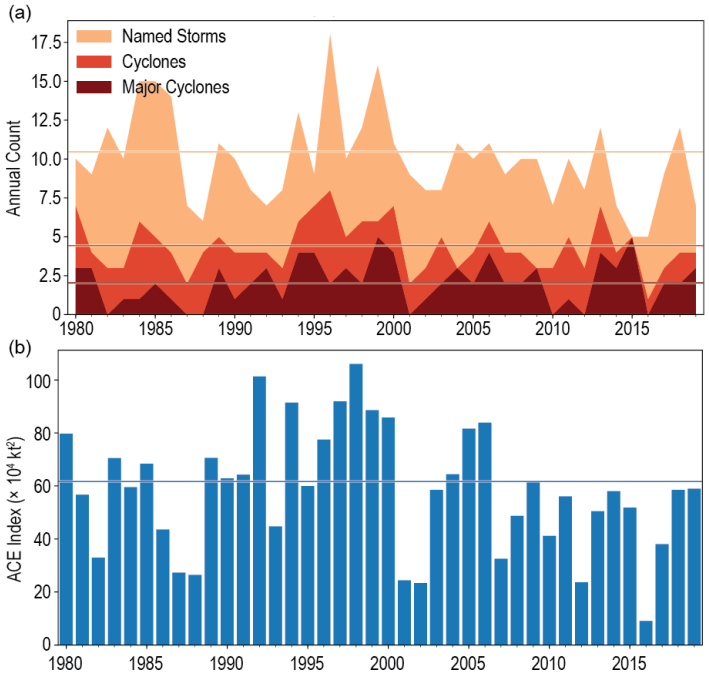

Fig. 4.34. Annual TC statistics for the Australian basin for 1980–2019: (a) number of named storms, cyclones, and major cyclones and (b) the estimated annual ACE (× 10^4 kt^2) for all TCs at least tropical storm strength or greater intensity (Bell et al. 2000). The 1981–2010 means (horizontal lines) are included in both (a) and (b).

On 17 March, TC Trevor formed in the Coral Sea at 1800 UTC. It moved west while intensifying and made its initial landfall as a Category 3 system near Lockhart River, on the Cape York Peninsula, around 0900 UTC on 19 March. It weakened to a Category 1 system while crossing the Peninsula, before re-emerging south of Weipa on the morning of 21 March. Once over the Gulf of Carpentaria, Trevor reintensified rapidly while moving southwest, reaching Category 4 intensity early on 23 March with maximum sustained winds of 95 kt (49 m s^{-1}) while off the coast west of the Northern Territory–Queensland border. It made landfall around 0000 UTC at slightly below-peak intensity, east of Port McArthur on the Northern Territory coast. The system weakened below TC intensity that evening as it moved inland, but it remained as a remnant low for several days, initially moving south through the eastern Northern Territory and then east through Queensland, finally dissipating near Richmond on 28 March.

There was substantial tree and some building damage near the point of Trevor's initial landfall at Lockhart River. The second landfall was in a sparsely populated area, and few impacts were reported. Storm surge heights east of that landfall reached 1.8 m at Burketown and 1.7 m at Mornington Island. Precautionary evacuations were carried out in a number of communities on the island of Groote Eylandt and parts of the Northern Territory coast. The heaviest rainfalls from Trevor were near the point of its Cape York Peninsula landfall, with 302 mm (and a two-day total of 421 mm) at Lockhart River on 20 March and 211 mm at Aurukun on 21 March. East of Trevor's second landfall, Westmoreland Station received 282 mm on 24 March. Following landfall, numerous daily rainfalls exceeding 100 mm were recorded in the eastern Northern Territory and far western Queensland, including 178 mm on 27 March at Trepell Airport, north of Boulia. The post-landfall rains caused widespread flooding on both sides of the Northern Territory–Queensland border, with significant cattle losses in some areas. Floodwaters moved south and eventually contributed to a partial filling of Lake Eyre.

TC Owen initially formed in the Coral Sea on 2 December, but soon weakened and moved west before making landfall near Port Douglas as a tropical low early on 10 December. The system crossed Cape York Peninsula and emerged over the Gulf of Carpentaria, moving west and

Unauthenticated | Downloaded 12/18/20 02:55 PM UTC

intensifying to Category 3 intensity with maximum sustained winds of 80 kt (41 m s^{-1}). It briefly touched the Northern Territory coast north of Port McArthur early on 13 December, at peak intensity, before beginning to move east and almost retracing its path across the Gulf. It made landfall again on the east coast of the Gulf, near the mouth of the Gilbert River, at slightly below-peak intensity, at about 1900 UTC on 14 December. Owen weakened to a tropical low that crossed Cape York Peninsula a second time and re-emerged into the Coral Sea. The two cyclone-intensity landfalls of Owen were both in remote, sparsely populated areas, and few impacts were reported. The major impacts were from flooding on the east coast during its tropical low phases. On 10 December, Kirrama Range (west of Cardwell) received 349 mm, but the most extreme rainfall occurred where the low moved offshore late in its lifetime. On 16 December, 681 mm fell at Halifax, the heaviest daily total recorded in Australia in December, and a number of other sites on the east coast exceeded 500 mm. There was substantial local flooding and some crop damage was reported.

The season's other landfall was Penny, which peaked at Category 2 intensity in the Coral Sea after crossing Cape York Peninsula from the west and reforming. It made landfall near Weipa as a Category 1 system on the afternoon of 1 January. Savannah remained well off the coast of western Australia while peaking at Category 4 intensity in mid-March, but the precursor low brought heavy rain to the Indonesian island of Java, with substantial flooding and some loss of life.

8) Southwest Pacific basin—J.-M. Woolley, P. R. Pearce, A. M. Lorrey, and H. J. Diamond

(I) SEASONAL ACTIVITY

The 2018/19 TC season in the southwest Pacific officially began in November 2018 and ended in April 2019; however there was both early and late activity in this region with "out of season" storms. Storm track data for 2018/19 were gathered from the Fiji Meteorological Service, Australian Bureau of Meteorology, and New Zealand MetService, Ltd. The southwest Pacific basin (defined by Diamond et al. 2012 as 135°E–120°W) had nine TCs, including four severe TCs (based on the Australian TC intensity scale). As noted in section 4e1, Fig. 4.35 shows the standardized TC distribution based on the basin spanning the area from 160°E–120°W to avoid overlaps with the Australian basin that could result in double counting of storms. However, it is important to use the definition of the southwest Pacific basin of Diamond et al. (2012) as that is how annual TC outlooks are produced and disseminated.

The 1981–2010 Southwest Pacific Enhanced Archive of Tropical Cyclones (SPEArTC) indicates a seasonal average of 10.4 named TCs and 4.3 severe TCs. The 2018/19 TC season therefore had near-normal activity with nine named TCs, of which four were severe. The first and last storm formed outside of the formally defined TC season, with TC Liua occurring in the Solomon Sea in late September 2018 and TC Ann developing in May 2019. The ratio of severe TCs relative to the total number of named TCs in 2018/19 was 44%, which is 6% lower than the previous season.

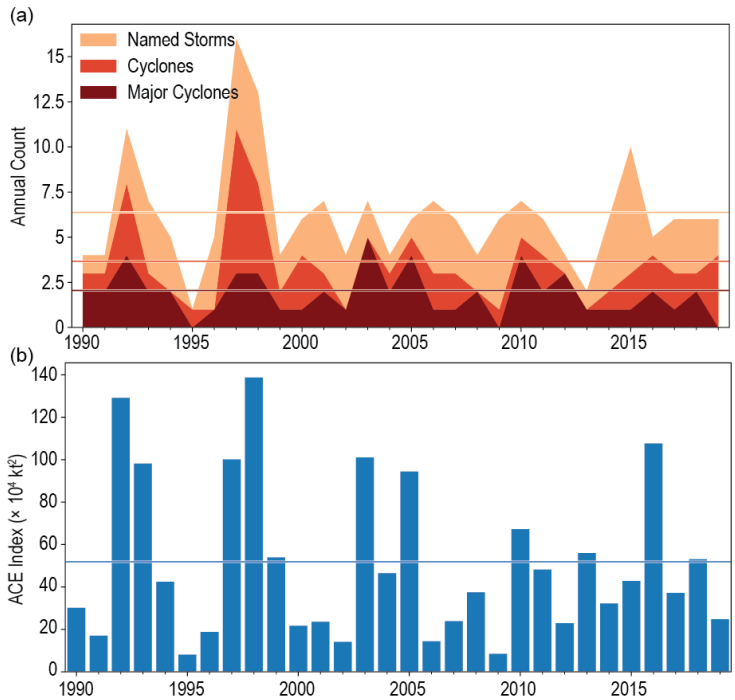

Fig. 4.35. Annual TC statistics for the southwest Pacific for 1980–2019: (a) number of named storms, cyclones, and major cyclones and (b) the estimated annual ACE index (× 10^4 kt^2) for all TCs at least tropical storm strength or greater intensity (Bell et al. 2000). The 1981–2010 means (horizontal lines) are included in both (a) and (b).

Unauthenticated | Downloaded 12/18/20 02:55 PM UTC

(II) LANDFALLING AND OTHER SIGNIFICANT TROPICAL CYCLONES

The first named TC of the 2018/19 season was reported as a tropical disturbance on 24 September 2018 to the east-northeast of Port Moresby in Papua New Guinea. On 26 September, the system moved southeast and intensified into a Category 1 TC named TC Liua. After intensifying to Category 1, TC Liua turned west and began to track toward Port Moresby, weakening into a TD on 28 September and further dissipating over the northern Coral Sea over the following days. TC Liua's peak 10-minute sustained winds were 40 kt (21 m s^{-1}) and its minimum central pressure was 994 hPa.

Severe TC Owen began as a low-pressure system over the Solomon Islands that developed into a tropical low on 29 November. The system became more organized the following day as it tracked southwest toward Tagula Island, then strengthened further as it tracked over the Coral Sea in favorable conditions. On 2 December, the system was classified as a Category 1 TC, but Owen weakened rapidly on 4 December and was downgraded to a tropical low. The degradation into a tropical low was temporary, as this system made landfall north of Cardwell, Queensland, on 10 December and re-attained Category 1 intensity on 11 December over the Gulf of Carpentaria. TC Owen looped and tracked back east, peaking as a Category 3 severe TC with maximum 10-minute sustained winds of 81 kt (42 m s^{-1}). On 15 December, TC Owen made landfall near Kowanyama as a low-end Category 3 severe TC. TC Owen's passage over northern Queensland brought heavy rainfall to the region.

Penny was the third TC of the season, which began as a tropical low located near the eastern coastline of Cape York Peninsula, Queensland, in late December 2018. The system tracked westward, emerging in the Gulf of Carpentaria on 31 December before turning eastward and strengthening into a Category 1 storm on the same day. On 1 January, TC Penny made landfall on the western Cape York Peninsula coastline, south of Weipa and was downgraded to a gale-force tropical low as it weakened over land. On 2 January, TC Penny achieved Category 1 status again after reorganizing over the Coral Sea. TC Penny's peak 10-minute sustained winds were 51 kt (26 m s^{-1}), and its minimum central pressure was 987 hPa.

TC Mona began as a tropical low near the southern Solomon Islands in a trough stretching across the northern Coral Sea. On 3 January, TC Mona achieved Category 1 status, north of Fiji. Mona intensified to Category 2 status the following day. It then tracked south toward Fiji and dissipated on 7 January. Approximately 2000 people took shelter in evacuation centers, and 30 roads were closed, mostly due to floods and some landslides. TC Mona's peak 10-minute sustained winds were 51 kt (26 m s^{-1}), and its minimum central pressure was 985 hPa.

Severe TC Oma began as a tropical low which had developed within an active monsoon trough along the coast of Vanuatu on 7 February. On 11 February, Oma intensified into a TC, quickly reaching Category 2 TC intensity. Oma achieved Category 3 TC status on 16 February, and again on 19 February following a brief weakening. Oma's peak 10-minute sustained winds were 70 kt (36 m s^{-1}), and its minimum central pressure was 974 hPa. Oma weakened to a Category 2 TC as it tracked southwest toward the Australian coast. On 22 February, TC Oma transitioned into a subtropical cyclone while turning to the northeast and continued to weaken further over the following days as it tracked farther in this direction. On 27 February, Oma turned eastward, while situated over Vanuatu, and dissipated on 28 February.

During early February, TC Oma pushed a bulk carrier freighter aground on a coral reef in the Solomon Islands, resulting in an oil spill, with an estimated cleanup cost of $50 million (U.S. dollars). Vanuatu was affected for several days by persistent heavy rain, damaging surf, and strong winds, particularly in the northern provinces of Malampa, Sanma, and Torba. Storm surge reportedly extended up to 50 m inland in some locations, impacting houses along the coast, particularly those constructed using traditional methods. In Torba, communications and transport links to the north were disrupted while flooding cut off road access to main services such as the hospital. New Caledonia was also impacted by heavy rain and damaging winds from TC Oma.

Unauthenticated | Downloaded 12/18/20 02:55 PM UTC

Thousands of people there were left without power while flooding made some roads impassable. Agriculture in New Caledonia was significantly affected, and the French government released $1.43 million (U.S. dollars) for recovery. Queensland was hit by large swells for about one week, causing significant beach erosion. More than 30 people required rescue, with some hospitalized, due to turbulent waters. One person drowned just off North Stradbroke Island. Heavy winds also damaged Cavendish banana plantations in Cudgen, New South Wales.

Severe TC Pola began as a tropical disturbance that formed northeast of Tonga on 23 February. Pola intensified into a TD while moving slowly southward. Pola became a Category 1 TC on 26 February and intensified into a Category 2 TC later that day. On 27 February, the system became a severe TC. On 28 February, Pola reached its peak intensity as a Category 4 TC with 10-minute sustained winds of 89 kt (46 m s^{-1}) and a minimum central pressure of 950 hPa.

Severe TC Trevor originated as a tropical low which formed off of the east coast of Papua New Guinea on 15 March. The system tracked southeast, crossing Papua New Guinea south of Port Moresby on 16 March. On 19 March, Trevor made landfall on the far northeast of the Queensland coast as a Category 3 severe TC and crossed Cape York Peninsula, downgrading to a Category 1 storm as it did so. As TC Trevor tracked southwest across the Gulf of Carpentaria, it intensified rapidly to a Category 4 system and then made landfall on the Northern Territory's Gulf coastline east of Borroloola on 23 March. The storm weakened as it moved inland. TC Trevor's peak 10-minute sustained winds were 94 kt (49 m s^{-1}), and its minimum central pressure was 950 hPa. Flooding in Queensland associated with the cyclone caused a farm to suffer loss of cattle and damage to equipment estimated to cost at least $710 000 (U.S. dollars). There was little reported in terms of major damage or injuries in the Northern Territory.

TC Ann originated from a tropical low that formed on 7 May, east of Honiara in the Solomon Islands. The low tracked slowly toward the southwest in a favorable environment, passing close to Honiara on 8 May and then moved southward, passing between the Australian cyclone region and South Pacific cyclone region three times over several days. On 11 May, the system intensified into a Category 1 TC before turning west-northwest and further strengthening over the Coral Sea. On 12 May, Ann reached peak intensity as a Category 2 TC with 10-minute sustained winds of 51 kt (26 m s^{-1}) and a central barometric pressure of 993 hPa. TC Ann weakened to a gale-force tropical low on 14 May and made landfall near Lockhart River on Cape York Peninsula on 15 May. The system continued to track west-northwest for several days and dissipated as a tropical low near East Timor on 18 May. Impacts associated with TC Ann were relatively minor, with heavy rainfall and gusts experienced in many areas south of where the system made landfall as a tropical low.

g. Tropical cyclone heat potential—R. Domingues, G. J. Goni, J. A. Knaff, I-I Lin, and F. Bringas

Upper-ocean thermal conditions observed during 2019 within the seven tropical cyclone (TC) basins are described here with respect to the long-term mean (1993–2018) and to conditions observed in 2018. The analysis focuses on vertically integrated temperature conditions based on the Tropical Cyclone Heat Potential (TCHP; e.g., Goni et al. 2009, 2017) which is calculated as the integrated heat content between the sea surface and the depth of the 26°C isotherm (the minimum temperature required for genesis and intensification, Leipper and Volgenau 1972; Dare and McBride 2011). The TCHP is an indicator of the amount of heat stored in the upper ocean and available to fuel TC intensification and modulates TC-induced sea surface temperature (SST) cooling and ocean–hurricane enthalpy fluxes (e.g., Lin et al. 2013). Areas in the ocean with TCHP values above 50 kJ cm^{-2} have been associated with TC intensification and rapid intensification (e.g., Shay et al. 2000; Mainelli et al. 2008; Lin et al. 2014; Knaff et al. 2018), provided that atmospheric conditions are also favorable. Salinity in the upper layers also modulates upper-ocean turbulent mixing and, thus, can also impact the depth of the 26°C isotherm and the corresponding TCHP values (e.g., Balaguru et al. 2015; Domingues et al. 2015).

Unauthenticated | Downloaded 12/18/20 02:55 PM UTC

The analysis developed here focuses primarily on seasonal TCHP anomalies (Fig. 4.36) calculated as departures from the long-term mean (1993–2019) for the primary months of TC activity in each hemisphere: June–November 2019 in the Northern Hemisphere (NH) and November 2018–April 2019 in the Southern Hemisphere (SH). Differences between the 2019 and 2018 seasons are also analyzed (Fig. 4.37). In any given TC basin, TCHP anomalies can exhibit large spatial and temporal variability linked with large mesoscale ocean features, and short-term, interannual (e.g., El Niño-Southern Oscillation [ENSO]), and longer-term ocean variability, such as the Pacific Decadal Variability.

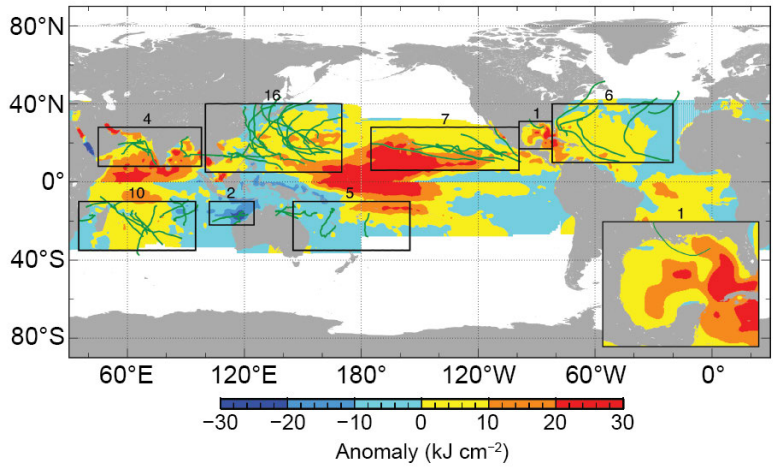

Fig. 4.36. Global anomalies of TCHP during 2019 computed as described in the text. Boxes indicate the seven regions where TCs occur: from left to right, Southwest Indian, North Indian, West North Pacific, Southeast Indian, South Pacific, East Pacific, and North Atlantic (shown as Gulf of Mexico and tropical Atlantic separately). The green lines indicate the trajectories of all TCs reaching at least Category-1 (1-min average wind ≥ 64 kts, 34 m s^{-1}) and above during Nov 2018–Apr 2019 in the SH and Jun–Nov 2019 in the NH. The numbers above each box correspond to the number of Category-1 and above cyclones that travel within each box. The Gulf of Mexico conditions are shown in the inset in the lower right corner.

The 2019 TC season exhibited above-normal TCHP anomalies, which are favorable for TC development and intensification, in most TC basins (Fig. 4.36). TCHP values also increased in most basins from 2018 to 2019 (Fig. 4.37), with notable warming of 20 kJ cm^{-2} with respect to 2018 observed at: (1) portions of the Gulf of Mexico associated with Loop Current dynamics; (2) large areas in the South and North Indian Ocean basins; and (3) the western North Pacific basin Main Development Region (MDR; Lin et al. 2014), i.e., east of the Philippines between 5°N and 20°N, and 100°–170°E. Negative TCHP anomalies with respect to long-term conditions (Fig. 4.36) and the 2018 season (Fig. 4.37) were only observed in the southeast Indian basin and near the eastern portion of the South Pacific basin.

Both the North and southwest Indian Ocean basins exhibited considerably large TCHP values in 2019 (Fig. 4.36), with anomalies as large as ~30 kJ cm^{-2} larger than the long-term average in most of the North Indian basin, including the Bay of Bengal and Arabian Sea; and ~20 kJ cm^{-2} in the southeast Indian basin. In particular, TCHP values were consistently larger than 90 kJ cm^{-2} in the North Indian basin and 70 kJ cm^{-2} in the southeast basin (not shown). Consistent with these substantially warmer conditions, both the North and southwest Indian basins were characterized by above-normal TC activity. In the North Indian basin, the 2019 TC season was one of the most active on record (see section 4f5; Fig. 4.36). In the southwest Indian basin, the 2019 TC season was the most active, costliest, and deadliest on record (see section 4f6).

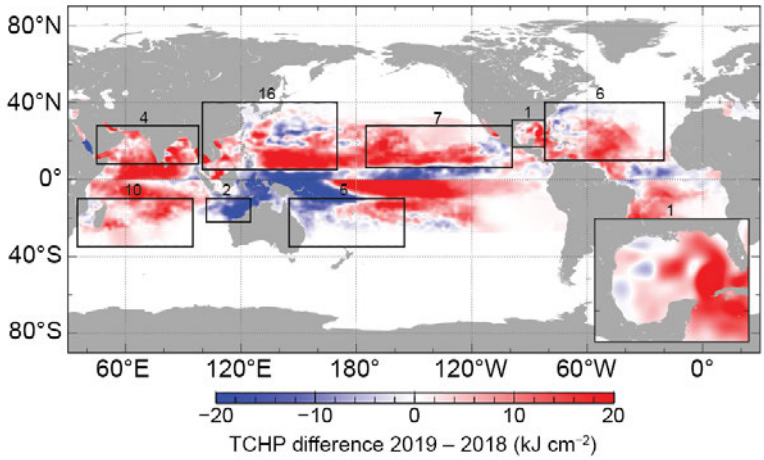

Fig. 4.37. TCHP difference between the 2019 and 2018 tropical cyclone seasons (Jun–Nov in the NH and Nov–Apr in the SH).

In the North Pacific, upper-ocean thermal conditions are largely modulated by the state of ENSO (e.g., Lin et al. 2014, 2020; Zheng et al. 2015), which can impact conditions both in the western and eastern North Pacific basins. During

Unauthenticated | Downloaded 12/18/20 02:55 PM UTC

the 2019 TC season, ENSO conditions switched from neutral in late 2018 to a weak El Niño in early 2019 and back to neutral conditions by mid-2019. Associated with the neutral ENSO state, the MDR within the western North Pacific basin exhibited TCHP values approximately 10–20 kJ cm^{-2} larger than the long-term mean (Fig. 4.36) and ~20 kJ cm^{-2} larger than 2018 conditions (Fig. 4.37). These anomalies led to absolute TCHP values of 120 kJ cm^{-2} or larger over the MDR and of at least 70 kJ cm^{-2} over most of this basin. Among the TCs that formed in this basin, Super Typhoon Hagibis was a notable TC that experienced rapid intensification while traveling over areas with TCHP of 100 kJ cm^{-2} or larger, where it became Category 5 (not shown). Another notable case is Super Typhoon Halong, which also rapidly intensified over the MDR in areas with large TCHP values (~100 kJ cm^{-2}) in November, reaching a maximum wind speed of 155 kts (80 m s^{-1}). Halong was the most intense TC globally in 2019, but fortunately did not make landfall.

In the eastern North Pacific basin, TCHP values were consistently larger than long-term average conditions by 10–30 kJ cm^{-2} (Fig. 4.36). Compared to 2018 conditions, TCHP values were ~20 kJ cm^{-2} larger in 2019 over the central part of the basin between 180°W and 120°W and slightly cooler by less than 10 kJ cm^{-2} closer to Central America. Of note, Major Hurricane Erick's rapid intensification west of 140°E was aided by the higher TCHP in this region.

Finally, in the North Atlantic basin, TCHP values were ~10 kJ cm^{-2} above the long-term average (Fig. 4.36) in most parts of the basin, and warmer than 2018 in the central part of the basin between 60°W and 30°W and in the Gulf of Mexico, where the Loop Current extended northward and shed a warm core ring. Associated with these conditions, the North Atlantic basin exhibited above-normal hurricane activity for the fourth consecutive year. Higher TCHP values over the central portion of the basin likely contributed to the rapid intensification of five of the total six hurricanes that developed in that region of the North Atlantic in 2019 (Fig. 4.36). Hurricane Dorian, now regarded as the most powerful hurricane on record for the Atlantic outside of the tropics (>23.5°N) in the satellite era (since 1966), reached its peak intensity while traveling over areas with TCHP values consistently above 70 kJ cm^{-2} and as large as 90 kJ cm^{-2} (not shown). These conditions are well above the 50 kJ cm^{-2} minimum threshold required to support Atlantic hurricane intensification (Mainelli et al. 2008). In addition to high TCHP values, Dorian traveled and intensified over areas with low surface salinity values associated with the Amazon and Orinoco riverine plumes (not shown). Areas with this type of low surface salinity are known for favoring TC intensification by creating barrier layer conditions that suppress upper-ocean mixing, maintaining enthalpy fluxes from the ocean into the hurricane (e.g., Balaguru et al. 2015; Domingues et al. 2015).

In summary, upper-ocean conditions conducive for TC development and intensification observed in 2019 were associated with higher-than-normal values of TCHP in most TC basins in 2019. Notable warming with respect to 2018 was also recorded in most basins, especially in the Gulf of Mexico, the west North Pacific, and the Indian Ocean, particularly the Arabian Sea. These warmer-than-usual conditions contributed to the more intense and above-normal TC activity in most of these basins.

h. Indian Ocean dipole—L. Chen, J.-J. Luo, and A.D. Magee

The Indian Ocean dipole (IOD) is an inherent air–sea coupling mode in the tropical Indian Ocean. It originates from local air–sea interaction in the Indian Ocean and/or the forcing associated with the El Niño–Southern Oscillation (ENSO) in the tropical Pacific (Saji et al. 1999; Luo et al. 2010). Typically, IOD events develop in boreal summer, peak in boreal autumn, and terminate rapidly in early boreal winter. During the late boreal spring to autumn 2019, a positive IOD (pIOD) with extreme intensity occurred for the first time since 1997. Prior to the pIOD event in 1997, the previous extreme pIOD event occurred in 1994 (Luo et al. 2007, 2008).

In the tropical Pacific, a weak El Niño occurred in the boreal winter of 2018/19 and returned to neutral conditions by the boreal summer of 2019, but the sea surface anomalously warmed there during the autumn of 2019 (Fig. 4.38c). In the tropical Indian Ocean, a weak pIOD occurred during

Unauthenticated | Downloaded 12/18/20 02:55 PM UTC

the autumn of 2018 but rapidly deteriorated early in the winter of 2018/19 (Figs. 4.38a,b; Chen and Luo 2019). For the first four months of 2019 (Figs. 4.38 a,b), IOD-related sea surface temperature (SST) anomalies were near zero. Meanwhile, weak surface easterly wind anomalies prevailed over the central equatorial Indian Ocean during the boreal winter of 2018/19 (partly due to the remote influence of the weak El Niño). These anomalies weakened to near zero in March–April 2019 (Fig. 4.38b). Both pIOD-related SST anomalies (SSTA) and easterly wind anomalies started to grow sharply beginning in May 2019 (Fig. 4.38b). The initial SSTA in the southeastern Indian Ocean exhibited cooling along the south coast of Java in May 2019, and then the cooling signal gradually strengthened and expanded toward the west coast of Sumatra and eastern equatorial Indian Ocean (Figs. 4.39b–d). The positive SSTA in the western equatorial Indian Ocean can be traced back to the persistent warming SSTA associated with the Indian Ocean basin mode throughout the late 2018/19 boreal winter and early 2019 spring (Figs. 4.39a,b). Then the anomalously warm SSTA in the western Indian Ocean maintained its intensity throughout June–October 2019 (Figs. 4.38a, 4.39c,d). The negative SSTA in the eastern pole started to grow from May and continued to increase quickly until October (Figs. 4.38a, 4.39b–d).

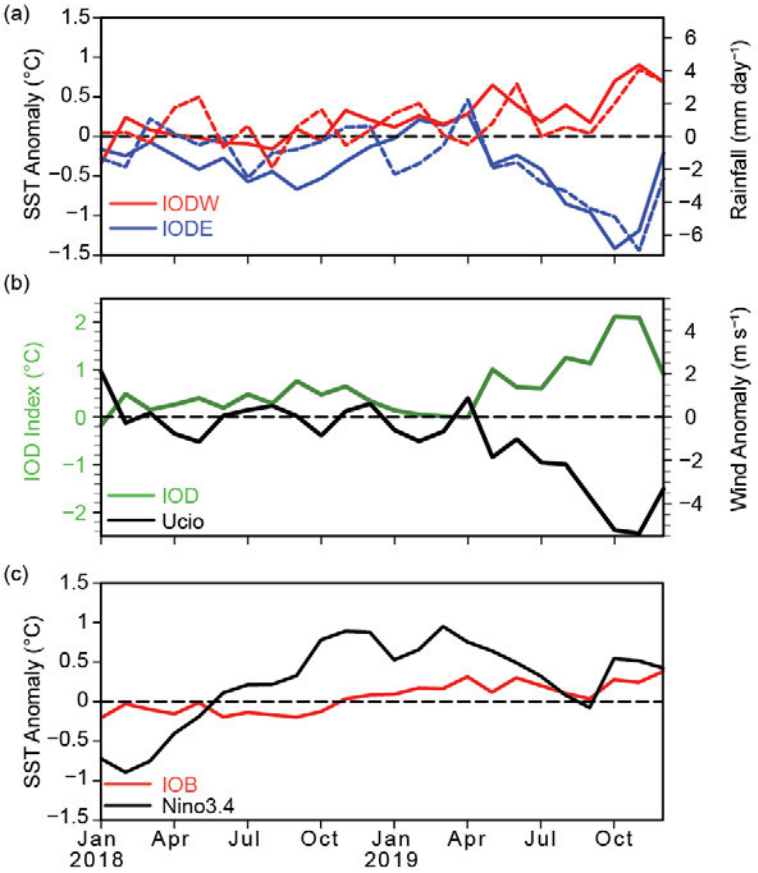

Fig. 4.38. (a) Monthly anomalies of SST (°C; solid lines) and precipitation (mm day^{-1}; dashed lines) in the eastern pole (IODE; 0°–10°S, 90°–110°E; blue lines) and the western pole (IODW; 10°N–10°S, 50°–70°E; red lines) of the IOD. (b) As in (a), but for the IOD index (measured by the SST difference between IODW and IODE, green line) and surface zonal wind anomaly (m s^{-1}) in the central equatorial IO (Ucio; 5°N–5°S, 70°–90°E; black line). (c) As in (a), but for the SST anomalies in the Niño-3.4 region (5°N–5°S, 170°–120°W; black line) and the tropical IO (IOB; 10°N–20°S, 40°–120°E; red line). Anomalies are relative to 1982–2019. (Sources: NOAA OISST [Reynolds et al. 2002]; GPCP precipitation [Huffman et al. 2009]; and JRA-55 atmospheric reanalysis [Ebita et al. 2011].)

Since the pIOD started to grow in May, positive precipitation anomalies developed near the western pole with dry anomalies near the eastern pole (Fig. 4.38a). This pattern indicates that the precipitation anomalies in the equatorial Indian Ocean were well coupled with the easterly wind anomalies in the central equatorial Indian Ocean and SSTA throughout the development of this pIOD event. Before the development of the IOD-related SSTA, a positive precipitation anomaly occurred near the eastern pole of the IOD in April (Fig. 4.38a), which might be associated with atmospheric high-frequency "noise." This positive precipitation near the eastern pole may have played a role in inducing the initial southeasterly wind anomaly along the south coast of Java and southwest coast of Sumatra in April, which caused the positive Bjerknes feedback (Bjerknes 1969) over the following months, ultimately leading to the pIOD event.

The pIOD in 2019, whose Dipole Mode Index (DMI) attained ~2.1°C in October 2019, exhibited the greatest magnitude in the observational record since 1997 (Fig. 4.40c). The surface zonal wind anomaly in the central equatorial Indian Ocean related to the pIOD in 2019 ranked only second to the extraordinary pIOD event in 1997 (Fig. 4.40d). In contrast to the extreme pIOD in 1997 that occurred with an extremely strong El Niño, the 2019 pIOD event was accompanied by a

Unauthenticated | Downloaded 12/18/20 02:55 PM UTC

neutral ENSO state in the tropical Pacific (Fig. 4.40e). There is no clear evidence supporting that remote processes in the tropical Pacific played an essential role in generating the pIOD event in 2019. Rather, it appears that the development of this extreme pIOD event was largely generated by local processes in the Indian Ocean. This is different from the majority of pIOD events, which have often co-occurred with El Niño events (e.g., 6 out of 10 past pIOD events since 1980 co-occurred with El Niño, as shown in Fig. 4.40). It is also worth noting that the positive SSTA in the western pole reached ~0.8°C and the negative SSTA in the eastern pole reached ~ −1.3°C in late autumn of 2019 (Figs. 4.40a,b). The former ranked first among all historical pIOD events, which may be traced back to the continuous enhancement of tropical Indian Ocean warming during recent decades (Luo et al. 2012).

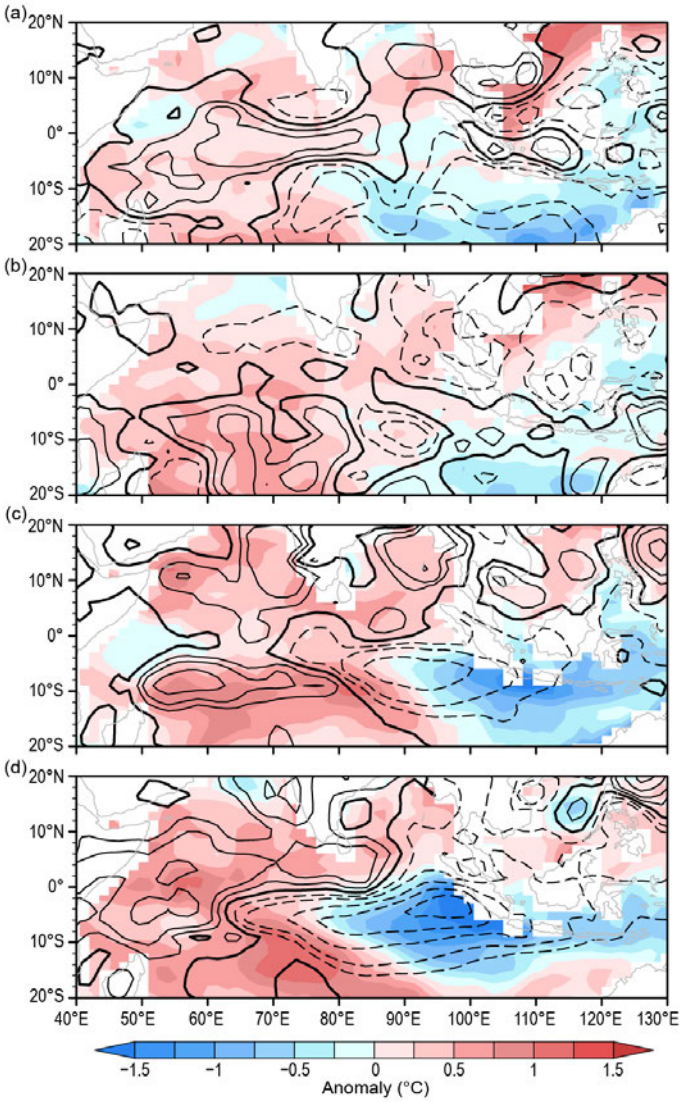

Fig. 4.39. SST (°C; colored scale) and precipitation (contours: −8, −6, −4, −2, −1, 0, 1, 2, 4, 6 mm day^{-1}; solid/dashed/bold curves denote positive/negative/zero values) anomalies during (a) Dec 2018–Feb 2019, (b) Mar–May 2019, (c) Jun–Aug 2019, and (d) Sep–Nov 2019. Anomalies are relative to 1982–2019. (Sources: NOAA OISST [Reynolds et al. 2002]; GPCP precipitation analysis [Huffman et al. 2009].)

Impacts associated with this strong pIOD event were widespread and preconditioned a number of events across the globe. In Australia, the austral spring of 2019 was the driest on record, and along with a particularly dry austral winter, fueled an unusually early start to the bushfire season (see section 7h4 and Sidebar 7.6 for details). Fires continued to burn into early 2020. This strong pIOD event resulted in significant flooding in eastern Africa, with some regions in the Horn of Africa seeing up to 300% above-average rainfall between October and mid-November, ranking among the wettest rainfall seasons in east Africa in at least 40 years. Approximately 300 people died, and a further 3.4 million people were affected across the region (Famine Early Warning Systems Network 2020). The strong pIOD has also been associated with the ongoing drought and smoke haze in Indonesia.

In summary, the strongest pIOD event since 1997 occurred in October 2019. During the course of the growth of this pIOD event, equatorial zonal wind, precipitation, and SST anomalies in the equatorial Indian Ocean all coupled well with each other. As shown in Fig. 4.40f, in April–May, low-level southeasterly anomalies prevailed near the south coasts of Java and Sumatra, and the negative SSTA near the eastern pole started to grow rapidly. Concurrently, weak, warm SSTA persisted near the western pole (which may be associated with the prolonged Indian Ocean basin warming during early 2019). As a result, low-level easterly wind anomalies started to grow in the central equatorial Indian Ocean in May. Through the positive Bjerknes feedback, the pIOD event was generated, and the corresponding anomaly signal peaked during the autumn of 2019. In December, the IOD-related SST, precipitation, and wind anomalies quickly deteriorated. The extreme pIOD event in 2019 seems to have originated from air–sea feedback processes in the

Unauthenticated | Downloaded 12/18/20 02:55 PM UTC

Indian Ocean itself, rather than being induced by the remote influence of El Niño. Interestingly, such a unique development feature of the pIOD in 2019 differs from many of the past pIOD events that co-occurred with El Niño events.

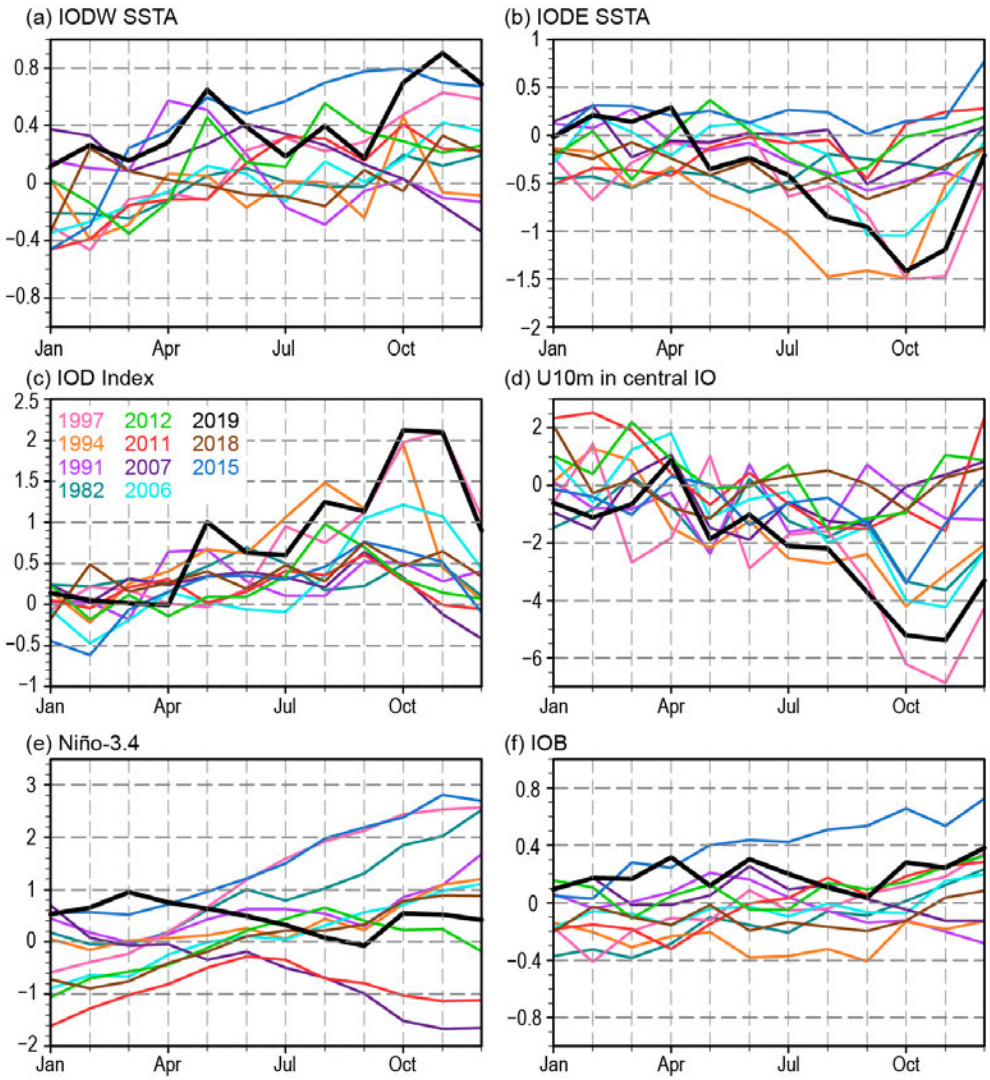

Fig. 4.40. Monthly SST anomalies in the (a) IODW, (b) IODE, and (c) the Dipole Mode Index (DMI, the SST anomaly difference between the IODW and the IODE) during 11 pIOD events since the 1980s. (d) As in (c) but for the surface zonal wind anomaly ($m\,s^{-1}$) in the central equatorial Indian Ocean (70°–90°E; 5°N–5°S). (e)–(f) As in (a)–(b), but for the monthly SST anomalies in the Niño-3.4 region (170°–120°W; 5°N–5°S) and the tropical Indian Ocean basin (40°–120°E; 20°N–20°S). (Sources: NOAA OISST [Reynolds et al. 2002]; GPCP precipitation [Huffman et al. 2009]; and JRA-55 atmospheric reanalysis [Ebita et al. 2011].)

Unauthenticated | Downloaded 12/18/20 02:55 PM UTC

APPENDIX: Acronym List

ACE	Accumulated Cyclone Energy
AEJ	African Easterly Jet
AMO	Atlantic Multidecadal Oscillation
ASO	August-October
CMORPH	Climate Prediction Center morphing method
CNP	central North Pacific
CPC	Climate Prediction Center
DJF	December-February
DMI	Dipole Mode Index
ENP	eastern North Pacific
ENSO	El Niño-Southern Oscillation
GPI	genesis potential index
HTC	hurricanes/typhoons/cyclones
HURDAT2	(National Hurricane Center's) Hurricane Database
IBTrACS	International Best Track Archive for Climate Stewardship
IOD	Indian Ocean dipole
ITCZ	Intertropical Convergence Zone
JAS	July-September
JASO	July-October
JFM	January-March
JJA	June-August
JMA	Japan Meteorological Agency
JTWC	Joint Typhoon Warning Center
MAM	March-May
MDR	Main Development Region
MJJ	May-July
MJO	Madden Julian Oscillation
NDJ	November-January
NH	Northern Hemisphere
NIO	North Indian Ocean
OLR	Outgoing Longwave Radiation
OND	October-December
ONI	Oceanic Niño Index
PAGASA	Philippine Atmospheric, Geophysical and Astronomical Services Administration
pIOD	positive Indian Ocean dipole
RMM	Real-time Multivariate MJO
RMSCs	Regional Specialized Meteorological Centers
SAM	Southern Annular Mode
SH	Southern Hemisphere
SIO	South Indian Ocean
SON	September-November
SPCZ	South Pacific Convergence Zone
SPEArTC	Southwest Pacific Enhanced Archive of Tropical Cyclones
SSHWS	Saffir-Simpson
SSHWS	Saffir-Simpson Hurricane Wind Scale
SST	sea surface temperature

Unauthenticated | Downloaded 12/18/20 02:55 PM UTC

TC	tropical cyclone
TCHP	Tropical Cyclone Heat Potential
TD	tropical depression
TS	tropical storm
TWS	trade wind surges
WMO	World Meteorological Organization
WNP	western North Pacific
WWBs	westerly wind bursts

Unauthenticated | Downloaded 12/18/20 02:55 PM UTC

References

Aiyyer, A., and J. Molinari, 2008: MJO and tropical cyclogenesis in the Gulf of Mexico and eastern Pacific: Case study and idealized numerical modeling. *J. Atmos. Sci.*, **65**, 2691–2704, https://doi.org/10.1175/2007JAS2348.1.

Avila, L. A., 2019: Hurricane Lorena. National Hurricane Center Tropical Cyclone Rep., 20 pp., www.nhc.noaa.gov/data/tcr/EP152019_Lorena.pdf.

——, S. A. Stewart, R. Berg, and A. B. Hagen, 2020: Hurricane Dorian. National Hurricane Center Tropical Cyclone Rep., 74 pp., www.nhc.noaa.gov/data/tcr/AL052019_Dorian.pdf.

Balaguru, K., G. R. Foltz, L. R. Leung, E. A. D'Asaro, K. A. Emanuel, H. Liu, and S. E. Zedle, 2015: Dynamic potential intensity: An improved representation of the ocean's impact on tropical cyclones. *Geophys. Res. Lett.*, **42**, 6739–6746, https://doi.org/10.1002/2015GL064822.

Banzon, V. F., and R. W. Reynolds, 2013: Use of WindSat to extend a microwave-based daily optimum interpolation sea surface temperature time series. *J. Climate*, **26**, 2557–2562, https://doi.org/10.1175/JCLI-D-12-00628.1.

Baxter, S., S. Weaver, J. Gottschalck, and Y. Xue, 2014: Pentad evolution of wintertime impacts of the Madden–Julian Oscillation over the contiguous United States. *J. Climate*, **27**, 7356–7367, https://doi.org/10.1175/JCLI-D-14-00105.1.

——, C. Schreck, and G. D. Bell, 2019: ttTropical intraseasonal activity [in "State of the Climate in 2018"]. *Bull. Amer. Meteor. Soc.*, **100** (9), S105–S107, https://doi.org/10.1175/2019BAMSStateoftheClimate.1.

Behringer, D. W., M. Ji, and A. Leetmaa, 1998: An improved coupled model for ENSO prediction and implications for ocean initialization. Part I: The ocean data assimilation system. *Mon. Wea. Rev.*, **126**, 1013–1021, https://doi.org/10.1175/1520-0493(1998)126<1013:AICMFE>2.0.CO;2.

Bell, G. D., and M. Chelliah, 2006: Leading tropical modes associated with interannual and multi-decadal fluctuations in North Atlantic hurricane activity. *J. Climate*, **19**, 590–612, https://doi.org/10.1175/JCLI3659.1.

,*Bull. Amer. Meteor. Soc.***100**——, and Coauthors, 2000: The 1999 North Atlantic hurricane season: A climate perspective [in "State of the Climate in 1999"]. *Bull. Amer. Meteor. Soc.*, **81** (6), S1–S68, https://doi.org/10.1175/1520-0477(2000)81[s1:CAF]2.0.CO;2.

——, and Coauthors, 2004: The 2003 North Atlantic Hurricane Season: A climate perspective [in "State of the Climate in 2003"]. *Bull. Amer. Meteor. Soc.*, **85** (6), S1–S68, https://doi.org/10.1175/1520-0477-85.6s.S1.

——, and Coauthors, 2006: The 2005 North Atlantic Hurricane Season: A climate perspective [in "State of the Climate in 2005"]. *Bull. Amer. Meteor. Soc.*, **86** (6), S1–S68, https://doi.org/10.1175/1520-0477-87.6.S1.

——, and Coauthors, 2017: [The tropics] the 2016 North Atlantic hurricane season: A climate perspective [in "State of the Climate in 2016"]. *Bull. Amer. Meteor. Soc.*, **98** (8), S109–S112, https://doi.org/10.1175/2017BAMSStateoftheClimate.1.

——, and Coauthors, 2018: [The tropics] the 2017 North Atlantic hurricane season: A climate perspective [in "State of the Climate in 2017"]. *Bull. Amer. Meteor. Soc.*, **99** (8), S114–S118, https://doi.org/10.1175/2018BAMSStateoftheClimate.1.

——, M. S. Halpert, and M. L'Heureux, 2019: ENSO and the tropical Pacific [in "State of the Climate in 2018"]. *Bull. Amer. Meteor. Soc.*, **100** (9), S101–S104, https://doi.org/10.1175/2019BAMSStateoftheClimate.1.

Bjerknes, J., 1969: Atmospheric teleconnections from the equatorial Pacific. *Mon. Wea. Rev.*, **97**, 163–172, https://doi.org/10.1175/1520-0493(1969)097<0163:ATFTEP>2.3.CO;2.

Blake, E. S., 2019: Tropical Storm Narda. National Hurricane Center Tropical Cyclone Rep., 14 pp., www.nhc.noaa.gov/data/tcr/EP162019_Narda.pdf.

Camargo, S. J., K. A. Emanuel, and A. H. Sobel, 2007: Use of a genesis potential index to diagnose ENSO effects on tropical cyclone genesis. *J. Climate*, **20**, 4819–4834, https://doi.org/10.1175/JCLI4282.1.

Cassou, C., 2008: Intraseasonal interaction between the Madden Julian oscillation and the North Atlantic oscillation. *Nature*, **455**, 523–527. Letter, https://doi.org/10.1038/nature07286.

Chen, L., and J.-J. Luo, 2019: Indian Ocean dipole [in "State of the Climate in 2018"]. *Bull. Amer. Meteor. Soc.*, **100** (9), S138–S140, https://doi.org/10.1175/2019BAMSStateoftheClimate.1.

Chia, H. H., and C. F. Ropelewski, 2002: The interannual variability in the genesis location of tropical cyclones in the northwest Pacific. *J. Climate*, **15**, 2934–2944, https://doi.org/10.1175/1520-0442(2002)015<2934:TIVITG>2.0.CO;2.

CDare, R. A., and J. L. McBride, 2011: Sea surface temperature response to tropical cyclones. *Mon. Wea. Rev.*, **139**, 3798–3808, https://doi.org/10.1175/MWR-D-10-05019.1.

Diamond, H. J., and J. A. Renwick, 2015: The climatological relationship between tropical cyclones in the southwest Pacific and the Madden–Julian Oscillation. *Int. J. Climatol.*, **35**, 676–686, https://doi.org/10.1002/joc.4012.

——, and C. J. Schreck III, Eds, 2017: The tropics [in "State of the Climate in 2016"]. *Bull. Amer. Meteor. Soc.*, **98** (8), S93–S128, https://doi.org/10.1175/2017BAMSStateoftheClimate.1..

——, and ——, Eds, 2018: The tropics [in "State of the Climate in 2017"]. *Bull. Amer. Meteor. Soc.*, **99** (8), S101–S141, https://doi.org/10.1175/2018BAMSStateoftheClimate.1..

——, and ——, Eds, 2019: The tropics [in "State of the Climate in 2018"]. *Bull. Amer. Meteor. Soc.*, **100** (9), S101–S140, https://doi.org/10.1175/2019BAMSStateoftheClimate.1..

——, A. M. Lorrey, K. R. Knapp, and D. H. Levinson, 2012: Development of an enhanced tropical cyclone tracks database for the southwest Pacific from 1840 to 2011. *Int. J. Climatol.*, **32**, 2240–2250, https://doi.org/10.1002/joc.2412.

Domingues, R., G. Goni, F. Bringas, G. Halliwell, S.-K. Lee, H.-S. Kim, J. Morell, and J. Dong, 2015: Upper ocean response to Hurricane Gonzalo (2014): Results from unique observations by underwater gliders. *Geophys. Res. Lett.*, **42**, 7131–7138, https://doi.org/10.1002/2015GL065378.

Dube, S. K., D. Rao, P. C. Sinha, T. S. Murty, and N. Bahuluyan, 1997: Storm surge in the Bay of Bengal and Arabian Sea: The problem and its prediction. *Mausam*, **48**, 288–304.

Ebita, A., and Coauthors, 2011: The Japanese 55-year reanalysis "JRA-55": An interim report. *SOLA*, **7**, 149–152, https://doi.org/10.2151/SOLA.2011-038.

Emanuel, K. A., and D. S. Nolan, 2004: Tropical cyclone activity and the global climate system. Proc. 26th Conf. on Hurricanes and Tropical Meteorology, Miami, FL, Amer. Meteor. Soc., 10A.2, https://ams.confex.com/ams/26HURR/techprogram/paper_75463.htm.

Enfield, D. B., and A. M. Mestas-Nuñez, 1999: Multiscale variabilities in global sea surface temperatures and their relationships with tropospheric climate patterns. *J. Climate*, **12**, 2719–2733, https://doi.org/10.1175/1520-0442(1999)012<2719:MVIGSS>2.0.CO;2.

Famine Early Warning Systems Network, 2020: 2019 short rains in East Africa among the wettest on historical record,. FEWS NET, , https://fews.net/east-africa/special-report/january-29-2020.

Frank, W. M., and P. E. Roundy, 2006: The role of tropical waves in tropical cyclogenesis. *Mon. Wea. Rev.*, **134**, 2397–2417, https://doi.org/10.1175/MWR3204.1.

Goldenberg, S. B., and L. J. Shapiro, 1996: Physical mechanisms for the association of El Niño and West African rainfall with Atlantic major hurricane activity. *J. Climate*, **9**, 1169–1187, https://doi.org/10.1175/1520-0442(1996)009<1169:PMFTAO>2.0.CO;2.

——, C. W. Landsea, A. M. Mestas-Nuñez, and W. M. Gray, 2001: The recent increase in Atlantic hurricane activity: Causes and implications. *Science*, **293**, 474–479, https://doi.org/10.1126/science.1060040.

Goni, G. J., and Coauthors, 2009: Applications of satellite-derived ocean measurements to tropical cyclone intensity forecasting. *Oceanography*, **22**, 190–197, https://doi.org/10.5670/oceanog.2009.78.

Unauthenticated | Downloaded 12/18/20 02:55 PM UTC

——, and Coauthors, 2017: Autonomous and Lagrangian Ocean observations for Atlantic tropical cyclone studies and forecasts. *Oceanography*, **30**, 92–103, https://doi.org/10.5670/oceanog.2017.227.

Gray, W. M., 1990: Strong association between West African rainfall and U.S. landfall of intense hurricanes. *Science*, **249**, 1251–1256, https://doi.org/10.1126/science.249.4974.1251.

Guo, Y., X. Jiang, and D. E. Waliser, 2014: Modulation of the convectively coupled Kelvin waves over South America and the tropical Atlantic Ocean in association with the Madden–Julian oscillation. *J. Atmos. Sci.*, **71**, 1371–1388, https://doi.org/10.1175/JAS-D-13-0215.1.

Halpert, M. S., and C. F. Ropelewski, 1992: Surface temperature patterns associated with the southern oscillation. *J. Climate*, **5**, 577–593, https://doi.org/10.1175/1520-0442(1992)005<0577:STPAWT>2.0.CO;2.

Hastenrath, S., 1990: Decadal-scale changes of the circulation in the tropical Atlantic sector associated with Sahel drought. *Int. J. Climatol.*, **10**, 459–472, https://doi.org/10.1002/joc.3370100504.

Hendon, H., C. Zhang, and J. Glick, 1999: Interannual variation of the Madden–Julian oscillation during austral summer. *J. Climate*, **12**, 2538–2550, https://doi.org/10.1175/1520-0442(1999)012<2538:IVOTMJ>2.0.CO;2.

Huang, B., and Coauthors, 2017: Extended Reconstructed Sea Surface Temperature, version 5 (ERSSTv5): Upgrades, validations, and intercomparisons. *J. Climate*, **30**, 8179–8205, https://doi.org/10.1175/JCLI-D-16-0836.1.

Huffman, G. J., R. F. Adler, D. T. Bolvin, and G. Gu, 2009: Improving the global precipitation record: GPCP version 2.1. *Geophys. Res. Lett.*, **36**, L17808, , https://doi.org/10.1029/2009GL040000.

India Meteorological Department, 2020: Statement on climate of India during 2019. India Meteorological Department Climate Research and Services.A, accessed 14 January 2020, https://mausam.imd.gov.in/backend/assets/press_release_pdf/Statement_on_Climate_of_India_during_2019.pdf.

Joyce, R. J., J. E. Janowiak, P. A. Arkin, and P. Xie, 2004: CMORPH: A method that produces global precipitation estimates from passive microwave and infrared data at high spatial and temporal resolution. *J. Hydrometeor.*, **5**, 487–503, https://doi.org/10.1175/1525-7541(2004)005<0487:CAMTPG>2.0.CO;2.

Kalnay, E., and Coauthors, 1996: The NCEP/NCAR 40-Year Reanalysis Project. *Bull. Amer. Meteor. Soc.*, **77**, 437–471, https://doi.org/10.1175/1520-0477(1996)077<0437:TNYRP>2.0.CO;2.

Kayano, M., and V. Kousky, 1999: Intraseasonal (30-60 day) variability in the global tropics: Principal modes and their evolution. *Tellus*, **51A**, 373–386, https://doi.org/10.3402/tellusa.v51i3.13459.

Kiladis, G. N., and K. M. Weickmann, 1992: Circulation anomalies associated with tropical convection during northern winter. *Mon. Wea. Rev.*, **120**, 1900–1923, https://doi.org/10.1175/1520-0493(1992)120<1900:CAAWTC>2.0.CO;2.

——, K. H. Straub, and P. T. Haertel, 2005: Zonal and vertical structure of the Madden–Julian oscillation. *J. Atmos. Sci.*, **62**, 2790–2809, https://doi.org/10.1175/JAS3520.1.

Kiladis, G. N., M. C. Wheeler, P. T. Haertel, K. H. Straub, and P. E. Roundy, 2009: Convectively coupled equatorial waves. *Rev. Geophys.*, **47**, RG2003, https://doi.org/10.1029/2008RG000266.

Klotzbach, P. J., 2010: On the Madden–Julian oscillation–Atlantic hurricane relationship. *J. Climate*, **23**, 282–293, https://doi.org/10.1175/2009JCLI2978.1.

Knaff, J. A., C. R. Sampson, and K. D. Musgrave, 2018: An operational rapid intensification prediction aid for the western North Pacific. *Wea. Forecasting*, **33**, 799–811, https://doi.org/10.1175/WAF-D-18-0012.1.

Knapp, K. R., M. C. Kruk, D. H. Levinson, H. J. Diamond, and C. J. Neumann, 2010: The International Best Track Archive for Climate Stewardship (IBTrACS): Unifying tropical cyclone data. *Bull. Amer. Meteor. Soc.*, **91**, 363–376, https://doi.org/10.1175/2009BAMS2755.1.

——, J. A. Knaff, C. R. Sampson, G. M. Riggio, and A. D. Schnapp, 2013: A pressure-based analysis of the historical western North Pacific tropical cyclone intensity record. *Mon. Wea. Rev.*, **141**, 2611–2631, https://doi.org/10.1175/MWR-D-12-00323.1.

Knutson, T. R., and K. M. Weickmann, 1987: 30–60 day atmospheric oscillations: Composite life cycles of convection and circulation anomalies. *Mon. Wea. Rev.*, **115**, 1407–1436, https://doi.org/10.1175/1520-0493(1987)115<1407:DAOCLC>2.0.CO;2.

Kousky, V. E., and M. T. Kayano, 1994: Principal modes of outgoing longwave radiation and 250-mb circulation for the South American sector. *J. Climate*, **7**, 1131–1143, https://doi.org/10.1175/1520-0442(1994)007<1131:PMOOLR>2.0.CO;2.

Krishnamurti, T. N., and D. Subrahmanyam, 1982: The 30–50 day mode at 850 mb during MONEX. *J. Atmos. Sci.*, **39**, 2088–2095, https://doi.org/10.1175/1520-0469(1982)039<2088:TDMAMD>2.0.CO;2.

Kruk, M. C., and C. J. Schreck, 2019: tEastern North Pacific basin [in "State of the Climate in 2018"]. *Bull. Amer. Meteor. Soc.*, **100** (9), S121–S124, https://doi.org/10.1175/2019BAMSStateoftheClimate.1.

Landsea, C. W., and J. L. Franklin, 2013: Atlantic hurricane database uncertainty and presentation of a New database format. *Mon. Wea. Rev.*, **141**, 3576–3592, https://doi.org/10.1175/MWR-D-12-00254.1.

——, W. M. Gray, P. W. Mielke, and K. J. Berry, 1992: Long-term variations of western Sahelian monsoon rainfall and intense U.S. landfalling hurricanes. *J. Climate*, **5**, 1528–1534, https://doi.org/10.1175/1520-0442(1992)005<1528:LTVOWS>2.0.CO;2.

——, B. A. Harper, K. Hoarau, and J. A. Knaff, 2006: Can we detect trends in extreme tropical cyclones? *Science*, **313**, 452–454, https://doi.org/10.1126/science.1128448.

—, G. A. Vecchi, L. Bengtsson, and T. R. Knutson, 2010: Impact of duration thresholds on Atlantic tropical cyclone counts. *J. Climate*, **23**, 2508–2519, https://doi.org/10.1175/2009JCLI3034.1.

Lau, W. K.-M., and D. E. Waliser, 2012: Intraseasonal Variability in the Atmosphere-Ocean Climate System. Springer, 642 pp.

Leipper, D. F., and D. Volgenau, 1972: Hurricane heat potential of the Gulf of Mexico. *J. Phys. Oceanogr.*, **2**, 218–224, https://doi.org/10.1175/1520-0485(1972)002<0218:HHPOTG>2.0.CO;2.

Liebmann, B., and C. A. Smith, 1996: Description of a complete (interpolated) outgoing longwave radiation dataset. *Bull. Amer. Meteor. Soc.*, **77**, 1275–1277, https://doi.org/10.1175/1520-0477-77.6.1274.

Lin, H., G. Brunet, and J. Derome, 2009: An observed connection between the North Atlantic oscillation and the Madden–Julian oscillation. *J. Climate*, **22**, 364–380, https://doi.org/10.1175/2008JCLI2515.1.

Lin, I.-I., and Coauthors, 2013: An ocean coupling potential intensity index for tropical cyclones. *Geophys. Res. Lett.*, **40**, 1878–1882, https://doi.org/10.1002/grl.50091.

——, I.-F. Pun, and C.-C. Lien, 2014: "Category-6" super-typhoon Haiyan in global warming hiatus: Contribution from subsurface ocean warming. *Geophys. Res. Lett.*, **41**, 8547–8553, https://doi.org/10.1002/2014GL061281.

——, and Coauthors, 2020: ENSO and tropical cyclones. *El Niño Southern Oscillation in a Changing Climate*, *Geophys. Monogr.*, Vol. 254, Amer. Geophys. Union, 377–408.

Luo, J.-J., S. Masson, S. Behera, and T. Yamagata, 2007: Experimental forecasts of the Indian Ocean dipole using a coupled OAGCM. *J. Climate*, **20**, 2178–2190, https://doi.org/10.1175/JCLI4132.1.

——, S. Behera, Y. Masumoto, H. Sakuma, and T. Yamagata, 2008: Successful prediction of the consecutive IOD in 2006 and 2007. *Geophys. Res. Lett.*, **35**, L14S02, https://doi.org/10.1029/2007GL032793.

——, R. Zhang, S. K. Behera, Y. Masumoto, F.-F. Jin, R. Lukas, and T. Yamagata, 2010: Interaction between El Niño and extreme Indian Ocean dipole. *J. Climate*, **23**, 726–742, https://doi.org/10.1175/2009JCLI3104.1.

——, W. Sasaki, and Y. Masumoto, 2012: Indian Ocean warming modulates Pacific climate change. *Proc. Natl. Acad. Sci. USA*, **109**, 18701–18706, , https://doi.org/10.1073/pnas.1210239109.

Madden, R., and P. Julian, 1971: Detection of a 40–50 day oscillation in the zonal wind in the tropical Pacific. *J. Atmos. Sci.*, **28**, 702–708, https://doi.org/10.1175/1520-0469(1971)028<0702:DOADOI>2.0.CO;2.

Unauthenticated | Downloaded 12/18/20 02:55 PM UTC

——, and ——, 1972: Description of global-scale circulation cells in the tropics with a 40–50 day period. *J. Atmos. Sci.*, **29**, 1109–1123, https://doi.org/10.1175/1520-0469(1972)029<1109:DOGSCC>2.0.CO;2.

——, and ——, 1994: Observations of the 40–50-day tropical oscillation: A review. *Mon. Wea. Rev.*, **122**, 814–837, https://doi.org/10.1175/1520-0493(1994)122<0814:OOTDTO>2.0.CO;2.

Mainelli, M., M. DeMaria, L. Shay, and G. Goni, 2008: Application of oceanic heat content estimation to operational forecasting of recent Atlantic category 5 hurricanes. *Wea. Forecasting*, **23**, 3–16, https://doi.org/10.1175/2007WAF2006111.1.

Maloney, E. D., and D. L. Hartmann, 2001: The Madden–Julian oscillation, barotropic dynamics, and North Pacific tropical cyclone formation. Part I: Observations. *J. Atmos. Sci.*, **58**, 2545–2558, https://doi.org/10.1175/1520-0469(2001)058<2545:TMJOBD>2.0.CO;2.

Masters, J., 2019: Africa's Hurricane Katrina: Tropical Cyclone Idai causes an extreme catastrophe. Weather Underground, accessed 14 January 2020, www.wunderground.com/cat6/Africas-Hurricane-Katrina-Tropical-Cyclone-Idai-Causes-Extreme-Catastrophe.

Mo, K. C., 2000: The association between intraseasonal oscillations and tropical storms in the Atlantic basin. *Mon. Wea. Rev.*, **128**, 4097–4107, https://doi.org/10.1175/1520-0493(2000)129<4097:TABIOA>2.0.CO;2.

——, and V. E. Kousky, 1993: Further analysis of the relationship between circulation anomaly patterns and tropical convection. *J. Geophys. Res.*, **98**, 5103–5113, https://doi.org/10.1029/92JD02952.

Münnich, M., and J. D. Neelin, 2005: Seasonal influence of ENSO on the Atlantic ITCZ and equatorial South America. *Geophys. Res. Lett.*, **32**, L21709, https://doi.org/10.1029/2005GL023900.

Nakazawa, T., and S. Hoshino, 2009: Intercomparison of Dvorak parameters in the tropical cyclone datasets over the western North Pacific. *SOLA*, **5**, 33–36, https://doi.org/10.2151/SOLA.2009-009.

NOAA, 2019: Synoptic discussion, November 2019., NOAA/NCEI, www.ncdc.noaa.gov/sotc/synoptic/201911#November-16-22.

Nobre, P., and J. Shukla, 1996: Variations of sea surface temperature, wind stress and rainfall over the tropical Atlantic and South America. *J. Climate*, **9**, 2464–2479, https://doi.org/10.1175/1520-0442(1996)009<2464:VOSSTW>2.0.CO;2.

PEAC, 2019: Pacific ENSO update. Pacific ENSO Applications Center, www.weather.gov/peac/update.

Pezza, A. B., and C. A. S. Coelho, 2019: The Atlantic Intertropical convergence zone [in "State of the Climate in 2018"]. *Bull. Amer. Meteor. Soc.*, **100** (9), S109–S110, https://doi.org/10.1175/2019BAMSStateoftheClimate.1.

Raga, G. B., B. Bracamontes-Ceballos, L. Farfán, and R. Romero-Centeno, 2013: Landfalling tropical cyclones on the Pacific coast of Mexico: 1850–2010. *Atmósfera*, **26**, 209–220, https://doi.org/10.1016/S0187-6236(13)71072-5.

Reynolds, R. W., N. A. Rayner, T. M. Smith, D. C. Stokes, and W. Wang, 2002: An improved in situ and satellite SST analysis for climate. *J. Climate*, **15**, 1609–1625, https://doi.org/10.1175/1520-0442(2002)015<1609:AIISAS>2.0.CO;2.

Riddle, E., M. Stoner, N. Johnson, M. L'Heureux, D. Collins, and S. Feldstein, 2012: The impact of the MJO on clusters of wintertime circulation anomalies over the North American region. *Climate Dyn.*, **40**, 1749–1766, https://doi.org/10.1007/S00382-012-1493-Y.

Ropelewski, C. F., and M. S. Halpert, 1989: Precipitation patterns associated with the high index phase of the Southern Oscillation. *J. Climate*, **2**, 268–284, https://doi.org/10.1175/1520-0442(1989)002<0268:PPAWTH>2.0.CO;2.

Saha, S., and Coauthors, 2014: The NCEP Climate Forecast System version 2. *J. Climate*, **27**, 2185–2208, https://doi.org/10.1175/JCLI-D-12-00823.1.

Saji, N. H., B. N. Goswami, P. N. Vinayachandran, and T. Yamagata, 1999: A dipole mode in the tropical Indian ocean. *Nature*, **401**, 360–363, https://doi.org/10.1038/43854.

Schneider, T., T. Bischoff, and G. H. Haug, 2014: Migrations and dynamics of the intertropical convergence zone. *Nature*, **513**, 45–53, https://doi.org/10.1038/nature13636.

Schreck, C. J., 2015: Kelvin waves and tropical cyclogenesis: A global survey. *Mon. Wea. Rev.*, **143**, 3996–4011, https://doi.org/10.1175/MWR-D-15-0111.1.

——, 2016: Convectively coupled Kelvin waves and tropical cyclogenesis in a semi-Lagrangian framework. *Mon. Wea. Rev.*, **144**, 4131–4139, https://doi.org/10.1175/MWR-D-16-0237.1.

——, and J. Molinari, 2011: Tropical cyclogenesis associated with Kelvin waves and the Madden–Julian oscillation. *Mon. Wea. Rev.*, **139**, 2723–2734, https://doi.org/10.1175/MWR-D-10-05060.1.

——, ——, and A. Aiyyer, 2012: A global view of equatorial waves and tropical cyclogenesis. *Mon. Wea. Rev.*, **140**, 774–788, https://doi.org/10.1175/MWR-D-11-00110.1.

——, J. M. Cordeira, and D. Margolin, 2013: Which MJO events affect North American temperatures? *Mon. Wea. Rev.*, **141**, 3840–3850, https://doi.org/10.1175/MWR-D-13-00118.1.

——, K. R. Knapp, and J. P. Kossin, 2014: The impact of best track discrepancies on global tropical cyclone climatologies using IBTrACS. *Mon. Wea. Rev.*, **142**, 3881–3899, https://doi.org/10.1175/MWR-D-14-00021.1.

——, H.-T. Lee, and K. R. Knapp, 2018: HIRS outgoing longwave radiation—daily climate data record: Application toward identifying tropical subseasonal variability. *Remote Sens.*, **10**, 1325, https://doi.org/10.3390/rs10091325.

Shay, L. K., G. J. Goni, and P. G. Black, 2000: Effects of a warm oceanic feature on Hurricane Opal. *Mon. Wea. Rev.*, **128**, 1366–1383, https://doi.org/10.1175/1520-0493(2000)128<1366:EOAWOF>2.0.CO;2.

Smith, T. M., R. W. Reynolds, T. C. Peterson, and J. Lawrimore, 2008: Improvements to NOAA's historical merged land–ocean surface temperature analysis (1880–2006). *J. Climate*, **21**, 2283–2296, https://doi.org/10.1175/2007JCLI2100.1.

Song, J.-J., Y. Wang, and L. Wu, 2010: Trend discrepancies among three best track data sets of western North Pacific tropical cyclones. *J. Geophys. Res.*, **115**, D12128, https://doi.org/10.1029/2009JD013058.

Stewart, S. R., 2019: Tropical Storm Priscilla. National Hurricane Center Tropical Cyclone Rep., 9 pp., www.nhc.noaa.gov/data/tcr/EP192019_Priscilla.pdf.

Vecchi, G. A., and B. J. Soden, 2007: Effect of remote sea surface temperature change on tropical cyclone potential intensity. *Nature*, **450**, 1066–1070, https://doi.org/10.1038/NATURE06423.

Ventrice, M. J., C. D. Thorncroft, and M. A. Janiga, 2012a: Atlantic tropical cyclogenesis: A three-way interaction between an African easterly wave, diurnally varying convection, and a convectively coupled atmospheric Kelvin wave. *Mon. Wea. Rev.*, **140**, 1108–1124, https://doi.org/10.1175/MWR-D-11-00122.1.

——, ——, and C. J. Schreck, 2012b: Impacts of convectively coupled Kelvin waves on environmental conditions for Atlantic tropical cyclogenesis. *Mon. Wea. Rev.*, **140**, 2198–2214, https://doi.org/10.1175/MWR-D-11-00305.1.

Villarini, G., G. A. Vecchi, T. R. Knutson, and J. A. Smith, 2011: Is the recorded increase in short duration North Atlantic tropical storms spurious? *J. Geophys. Res.*, **116**, D10114, https://doi.org/10.1029/2010JD015493.

Vincent, D. G., 1994: The South Pacific Convergence Zone (SPCZ): A review. *Mon. Wea. Rev.*, **122**, 1949–1970, https://doi.org/10.1175/1520-0493(1994)122<1949:TSPCZA>2.0.CO;2.

Waliser, D. E., and C. Gautier, 1993: A satellite-derived climatology of the ITCZ. *J. Climate*, **6**, 2162–2174, https://doi.org/10.1175/1520-0442(1993)006<2162:ASDCOT>2.0.CO;2.

Wang, B., and Q. Ding, 2008: Global monsoon: Dominant mode of annual variation in the tropics. *Dyn. Atmos. Ocean*, **44**, 165–183, https://doi.org/10.1016/J.DYNATMOCE.2007.05.002.

——, J. Liu, H. J. Kim, P. J. Webster, and S. Y. Yim, 2012: Recent change of the global monsoon precipitation (1979–2008). *Climate Dyn.*, **39**, 1123–1135, https://doi.org/10.1007/s00382-011-1266-z.

Unauthenticated | Downloaded 12/18/20 02:55 PM UTC

Wheeler, M., and G. N. Kiladis, 1999: Convectively coupled equatorial waves: Analysis of clouds and temperature in the wavenumber-frequency domain. *J. Atmos. Sci.*, **56**, 374–399, https://doi.org/10.1175/1520-0469(1999)056<0374:CCEWAO>2.0.CO;2.

——, and H. H. Hendon, 2004: An all-season real-time multivariate MJO index: Development of an index for monitoring and prediction. *Mon. Wea. Rev.*, **132**, 1917–1932, https://doi.org/10.1175/1520-0493(2004)132<1917:AARMMI>2.0.CO;2.

Wood, K. M., and E. A. Ritchie, 2015: A definition for rapid weakening in the North Atlantic and eastern North Pacific. *Geophys. Res. Lett.*, **42**, 10 091–10 097, https://doi.org/10.1002/2015GL066697.

——, P. J. Klotzbach, J. M. Collins, and C. J. Schreck, 2019: The record-setting 2018 eastern North Pacific hurricane season. *Geophys. Res. Lett.*, **46**, 10 072–10 081, https://doi.org/10.1029/2019GL083657.

——, ——, ——, L.-P. Caron, R. E. Truchelut, and C. J. Schreck III, 2020: Factors affecting the 2019 Atlantic hurricane season and the role of the Indian Ocean Dipole. *Geophys. Res. Lett.*, **47**, e2020GL087781, https://doi.org/10.1029/2020GL087781.

Wu, M.-C., K.-H. Yeung, and W.-L. Chang, 2006: Trends in western North Pacific tropical cyclone intensity. *Eos, Trans. Amer. Geophys. Union*, **87**, 537–548, https://doi.org/10.1029/2006EO480001.

Yim, S. Y., B. Wang, J. Liu, and Z. W. Wu, 2014: A comparison of regional monsoon variability using monsoon indices. *Climate Dyn.*, **43**, 1423–1437, https://doi.org/10.1007/s00382-013-1956-9.

Ying, M., E.-J. Cha, and H. J. Kwon, 2011: Comparison of three western North Pacific tropical best track datasets in a seasonal context. *J. Meteor. Soc. Japan*, **89**, 211–224, https://doi.org/10.2151/jmsj.2011-303.

Yu, H., Y. Lu, P.-Y. Chen, and W. C. Zhou, 2012: Intensity change characteristics of tropical cyclones in the western North Pacific as revealed by three different datasets. *J. Trop. Meteor.*, **18**, 119–126.

Yuan, J., and J. Cao, 2012: North Indian Ocean tropical cyclone activities influenced by the Indian Ocean Dipole mode. *Sci. China Earth Sci.*, **56**, 855–865, https://doi.org/10.1007/s11430-012-4559-0.

Zhang, C., 2005: Madden–Julian oscillation. *Rev. Geophys.*, **43**, RG2003, https://doi.org/10.1029/2004RG000158.

——, 2013: Madden–Julian oscillation: Bridging weather and climate. *Bull. Amer. Meteor. Soc.*, **94**, 1849–1870, https://doi.org/10.1175/BAMS-D-12-00026.1.

——, and J. Gottschalck, 2002: SST anomalies of ENSO and the Madden–Julian oscillation in the equatorial Pacific. *J. Climate*, **15**, 2429–2445, https://doi.org/10.1175/1520-0442(2002)015<2429:SAOEAT>2.0.CO;2.

Zheng, Z.-W., I.-I. Lin, B. Wang, H.-C. Huang, and C.-H. Chen, 2015: A long neglected damper in the El Nino–Typhoon relationship: A 'Gaia-like' process. *Sci. Rep.*, **5**, 11103, https://doi.org/10.1038/srep11103.

Unauthenticated | Downloaded 12/18/20 02:55 PM UTC